ZEPHYR AEROSPACE PRODUCTS	**Configuration Selection**	**DESIGN NOTE** **002**
Aircraft Model:	STOLER-1	
Group Name:	Zephyr Aerospace Products	**Date:** 12/04/2025

Abstract:

This design note outlines the preliminary design, performance, and certification analysis of the STOLER-1, a 9-passenger, twin-engine, piston-propeller commuter aircraft optimized for short-takeoff-and-landing operations on constrained regional routes. Sized to a 9,500 lb MTOW with a useful payload of 2,250 lb, the high-wing, fixed-gear configuration with twin Lycoming IO-720 engines and 80.5 in four-blade constant-speed propellers achieves a design cruise speed of approximately 215 KTAS at 12,000 ft and a still-air range of about 553 nmi at maximum payload. The aircraft meets key field-performance requirements with takeoff and landing distances of roughly 1,377 ft and 1,450 ft over a 50 ft obstacle, while maintaining positive one-engine-inoperative climb margins and an operational service ceiling of 15,000 ft. The cabin and systems architecture support pressurized commuter, cargo, and medevac missions, with palletized cargo capability, FIKI operation via pneumatic de-ice boots, and a Garmin G1000 NXi-based avionics suite, all within an estimated flyaway acquisition cost of $\approx$ \$3.2M and CASM of \$0.31. The design is benchmarked against Tecnam P2012 STOL and Cessna Caravan class aircraft and is evaluated for compliance with 14 CFR Part 23 through integrated sizing, aerodynamics, propulsion, stability and control, structures, systems, and cost analyses to demonstrate feasibility for continued development and eventual certification.

Doc Number	Description	Date	Author
ZAP_G-01	Program Files	10/15/2025	ZAP
ZAP_CAD-01	3-View Drawings	10/15/2025	ZAP
ZAP_F-01	Cost Analysis	10/15/2025	ZAP
ZAP_Aircraft Sizing	Sizing Analysis	09/08/2025	ZAP
ZAP_Constraint Diagram_Cape Air	Constraint Diagram	09/15/2025	ZAP

Revision	Description	Date	Author
IR	Initial release	12/04/2025	ZAP

Member Name	Title
Conry Cabantac	Project Lead
Isaiah Santiago	Chief Engineer
Tyler Kingston	Propulsion/Weight Lead
Jacob House	Structures/Validation Lead
Pedro Leme Garcia	Aero/Performance Lead
Joseph Borrelli	Geometry/CAD Lead
Chase Dryan	Stability/Control Lead

Contents

1 Introduction

This capstone design project presents the complete preliminary design for a new general aviation aircraft. Centered around a request for proposal (RFP) submitted by regional commuter airline Cape Air, the team's aircraft, the STOLER-1, aims to deliver improved performance in takeoff and landing capability, cruise speed, and overall operating cost. The project combines multidisciplinary engineering principles, including aerodynamics, stability and control, propulsion, structures, and 3D design. Conducted as a collaborative team effort, it emphasizes communication and coordination between all team members across the entire design process. All analyses, calculations, and design choices are consolidated into one comprehensive document and presentation, enabling the team to demonstrate proper engineering documentation standards and effectively communicate their work with peers and industry guests.

1.1 Preliminary Aircraft Design

The purpose of this report is to show the performance results and the final layout of the selected configuration for STOLER-1. In this report, the team goes into detail how the aircraft performs and is modeled. The team intends to show that STOLER-1 can be used in the regional commuter market as it has STOL performance as well as a low acquisition cost. Most regional commuters will fly around 350 nmi, which STOLER-1 surpasses. The design includes fowler flaps so it can operate at small airports, Garmin G1000 NXi Flight deck, and two passenger entries. The design is special as it flies at 215 kt and the team took in mind the other missions the aircraft can be used: medical transport, evacuations, and one of the passenger entries are wide enough to be used as a cargo bay to put in a pallet. The aircraft passes all requirements: it holds nine passengers, cruises at a higher speed, under $6 million acquisition cost, and has a cruise range of 442 nmi and will reach many destinations the airlines need it to.

1.2 Team Organization and Strategies

To effectively manage the STOLER-1 project, the team created a structured leadership hierarchy made up of seven distinct roles: Chief Engineer, Project Lead, Aerodynamics Lead, Stability and Controls Lead, Propulsion Lead, Structures Lead, and CAD Lead. While each member held a primary responsibility for their specific area of expertise, the team worked collaboratively with other members whenever assistance was needed. The team worked in pairs, ensuring work was double-checked before submission. The 'buddy' system gave members the chance to assist with deliverables outside their expertise. Task management was controlled using a Gantt Chart, where it provided a timeline for deliverables and ensured the team stick to the deadlines during the bi-weekly meetings. The design of STOLER-1 required the team to adapt to advanced design tools and methodologies quickly. The team used OpenVsp and X-Foil to verify hand calculations digitally, validating STOLER-1's performance. The integration of CATIA V.5 allowed the team to design the structural components, interior layout, and control surfaces. Lastly, the team used design textbooks from respected aerospace engineers to verify results and make sure that the analysis aligned with aerospace fundamentals.

2 Concept of Operations

2.1 Requirements

The STOLER-1 concept is driven by the need for a FAA 14 CFR Part 23 certifiable, nine–passenger short–takeoff–and–landing (STOL) aircraft optimized for thin regional routes and utility operations. The baseline requirements focus on regulatory compliance, mission capability, field performance from short and constrained runways, and competitive acquisition and operating economics. The aircraft is intended to operate with a crew of two pilots, no lavatory, and the ability to accept standard cargo pallets for rapid reconfiguration between passenger and freight missions. Key quantitative and qualitative requirements are summarized below and captured in the compliance checklist in Table 2-1.

- **Certification:** Design must be certifiable under 14 CFR Part 23 (normal category) including STOL and Flight-Into-Known-Icing (FIKI) capabilities.
- **Crew and passengers:** Seating for 9 passengers plus 2 pilots (9 + 2 configuration).
- **Acquisition cost:** Flyaway acquisition cost less than $6,000,000 (FY$), excluding operator-specific options.
- **Operating economics (CASM):** Target operating cost per available seat-mile (CASM) less than $0.35 (FY$).
- **Cruise performance:** Normal cruise speed greater than 200 KTAS at the design cruise altitude.
- **Field performance:** Takeoff distance over a 50 ft obstacle less than 2,100 ft; landing distance over a 50 ft obstacle less than 2,100 ft.
- **Payload:** Minimum useful payload of 2,250 lb for passengers and baggage or equivalent cargo.
- **Range:** Mission range greater than 500 nmi with reserves at design payload.
- **Service ceiling:** Operational service ceiling of at least 15,000 ft MSL.
- **Propulsion:** Piston–propeller propulsion system compatible with FIKI operation and STOL performance.
- **Cabin configuration:** No lavatory installation; cabin and door geometry must allow palletized cargo loading and mixed passenger–cargo configurations.

Table 2-1: Preliminary requirements compliance checklist for the STOLER-1.

Requirement	Target / Limit	STOLER-1 Baseline
Certification basis	14 CFR Part 23	Part 23 (normal), STOL, FIKI (planned)
Seating	9 + 2 pilots	9 + 2 pilots
Acquisition cost	$< $6.0 M	$\approx$ $3.22 M
CASM	Low; $< $0.35	$< $0.35 (estimated)
Cruise speed	$>$ 200 KTAS	$\approx$ 215 KTAS
Takeoff distance (50 ft)	$<$ 2,100 ft	$\approx$ 1,377 ft
Landing distance (50 ft)	$<$ 2,100 ft	$\approx$ 1,450 ft
Payload	$\geq$ 2,250 lb	2,250 lb
Range	$>$ 500 nmi	$\approx$ 553 nmi
Service ceiling	$\geq$ 15,000 ft MSL	15,000 ft (design goal)
Propulsion type	Piston propeller	Twin piston propeller
FIKI capability	Required	Provided via de-ice/anti-ice systems
Lavatory	Not installed	None
Cargo pallet accessibility	Required	Aft door and cabin sized for pallets

2.2 Operations

The STOLER-1 is conceived as a commuter and utility aircraft for thin-route regional markets, with Cape Air as a reference operator and the broader 9–passenger market as characterized in [25]. The primary mission is a 9-passenger + 2-pilot Part 135 scheduled commuter configuration, carrying a practical payload of 2,250 lb (190 lb per passenger plus baggage) on stage lengths of 400–500 nmi in all-weather conditions, including Essential Air Service (EAS) routes, air-taxi and charter operations, and mixed passenger/cargo services in North America, Latin America, and selected Asia-Pacific and European markets where short runways and limited ground infrastructure are common [25].

Operationally, the aircraft is optimized for short-field performance and frequent cycling. Takeoff and landing distances on the order of 1,400–1,500 ft allow the STOLER-1 to access runways where existing types such as the Cessna 402 and Tecnam P2012 are constrained or performance-limited. Cruise speeds above 200 KTAS at 6,000 ft enable competitive block times relative to Caravan-class benchmarks while preserving low direct operating cost (DOC) and CASM, identified as dominant economic drivers in the 9-passenger segment [25].

The cabin layout supports rapid reconfiguration between full passenger and palletized cargo modes using a dedicated cargo door and rectangular cabin cross-section. This enables secondary missions such as small-package freight, medevac (stretcher plus attendant), and government/special-mission roles without major modification. Operations are assumed to be pressurized at low to mid altitudes (up to 15,000 ft), with FIKI capability provided by wing and tail de-ice boots, satisfying winter-operations requirements while avoiding the weight and complexity of liquid-based systems noted as pain points on legacy aircraft [25].

In day-to-day service, the STOLER-1 is sized to fit existing gate and ramp footprints, with wingspan and overall length kept within the Tecnam/Caravan envelope to avoid conflicts at constrained gates (e.g., Boston gate C27).

2.3 Fielding and Maintenance

Fielding of the STOLER-1 is envisioned in two phases. The first replaces aging Cessna 402s on like-for-like routes, leveraging similar runway requirements and non-pressurized operating altitudes to minimize changes in procedures, training, and infrastructure. The second targets expansion into new short-field and mixed passenger/cargo markets identified in the operator-segment analysis (air taxi/charter, thin-route commuter/EAS, and cargo/hybrid freight), allowing operators to standardize on a single, flexible 9-seat platform [25].

The maintenance philosophy emphasizes simplicity, low cost, and mature, supportable systems. The airframe is a high-wing, fixed-gear configuration with conventional aluminum primary structure and single-element Fowler flaps, chosen to reduce parts count and ease inspection and repair. Propulsion is provided by Lycoming IO-720-A1B piston engines with turbochargers, aligning with operator preferences for proven reciprocating engines over experimental or hybrid systems. A simple glass avionics suite and rubber de-ice boots are selected to keep maintenance man-hours and spares inventory low relative to turbine or highly integrated alternatives [25].

From a supportability standpoint, the design facilitates line maintenance at small outstations: major access panels, removable cowlings, and simplified landing-gear geometry are intended to allow most scheduled inspections and unscheduled repairs without specialized ground support equipment. The absence of a lavatory removes one of the most maintenance-intensive subsystems in regional aircraft, directly reducing DOC and turnaround disruptions [25].

Introduction into service is planned to leverage existing training pipelines. Pilot training uses conventional twin-piston handling qualities and glass-cockpit procedures similar to current fleet upgrades, while maintenance training focuses on incremental differences from legacy Lycoming- and Cessna-based systems.

3 Sizing Analysis

3.1 Initial Sizing

Using the aircraft database, the team used 9500 lb for the estimated gross weight of the aircraft. The aircraft's initial sizing was done using Roskam's fuel-fraction method. Roskam had equations to solve for the fuel-fractions at different phases as seen in Table 4.1. The team had to use input values that were reasonable for certain phases such as: specific fuel consumption (c_p), propeller efficiency (η_p), and lift-to-drag ratio (L/D). Roskam states that the calculated empty weight and the historical empty weight had to be within 0.5% of each other.

Assumptions and methods for Sizing Analysis.

- **Assumptions:** *Initial sizing analysis depended on many key performance estimates from historical data and standard operating conditions. From review of the aircraft database, the initial takeoff gross weight of 9500 lb was estimated to act as the starting point for sizing. To determine the fuel-fractions, critical efficiency parameters were assumed with reasonable values. These assumptions included c_p, η_p, and L/D. The values were chosen to represent expected aerodynamic and propulsion performance during specific phases of flight (e.g., climb, cruise, and loiter).*
- **Methods:** *The team determined initial aircraft sizing using the fuel-fraction method founded by Roskam. The mission profile was divided into specific segments of flight, and specific equations were applied to calculate the fuel-weight fractions of each flight as detailed in Table 4-1. The calculated fuel-fractions determined the empty weight of STOLER-1. The calculated empty weight was compared to historical empty weight trend from Roskam's book. Values were changed within specific limits defined by Roskam until the tolerance between the calculated empty weight and historical empty weight was within 0.5%, as recommended by Roskam's guidelines.*

Table 3-1: Fuel fractions per phase and corresponding weight.

Phase	Ratio	Weight (lb)
Engine Start	0.990	9405.000
Taxi	0.995	9357.975
Take-off	0.995	9311.185
Climb	0.990	9216.804
Cruise	0.957	8817.494
Loiter	0.986	8691.884
Descent	0.985	8561.505
Landing	0.990	8475.890

Table 3-2: Weight comparison with reference aircraft.

STOLER-1	Tecnam P2012 STOL	Cessna Caravan
9500 lb	8113 lb	8000 lb

Table 3-3: Aircraft weight breakdown.

Empty (lb)	Payload (lb)	Fuel (lb)	Crew (lb)	Trapped oil and fuel (lb)
5422.363	2250.000	1280.137	500.000	47.5

3.2 Constraint Analysis

The power versus wing–loading constraint diagram in Fig. 3-1 combines the takeoff distance, cruise, rate-of-climb, service-ceiling, constant–velocity turn, and stall-speed limits following the methodology of Gudmundsson [4]. The feasible region defined by these curves led to a selected design point of $W/S = 25.1$ lb/ft^2 and the corresponding power level, which satisfies all constraints while keeping sea-level power requirement relatively low. The stall lines indicate that, at a 60 kt stall speed, this wing loading implies $C_{L_{\max}} \approx 2.06$ in the high-lift configuration, which was judged acceptable for the STOL mission. For comparison, the Tecnam P2012 STOL, plotted on the same diagram, has a lower wing loading of 21.3 lb/ft^2 [13], favoring more aggressive STOL performance. STOLER-1's higher wing loading is therefore a deliberate compromise: it still meets the STOL takeoff and climb constraints, but provides improved cruise efficiency and a smoother ride quality relative to the Tecnam benchmark.

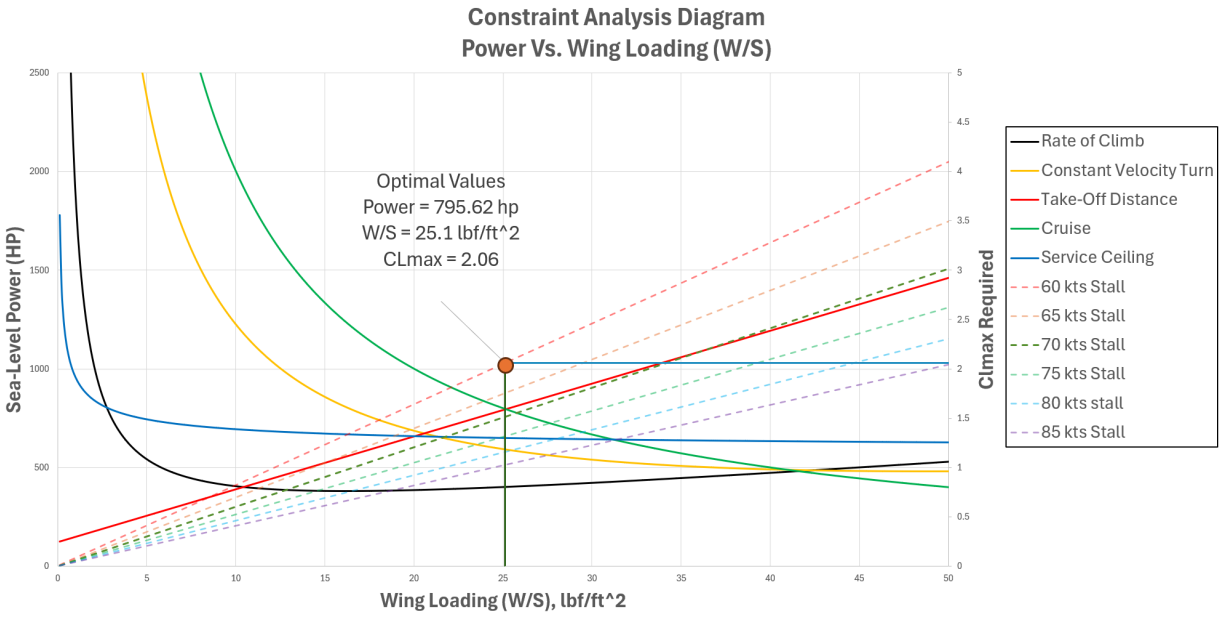

Figure 3-1: Constraint Diagram

Assumptions and methods for Constraint analysis.

- **Assumptions:** *The constraint diagram is constructed at the design takeoff weight using the standard power versus wing–loading framework described by Gudmundsson [4]. A sea-level, ISA atmosphere with a temperature offset of $\Delta T = -10$ R from standard is assumed for takeoff, climb, and low-altitude turn constraints to reflect a slightly colder, higher-density operating condition. Propeller efficiency is taken as constant at its representative cruise/climb value, and engine power is assumed to be fully available at sea level. The maximum rate-of-climb requirement is set to 1200 ft/min, chosen to match the benchmark climb capability of the Tecnam P2012 Traveller STOL variant [13]. Service ceiling is defined at a minimum climb rate of 100 ft/min. Stall-speed limits are represented by the dashed lines for V_S between 60 and 85 kt; for the chosen design point at $V_S = 60$ kt and $W/S = 25.1$ lb/ft^2, this corresponds to $C_{L_{\max}} \approx 4.1$ in the takeoff/landing configuration.*
- **Methods:** *The individual constraint curves are generated using the analytical relations in Gudmundsson [4], expressed in terms of power (P) as a function of wing loading (W/S). The takeoff constraint is obtained from the required field length and maximum lift coefficient, yielding a minimum (P) line as a function of (W/S) for the specified 50 ft obstacle height. The rate-of-climb constraint uses the excess power relation $P_{excess} = W\,(ROC)$ evaluated at the 1200 ft/min requirement to obtain another (P)–versus–(W/S) curve. The cruise constraint is derived from the power required at the design cruise*

speed and altitude, while the service-ceiling curve is computed at the altitude where ROC = 100 ft/min. The constant-velocity turn constraint is based on the sustained load-factor and drag increase in a coordinated level turn at the selected turn speed. The feasible design region is the envelope above all constraint curves and to the left of the stall-speed limits; the final design point of $W/S = 25.1$ lb/ft^2 and the corresponding sea-level power loading is chosen near the lower-power boundary of this feasible region to minimize required installed power while satisfying all performance constraints.

4 Performance Analysis

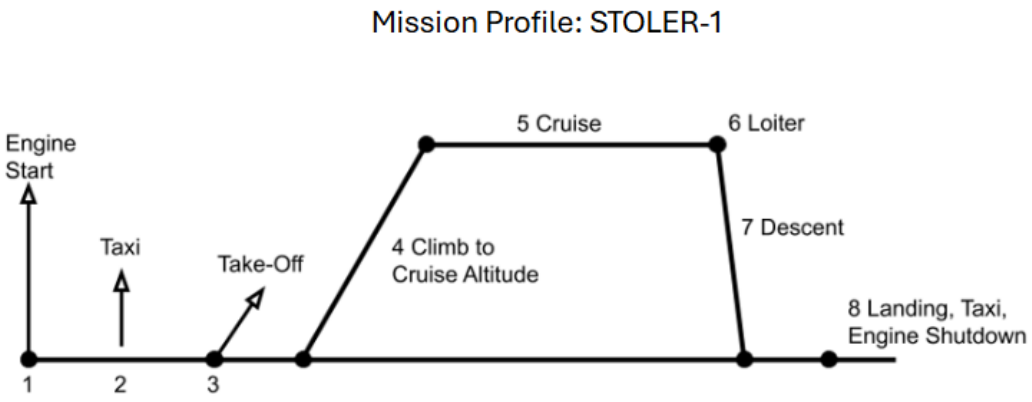

Figure 4-1: STOLER-1 mission profile illustrating each phase of the design mission.

The performance analysis of the STOLER-1 is conducted with direct reference to the mission profile shown in Fig. 4-1, which defines the sequence and duration of each flight segment. Using this mission as the baseline, the aircraft's capabilities are evaluated in takeoff, climb, cruise, descent, and landing to verify compliance with the Request for Proposal requirements. For each segment, key performance metrics such as required field length, climb gradient, cruise speed, and fuel consumption are quantified. To assess the competitiveness of the design, the resulting performance is benchmarked against comparable commuter STOL aircraft, specifically the Tecnam P2012 STOL and the Cessna Caravan.

Table 4-1: Performance Comparison Matrix.

Parameter	**STOLER-1**	**Tecnam P2012 STOL**	**Cessna Caravan**
MTOW (lb)	9,500	8,113	8,000
Cruise Speed (ktas)	215	185	186
Range (nm)	553	540	831
Takeoff Distance (ft)	1,377	1,394	2,055
Landing Distance (ft)	1,450	1,181	1,625
Payload (lb)	2,250	2,317	3,070

4.1 Take-Off Performance

One of the main selling points of the STOLER-1 is its STOL capability. To estimate the takeoff performance of the STOLER-1, the methodology outlined in Chapter 18 of *General Aviation Aircraft Design: Applied Methods and Procedures* [4] was followed. This method splits the takeoff estimation into distinct segments of the takeoff procedure, including ground run, rotation, transition, and climb distance over an obstacle. This analysis was carried out assuming maximum payload capacity, sea-level altitude, and a dry paved runway.

4.1.1 Takeoff Distance Breakdown

For analysis and reporting purposes, the takeoff is decomposed into four primary segments:

1. **Ground Run**: from brake release to initiation of rotation.
2. **Rotation**: from rotation initiation to lift off point.
3. **Transition**: from lift off point to achieving climb angle.
4. **Climb distance over obstacle**: from climb angle to clearance of 50 ft obstacle.

The total takeoff distance is the sum of these components measured from brake release to the clearance of a 50 ft obstacle. In this analysis the climb distance may be a negative value if the aircraft clears 50 ft before the transition phase is finished.

Table 4-2 summarizes the computed distances for each segment of the takeoff maneuver. The numerical values shown are based on the current performance analysis for the STOLER-1 and can be updated as higher-fidelity data become available.

Table 4-2: Takeoff distance breakdown for the STOLER-1 from brake release to clearance of a 50 ft obstacle.

Segment	**Description**	**Distance [ft]**
Ground Run	Brake release to rotation initiation	700
Rotation	rotation initiation to lift off point	117
Transition	liftoff point to climb angle	560
Climb distance over obstacle	climb angle to 50 ft clearance	-254
Total takeoff distance	Brake Release to 50 ft clearance	1,377

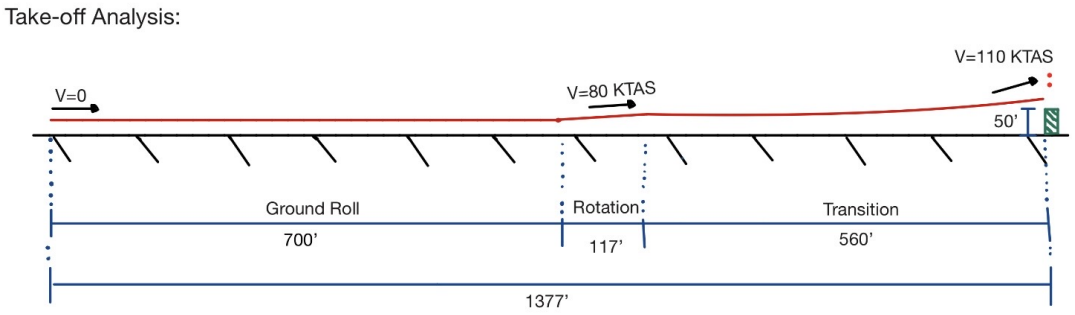

Figure 4-2: Schematic of the STOLER-1 takeoff profile showing ground roll, rotation, and initial climb segments.

4.1.2 Environment Sensitivities

To account for takeoff at different airports around the world, takeoff distance was found at varying altitude between sea level and 10,000 ft, as well as at temperatures at plus or minus 30 C. Figure 4-3 shows how the takeoff distance varies with these altitude effects.

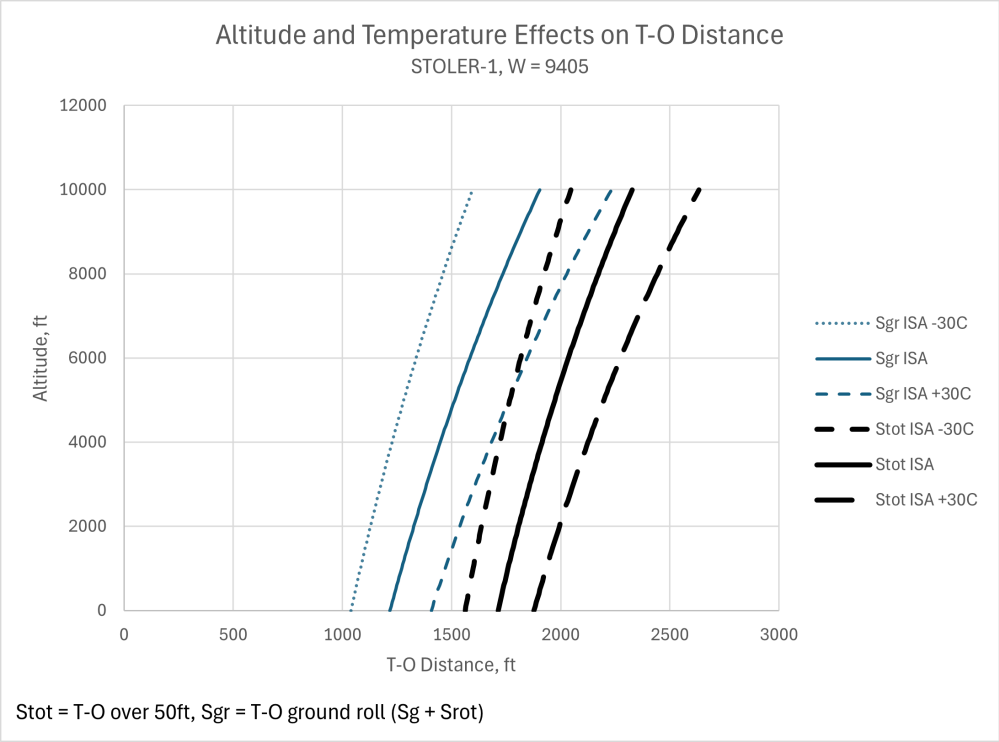

Figure 4-3: Takeoff Distance vs. Altitude

Assumptions and methods for takeoff performance.

- **Assumptions:** *The takeoff analysis assumes ISA standard–day conditions at sea level, a dry paved level runway with negligible slope, and no runway contamination. The STOLER-1 is taken at maximum takeoff weight with maximum payload and takeoff flap setting. Baseline results assume calm wind (zero headwind and crosswind) and nominal engine and propeller performance with no additional degradation beyond that captured in the propulsion model. Rotation and lift–off speeds are scheduled as fixed multiples of the stall speed in takeoff configuration, following the guidance of Gudmundsson [4]. For the environmental–sensitivity curves, altitude is varied from sea level to 10,000 ft, and temperature is varied by* $\pm 30^\circ C$ *about ISA, while runway surface, configuration, and technique remain unchanged.*
- **Methods:** *The takeoff distances in Table 4-2 are computed using the segmented takeoff–performance procedure described by Gudmundsson [4]. Stall speed in takeoff configuration is first obtained from wing loading, maximum lift coefficient, and density; this defines the scheduled rotation and lift–off speeds. The ground–run distance from brake release to rotation speed is found by integrating the longitudinal equation of motion along the runway with thrust, drag, and rolling resistance. The rotation distance is approximated from the average speed during rotation and the time required to achieve the takeoff pitch attitude. The transition segment is modeled as a curved flight path from lift–off to the steady climb attitude, and the subsequent climb distance to the 50 ft obstacle is obtained from the climb gradient; this term becomes negative if 50 ft is cleared before the end of the transition arc. Total takeoff distance is the sum of these segments from brake release to obstacle clearance. For the altitude and temperature sensitivity results in Figure 4-3, the same procedure is repeated with updated density, thrust lapse, and aerodynamic coefficients evaluated at the corresponding atmospheric conditions.*

4.2 OEI Take-Off Performance

A critical aspect of the STOLER-1's safety and operational capability is its performance during an engine-out scenario. To estimate the one-engine-inoperative (OEI) takeoff performance, the methodology in Chapter 18 of *General Aviation Aircraft Design: Applied Methods and Procedures* [4] was adapted for asymmetric thrust

conditions. The standard takeoff procedure is re-evaluated under OEI assumptions, incorporating reduced available thrust, increased yawing moment, reduced climb capability, and any additional control or speed requirements. This analysis assumes maximum takeoff weight, sea-level conditions, and a dry paved runway unless otherwise noted.

4.2.1 OEI Takeoff Distance Breakdown

For OEI analysis and reporting purposes, the takeoff is divided into the same four primary segments used in the all-engines-operating case. However, each segment reflects the degraded performance and modified procedures associated with an OEI event:

1. **Ground Run (OEI)**: From brake release to rotation initiation under reduced thrust and increased directional control requirements.
2. **Rotation (OEI)**: From rotation initiation to lift-off, accounting for higher rotation airspeed and increased stabilator/elevator authority requirements.
3. **Transition (OEI)**: From lift-off to achieving a stabilized OEI climb attitude.
4. **OEI Climb Distance Over Obstacle**: Distance required to climb from the established OEI climb attitude to clear a 50 ft obstacle.

The total OEI takeoff distance is the sum of all four components measured from brake release to 50 ft obstacle clearance, noting that the transition and climb segments may significantly increase relative to the all-engines-operating case.

Table 4-3: OEI takeoff distance breakdown for the STOLER-1 from brake release to clearance of a 50 ft obstacle.

Segment	**Description**	**Distance [ft]**
Ground Run (OEI)	Brake release to rotation initiation under OEI conditions	1,588
Rotation (OEI)	Rotation initiation to lift-off point	116
Transition (OEI)	Lift-off to establishment of OEI climb attitude	400
OEI Climb distance over obstacle	OEI climb to 50 ft clearance	100
Total OEI takeoff distance	Brake release to 50 ft clearance (OEI)	2,204

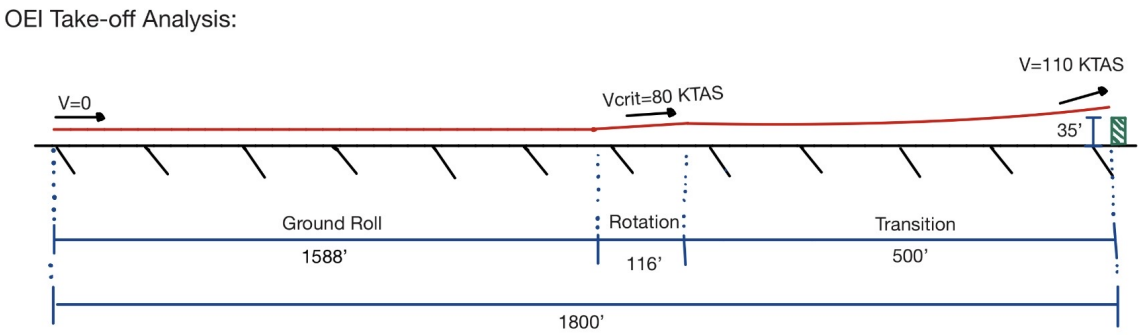

Figure 4-4: Schematic of the OEI takeoff profile for the STOLER-1 showing ground roll, rotation, and reduced-performance climb segments.

4.2.2 Environment Sensitivities (OEI)

OEI performance is more sensitive to environmental conditions than the all-engines-operating case. To evaluate these sensitivities, OEI takeoff distance should be computed across a range of altitudes from sea level to 10,000 ft, and at temperatures spanning ±30°C from standard conditions. Figure 4-5 provides a template for illustrating how OEI takeoff distance varies with altitude. Replace the figure once OEI performance data become available.

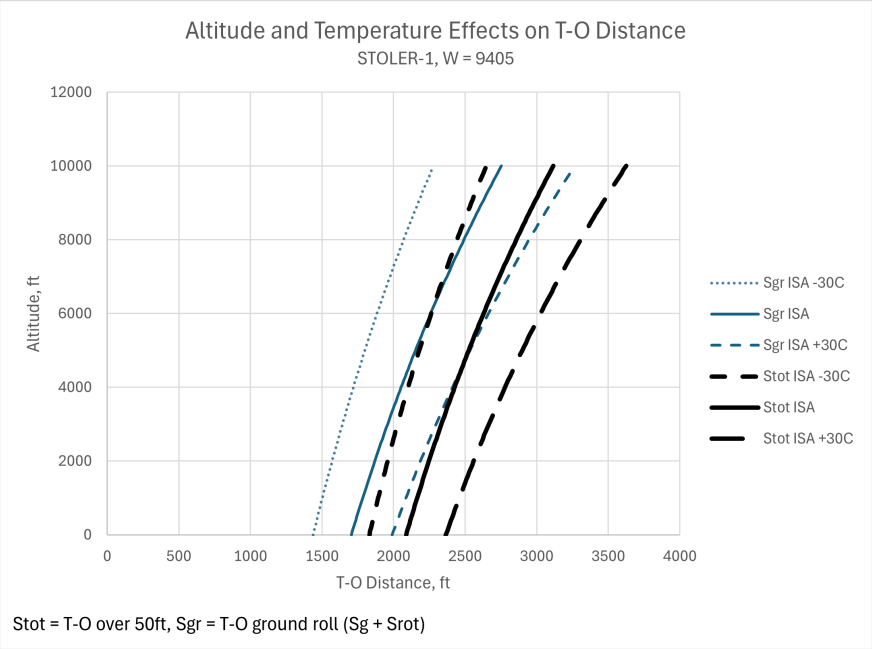

Figure 4-5: OEI Takeoff Distance vs. Altitude

Assumptions and methods for OEI takeoff performance.

- **Assumptions:** *The OEI takeoff analysis assumes ISA standard–day conditions at sea level for the baseline case, a dry paved level runway with negligible slope, and operation at maximum takeoff weight. An engine failure is assumed to occur at or just prior to rotation, with the failed engine fully feathered and the operating engine set to the prescribed takeoff/OEI power setting. Directional control is maintained using rudder and, if needed, a small bank angle into the operating engine, such that the aircraft remains within lateral–control and minimum–control–speed limits. Rotation, lift–off, and climb–out speeds in OEI conditions are scheduled as multiples of the appropriate stall speeds and minimum–control speed (e.g., V_{MC} and OEI climb speed) consistent with the guidance of Gudmundsson [4]. For the OEI environmental–sensitivity results, altitude is varied from sea level to 10,000 ft and temperature is varied by $\pm 30^{\circ}C$ about ISA, while runway surface, configuration, and OEI procedures remain unchanged.*

- **Methods:** *The OEI takeoff distances in Table 4-3 are computed by adapting the segmented takeoff–performance procedure of Gudmundsson [4] to asymmetric thrust conditions. Available thrust is reduced to reflect single–engine operation, including thrust lapse with altitude and propeller efficiency for the operating engine, while the failed engine contributes only drag (accounted for via an OEI drag increment). The ground–run (OEI) distance is obtained by integrating the longitudinal equation of motion from brake release to the OEI rotation speed, using the net accelerating force (single–engine thrust minus drag and rolling resistance) and enforcing directional–control limits through a minimum–control–speed constraint. The rotation (OEI) distance is estimated from the average speed and time required to pitch from the ground–run attitude to the OEI lift–off attitude under reduced control margins. The transition*

(OEI) segment is modeled as a curved flight path from lift–off to the stabilized OEI climb attitude at the scheduled OEI climb speed. Once established in steady OEI climb, the horizontal distance required to reach 50 ft is determined from the OEI climb gradient; this contribution may dominate the total OEI takeoff distance when climb performance is marginal. For the OEI altitude and temperature sensitivity curves in Figure 4-5, the same procedure is repeated with updated density, single–engine thrust lapse, propeller efficiency, and OEI aerodynamic characteristics evaluated at the corresponding atmospheric conditions.

4.3 Climb Performance

The climb capability of the STOLER-1 is a primary measure of mission efficiency and obstacle–clearance performance following takeoff. This section summarizes the baseline rate–of–climb characteristics as a function of calibrated airspeed (KCAS), first for varying pressure altitude and then for varying payload. In all cases, the propulsion system is assumed to be set at the scheduled climb power with the aircraft in climb configuration (takeoff/climb flaps).

4.3.1 Altitude Sensitivity

Figure 4-6 shows rate of climb versus KCAS at sea level and at 3,000, 6,000, and 9,000 ft. Each curve exhibits a well–defined peak corresponding to the best–rate-of-climb speed V_Y. Two main trends are evident as altitude increases:

1. The peak rate of climb decreases slightly, reflecting the modest reduction in available power with altitude. The maximum climb rate drops from roughly 2,600 ft/min at sea level to just above 2,400 ft/min by 9,000 ft.

2. The optimal climb speed shifts marginally to higher KCAS, consistent with the increase in true airspeed required at altitude for the same lift coefficient.

The curves remain relatively flat near their peaks, indicating that the STOLER-1 maintains strong climb performance throughout the typical mission altitude range.

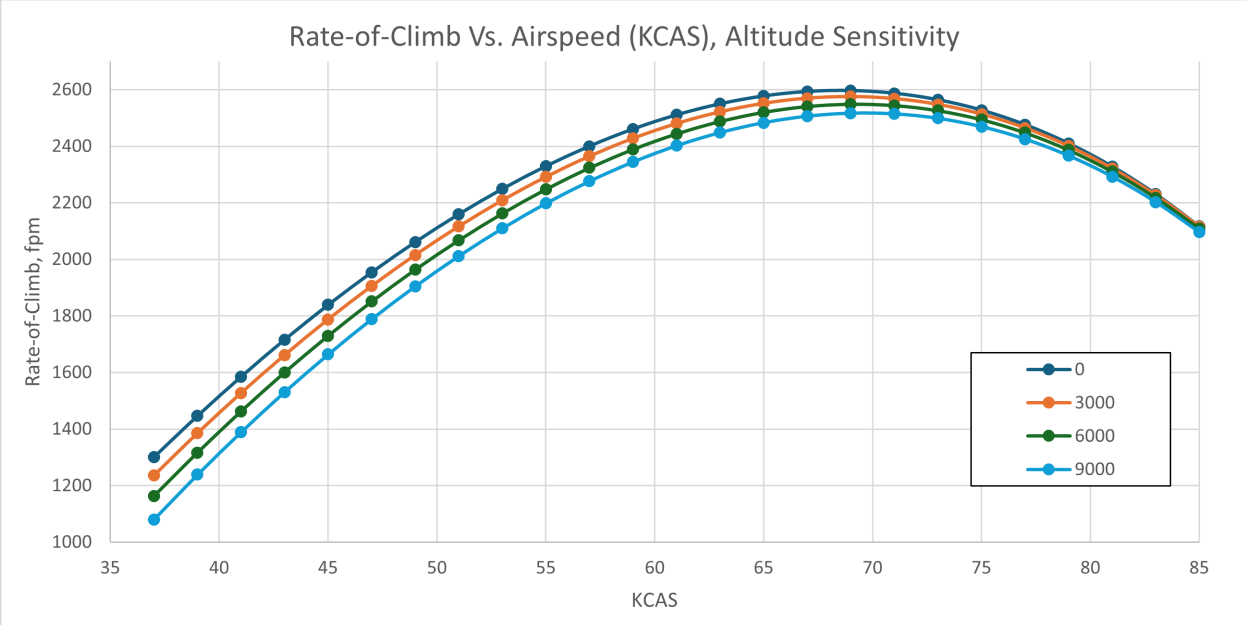

Figure 4-6: Rate of climb versus KCAS for several pressure altitudes.

4.3.2 Payload Sensitivity

The influence of payload on climb performance is presented in Figure 4-7. Curves are shown for maximum payload (9 passengers + baggage), and for 75%, 50%, and 25% of maximum payload, as well as the no–payload case. As payload (and thus gross weight) is reduced, rate of climb increases across the entire airspeed range:

- At maximum payload, the peak climb rate is on the order of 2,500–2,600 ft/min around 65–70 KCAS.
- With no payload, the peak climb rate rises to approximately 3,400–3,500 ft/min at nearly the same airspeed, providing substantial excess performance margin for ferry or repositioning flights.

The speed corresponding to V_Y remains clustered near the same KCAS for all payload levels, so a single scheduled best-rate-of-climb speed is sufficient to obtain near–optimal climb performance across the payload envelope.

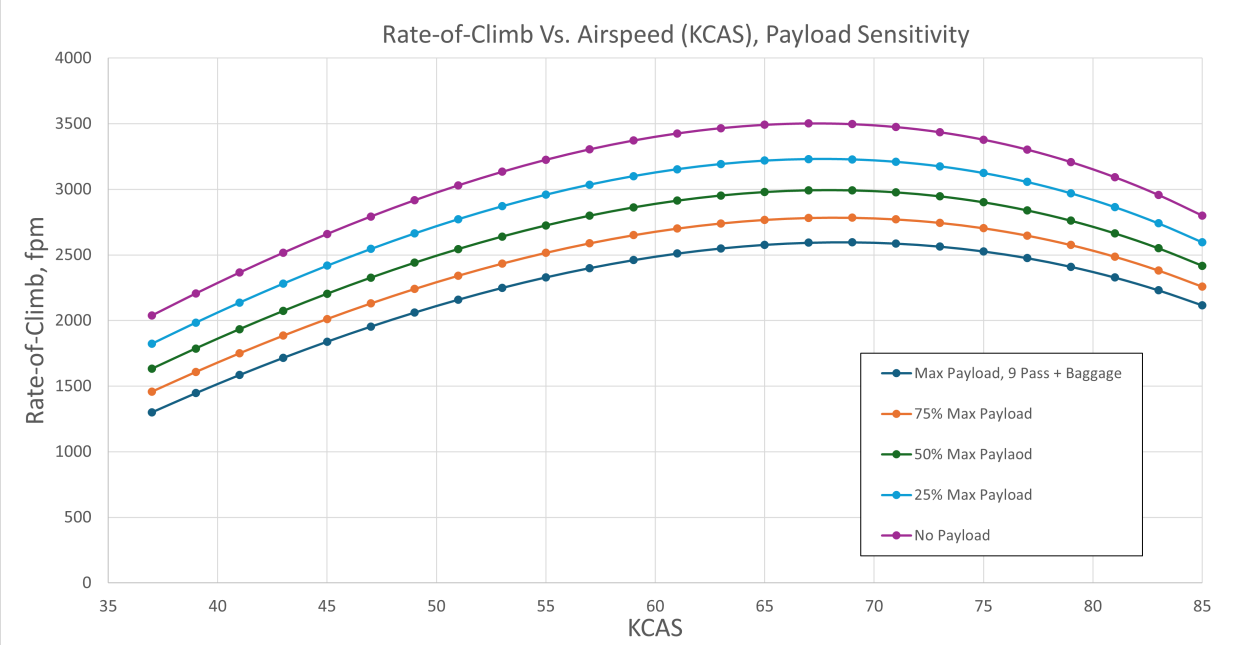

Figure 4-7: Rate of climb versus KCAS for different payload fractions.

Assumptions and methods for climb performance.

- **Assumptions:** *The climb analysis assumes ISA standard–day conditions, the propulsion system set to the scheduled climb power setting (constant–speed propellers at recommended climb RPM), and the aircraft in climb configuration (takeoff/climb flaps). Bank angle is limited to maintain coordinated flight and minimum drag. For the altitude–sensitivity curves, gross weight is held at the nominal climb weight with full payload. For the payload–sensitivity curves, altitude is fixed and weight is varied from maximum payload down to the no–payload condition. Power lapse with altitude, propeller efficiency, and aerodynamic characteristics (drag polar and lift curve) are taken from the performance models developed earlier in this report.*
- **Methods:** *The rate–of–climb curves are generated using the climb–performance procedure described by Gudmundsson [4]. For each combination of altitude, weight, and airspeed, the available power at the climb power setting is obtained from the power–altitude model and propeller efficiency. The required power for steady climb is computed from the drag polar and lift requirement, and the difference between available and required power is converted to rate of climb by dividing by the aircraft weight. This process is repeated over the KCAS range to produce the curves in Figures 4-6 and 4-7. The peak of each curve*

defines the best–rate-of-climb speed V_Y and the associated maximum climb rate for the specified altitude or payload.

4.4 One-Engine-Inoperative Climb Performance

The OEI takeoff and climb capability of the STOLER-1 is a key safety and certification driver, particularly for twin–engine aircraft operating from short or obstacle–limited runways. This section summarizes the OEI rate–of–climb characteristics as a function of calibrated airspeed (KCAS), first for varying pressure altitude and then for varying payload. In all cases, the remaining engine is assumed to be operating at takeoff power and the aircraft in the OEI climb configuration (gear up, flaps in takeoff/climb setting).

4.4.1 Altitude Sensitivity

Figure 4-8 shows OEI rate of climb versus KCAS at sea level and at 3,000, 6,000, and 9,000 ft. Each curve exhibits a well–defined peak, corresponding to the best–rate-of-climb speed $V_{Y,\mathrm{OEI}}$. As altitude increases, two trends are evident:

1. The peak rate of climb decreases, reflecting the reduced power available at lower air density.
2. The optimal climb speed shifts slightly to the right (higher KCAS), consistent with the higher true airspeeds required at altitude.

At sea level the STOLER-1 achieves an OEI peak climb rate of roughly 450–470 ft/min near 62–65 KCAS. By 9,000 ft the peak OEI climb rate is reduced by about 20–25%, but remains positive across the full airspeed range of interest, demonstrating adequate OEI climb capability at typical engine–out screen heights and second–segment climb conditions.

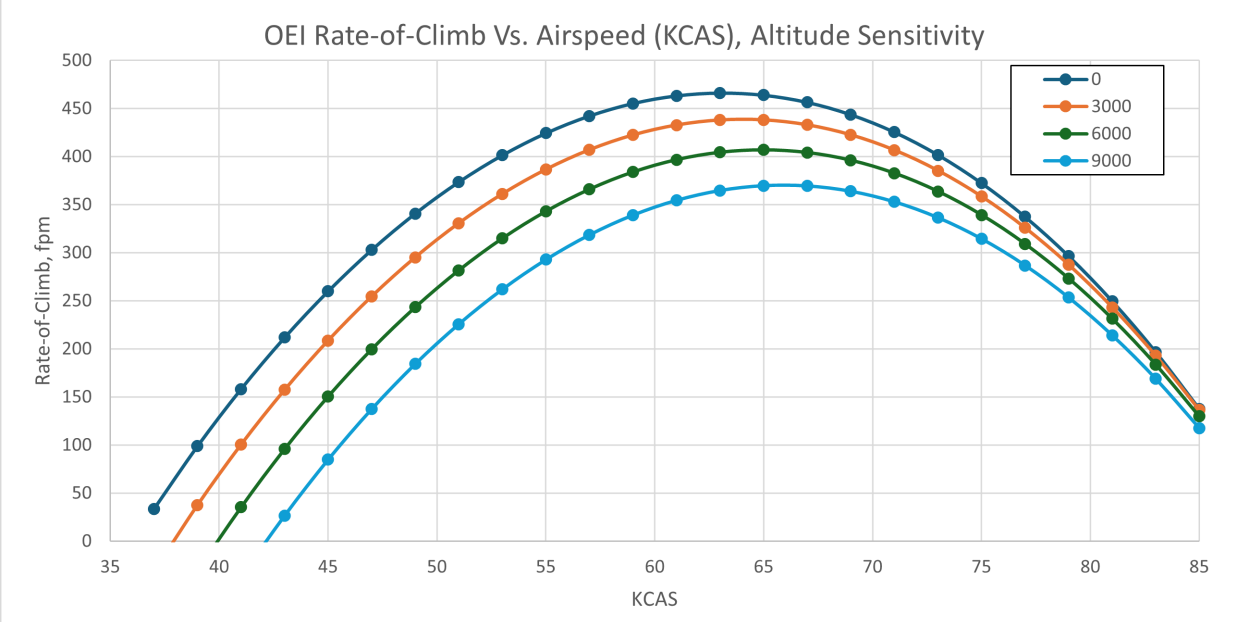

Figure 4-8: OEI rate of climb versus KCAS for several pressure altitudes.

4.4.2 Payload Sensitivity

The influence of payload on OEI climb performance is presented in Figure 4-9. Curves are shown for maximum payload (9 passengers + baggage), and for 75%, 50%, and 25% of maximum payload, as well as the no–payload case. As expected, reducing payload (and thus aircraft weight) increases OEI rate of climb across the entire airspeed range:

- At maximum payload, the peak OEI climb rate is on the order of 440–460 ft/min at 60–65 KCAS.
- With no payload, the peak OEI climb rate increases to approximately 700–720 ft/min, providing substantial climb margin for ferry or repositioning flights.

The speed for best OEI climb remains clustered near the same KCAS for all payload levels, so in practice a single scheduled $V_{Y,\mathrm{OEI}}$ provides near–optimal performance across the payload envelope.

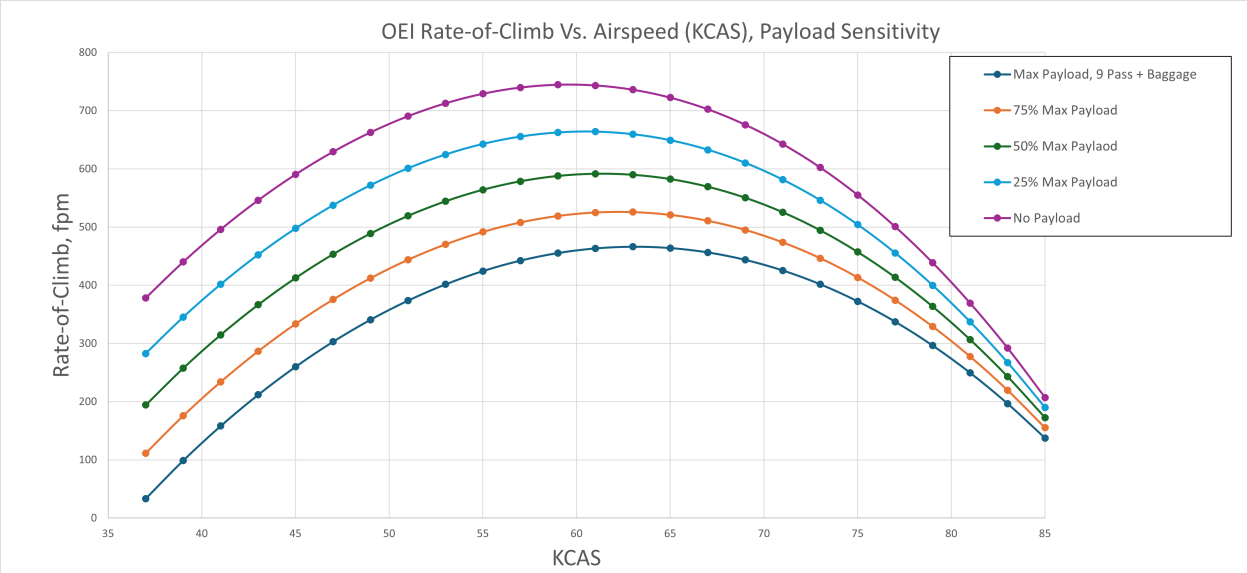

Figure 4-9: OEI rate of climb versus KCAS for different payload fractions.

Assumptions and methods for OEI climb performance.

- **Assumptions:** *The OEI climb analysis assumes ISA standard–day conditions, propellers set to maximum allowable continuous RPM on the operating engine, and the inoperative engine feathered. The aircraft is configured in OEI climb configuration (gear up, takeoff/climb flaps) with bank angle limited to maintain coordinated flight and minimum drag. For the altitude–sensitivity curves, gross weight is held constant at the OEI takeoff weight. For the payload–sensitivity curves, altitude is fixed and weight is varied from maximum payload down to the no–payload condition. Engine power lapse with altitude, propeller efficiency, and aerodynamic characteristics (drag polar and lift curve) are taken from the performance models developed earlier in this report.*
- **Methods:** *The OEI rate–of–climb curves are computed using the procedure described by Gudmundsson [4]. For a given altitude, weight, and airspeed, the available power with one engine inoperative, $P_{\mathrm{avail,OEI}}$, is obtained by first determining the total two–engine power available from the power–altitude model and propeller efficiency, then cutting this value in half and assuming the operating engine is delivering 95% of its rated power. The required power is computed from the drag polar and lift requirements for steady climb, and the excess power is converted to rate of climb by dividing by the aircraft weight. This process is repeated across the KCAS grid to generate each curve in Figures 4-8 and 4-9; the peak of each curve defines $V_{Y,\mathrm{OEI}}$ and the maximum OEI rate of climb for the specified altitude or payload.*

4.5 Cruise Performance

The STOLER-1's performance during the cruise phase is another selling point of the aircraft. Compared with similar aircraft, the STOLER-1 features a significant boost in cruise speed. The cruise performance estimations were carried out using methodology outlined in Gudmundsson's "General Aviation Aircraft

Design". This analysis was carried out considering a max payload, an aircraft weight representative of the aircraft during cruise, and at an altitude of 12,000 ft with no temperature deviation. From this cruise performance estimation the following values were produced in 4-4.

Table 4-4: Principal airspeeds during cruise phase

Term	Description	Airspeed (kts)
V_{min}	Minimum level airspeed	46
V_S	Stalling speed	73.4
V_{BG}	Best glide airspeed	129
$V_{TR_{min}}$	Minimum thrust required airspeed	254
$V_{PR_{min}}$	Minimum power required airspeed	98.2
$V_{R_{max}}$	Maximum range airspeed	
V_{CAR}	Carson's airspeed	171
$V_{TR_{min}}$	Minimum thrust required airspeed	-254
Total takeoff distance	Brake Release to 50 ft clearance	1,377

4.6 Landing Performance

The landing performance of the STOLER-1 is driven by its steep approach capability and high-lift configuration. As a STOL aircraft, the STOLER-1 is intended to operate with an approach flight path angle of approximately 7°, significantly steeper than the conventional 3° approach used by many transport and general aviation aircraft. This steeper approach allows the aircraft to clear standard obstacles and still achieve a short ground roll, reducing the overall landing distance required on constrained runways.

4.6.1 Landing Distance Breakdown

For analysis and reporting purposes, the landing is decomposed into three primary segments:

1. **Approach segment**: from threshold crossing height to flare/rotation initiation.
2. **Rotation (flare) segment**: from flare initiation to main gear touchdown.
3. **Braking segment**: from touchdown to full stop.

The total landing distance is the sum of these components measured from the runway threshold to the point at which the aircraft comes to rest.

Table 4-5 summarizes the computed distances for each segment of the landing. The numerical values shown are based on the current performance analysis for the STOLER-1 and can be updated as higher-fidelity data become available.

Table 4-5: Landing distance breakdown for the STOLER-1 from threshold to full stop.

Segment	Description	Distance [ft]
Approach	Threshold to flare initiation (7° approach)	407
Rotation	Flare / rotation to main gear touchdown	350
Braking	Ground roll with braking to full stop	693
Total landing distance	Threshold to full stop	1,450

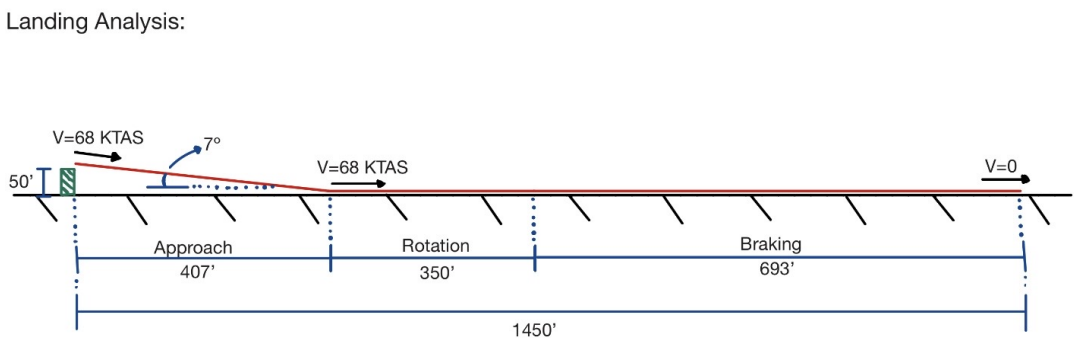

Figure 4-10: Schematic of the STOLER-1 landing profile showing approach, rotation (flare), and braking segments.

Assumptions and methods for landing distance calculations.

- **Assumptions:** *The STOLER-1 landing analysis assumes a nominal approach glide-slope of* 7° *in full landing configuration (*30° *flap deflection), consistent with STOL operations. The stall speed in landing configuration is taken as* $V_S = 60$ *kt, with the speed over the 50 ft obstacle set to* $V_{50} = 1.3\,V_{\mathrm{S,land}}$ *and the touchdown speed to* $V_{\mathrm{TD}} = 1.15\,V_{\mathrm{S,land}}$*, giving* $V_{\mathrm{TD}} \approx 116.5$ *ft/s. The runway is assumed to be dry, level, and paved. For the braking segment, a landing weight of 8,475 lb, gravitational acceleration* $g = 32.2$ *ft/s*^{2}*, braking friction coefficient* $\mu = 0.5$*, air density* $\rho = 0.00238$ *slug/ft*^{3}*, reference wing area* $S_{\mathrm{ref}} = 376.5$ *ft*^{2}*, ground-lift coefficient during braking at zero angle of attack* $C_{L_G} = 1.12$*, and drag coefficient* $C_D = 0.095$ *are used. Reverse thrust is neglected, and the assumed tire–runway friction limits braking.*
- **Methods:** *The landing-distance breakdown follows the procedure in Nicolai's Fundamentals of Aircraft and Airship Design [5]. The approach distance* S_A *is obtained from the 50 ft threshold height and the* 7° *approach angle using* $S_A = 50/\tan\gamma_{\mathrm{app}}$*, yielding* $S_A \approx 407$ *ft. The free-roll distance* S_{FR} *is computed assuming a 3 s delay between touchdown and full braking, with constant ground speed equal to* V_{TD}*, giving* $S_{FR} \approx 349$ *ft. The braking distance* S_B *is calculated from* V_{TD} *and the average deceleration obtained from the braking force balance in Nicolai's model, using the specified* μ*,* C_{L_G}*,* C_D*,* ρ*,* S_{ref}*, and landing weight; this yields* $S_B \approx 694$ *ft. The total landing distance is then* $L_{\mathrm{dist}} = S_A + S_{FR} + S_B \approx 1{,}450$ *ft. Intermediate speed schedules, forces, and decelerations are computed following Nicolai's landing-performance methodology and can be refined as more detailed aerodynamic and braking data become available.*

4.7 Range Performance

The range performance of the STOLER-1 is evaluated to verify that the aircraft can satisfy the design cruise distance and reserve requirements specified in the Request for Proposal. A piston–propeller form of the Breguet range relation is used, with performance referenced to the selected design cruise condition of $V = 215$ KTAS at 12,000 ft and the Lycoming IO-720-A1B engines operating in a turbonormalized configuration. Under these assumptions, the maximum still-air range of the STOLER-1 is computed and compared against the minimum required range of 500 nmi, demonstrating that the baseline design provides adequate fuel capacity and aerodynamic efficiency to meet the mission requirement with margin.

4.7.1 Range Model and Assumptions

For preliminary design, the mission range is estimated with the propeller-version of the Breguet range equation,

$$R = \frac{\eta_p}{c_p} V \frac{L}{D} \ln\left(\frac{W_i}{W_f}\right), \tag{1}$$

where:

- R is the still-air range [nmi],
- η_p is the propeller efficiency in cruise,
- c_p is an effective specific fuel-consumption parameter [hr^{-1}],
- V is the representative (selected) design cruise speed [kt],
- L/D is the lift-to-drag ratio in cruise,
- W_i and W_f are the initial and final weights over the powered portion of the mission, respectively.

The specific fuel-consumption term c_p is obtained from the Lycoming IO-720-A1B operator's manual [9] by extracting a representative cruise brake specific fuel consumption (BSFC) at the selected power setting and converting it into an effective parameter in [hr^{-1}] suitable for use in Eq. (1). In practice, the manual provides cruise fuel flow $\dot{W}_f$ [lb/hr] and engine power P_{cr} [hp]. A BSFC value is first computed as

$$\mathrm{BSFC} = \frac{\dot{W}_f}{P_{\mathrm{cr}}} \left[\frac{\mathrm{lb}}{\mathrm{hp}\cdot\mathrm{hr}}\right], \tag{2}$$

which is then combined with the aircraft's cruise power loading and an assumed propeller efficiency $\eta_p = 0.87$ to define an effective specific fuel-consumption parameter c_p that reproduces the IO-720 cruise fuel flow when used in Eq. (1). For the present analysis, applying Eq. (2) and this procedure yields $c_p = 0.56\ \mathrm{hr}^{-1}$.
Table 4-6 summarizes the parameters adopted for the STOLER-1 range calculation, updated to reflect the selected design cruise condition and the Lycoming IO-720-A1B engine data.

Table 4-6: Input parameters for STOLER-1 prop-Breguet range calculation (Lycoming IO-720-A1B, turbonormalized).

Quantity	Symbol	Value	Units	Notes
Propeller efficiency (cruise)	η_p	0.87	–	Assumed constant in cruise
Specific fuel-consumption parameter	c_p	0.56	hr^{-1}	From IO-720 BSFC data [9]
Representative cruise speed (design)	V	215	kt	Selected design cruise speed at 12,000 ft
Lift-to-drag ratio in cruise	L/D	19.6	–	From cruise aerodynamic analysis at 12,000 ft
Cruise fuel fraction	W_f/W_i	0.919	–	Includes climb, cruise, descent fuel
Weight ratio	W_i/W_f	1.09	–	$W_i/W_f = 1/(W_f/W_i)$
Log weight ratio	$\ln(W_i/W_f)$	0.0845	–	$\ln(1/0.919)$

4.7.2 Numerical Range Calculation

Using the parameters in Table 4-6, the propeller Breguet range equation, Eq. (1), evaluates to

$$\begin{aligned} R &= \frac{\eta_p}{c_p} V \frac{L}{D} \ln\left(\frac{W_i}{W_f}\right) \\ &= \frac{0.87}{0.56} \times 215\ \mathrm{kt} \times 19.6 \times 0.0845 \\ &\approx 553.20\ \mathrm{nmi}. \end{aligned}$$

Table 4-7 compares the computed maximum still-air range to the nominal RFP requirement (taken here as $R_{\text{req}} = 500$ nmi for the design mission).

Table 4-7: Summary of STOLER-1 range performance versus requirement.

Metric	**Value**	**Units**
Maximum still-air range, R	553.2	nmi
RFP minimum required range, R_{req}	500	nmi
Range margin ($R - R_{\text{req}}$)	53.2	nmi
Range margin (percent)	10.6	%

Based on these updated cruise conditions and engine data, the STOLER-1 achieves a calculated still-air range of approximately 553.2 nmi, providing a margin of about 53.2 nmi (10.6%) above the nominal 500 nmi requirement before accounting for regulatory reserves and potential headwinds.

Assumptions and methods for range calculations.

- **Assumptions:** *The range analysis assumes a representative mid-cruise altitude of 12,000 ft and a cruise condition consistent with the selected design point, $V = 215$ KTAS. The propulsion system consists of two Lycoming IO-720-A1B engines operating in a turbonormalized configuration. A representative cruise BSFC is taken from the IO-720 operator's manual [9] at the chosen manifold pressure, RPM, and percent power, and is used to define an effective $c_p = 0.56\ hr^{-1}$ in conjunction with an assumed propeller efficiency of $\eta_p = 0.87$. An average aerodynamic efficiency of $(L/D) = 19.6$ is used to represent the en route portion of the mission. The mission fuel fraction over the powered portion of flight is taken as $W_f/W_i = 0.919$, representing warm-up, taxi, climb, cruise, descent, and approach fuel. Winds, icing penalties, and off-design operation are neglected in this preliminary estimate.*
- **Methods:** *The range is computed using the propeller Breguet relation in Eq. (1). In practice, BSFC is obtained by reading cruise fuel flow $\dot{W}_f$ and power P_{cr} from the IO-720 manual [9] at the selected operating point and computing BSFC $= \dot{W}_f/P_{\text{cr}}$. This BSFC is then combined with the aircraft's cruise power loading and the assumed η_p to define the effective parameter c_p used in Eq. (1). Substitution of η_p, c_p, V, L/D, and $\ln(W_i/W_f)$ yields the still-air range R. As additional aerodynamic data, engine performance maps, and refined mission fuel-fraction breakdowns become available, the parameters in Table 4-6 and the resulting range values in Table 4-7 can be updated without altering the underlying methodology.*

4.7.3 Payload–Range Analysis

In addition to the baseline maximum-payload range calculation, a simple payload–range analysis was performed to illustrate how the STOLER-1's range capability increases as payload is reduced. Table 4-8 summarizes the key operating points considered, and Fig. 4-11 provides a notional payload–range diagram highlighting the trade between payload and range capability.

Table 4-8: STOLER-1 payload–range summary for representative operating points.

Operating point	**Description**	**Range [nmi]**
Maximum payload / MTOW	Full passenger + baggage payload	553
4-passenger payload	Reduced payload (4 passengers)	1,015
Zero payload	Ferry / repositioning (no payload)	1,624

These results show that, at maximum gross weight with full payload, the STOLER-1 achieves a still-air range of approximately 553 nmi, meeting the 500 nmi requirement with margin. When the payload is reduced to a 4-passenger configuration, the additional fuel available for cruise increases the range to roughly 1,015 nmi. In

the zero-payload (ferry) condition, the aircraft can achieve an extended range of about 1,624 nmi, providing ample flexibility for repositioning or maintenance ferry flights.

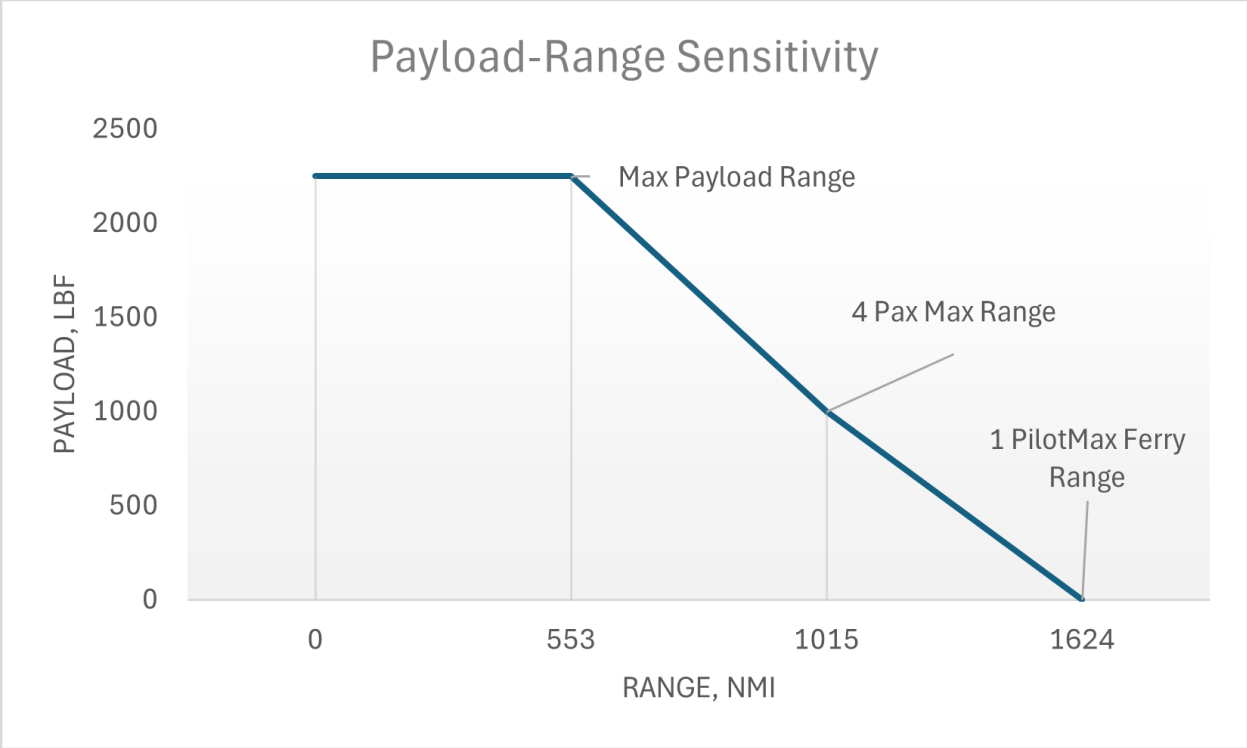

Figure 4-11: Payload–range diagram for STOLER-1 showing maximum-payload, 4-passenger, and zero-payload operating points.

Overall, the payload–range characteristics of STOLER-1 demonstrate that the aircraft not only satisfies the 500 nmi mission requirement at maximum payload, but also offers substantial additional range capability as payload is reduced. The ability to trade payload for range—extending from 553 nmi at MTOW to over 1,600 nmi in a ferry configuration—provides operators with significant operational flexibility for route planning, seasonal demand shifts, and repositioning flights, enhancing the overall utility and market competitiveness of the design.

5 Configuration

The configuration of STOLER-1 was developed through an iterative trade-study process that balanced STOL performance, commuter-aircraft operations practicality, and regulatory compliance. Multiple candidate layouts were evaluated, varying wing placement, number of engines and location, and empennage type to assess their effects on low-speed handling, OEI performance, structural efficiency, and maintainability. The final high-wing, twin-engine, conventional-tail configuration was selected for its superior field performance, large cabin and cargo accessibility, and strong alignment with proven commuter aircraft such as the TECNAM P2012 and Britten-Norman Islander. This section documents the evolution from initial concepts to the selected Outer-Mold-Line, including external and internal layout decisions driven by Cape Air's operational requirements and applicable certification constraints.

5.1 Design Morphology

Four configurations were initially considered:

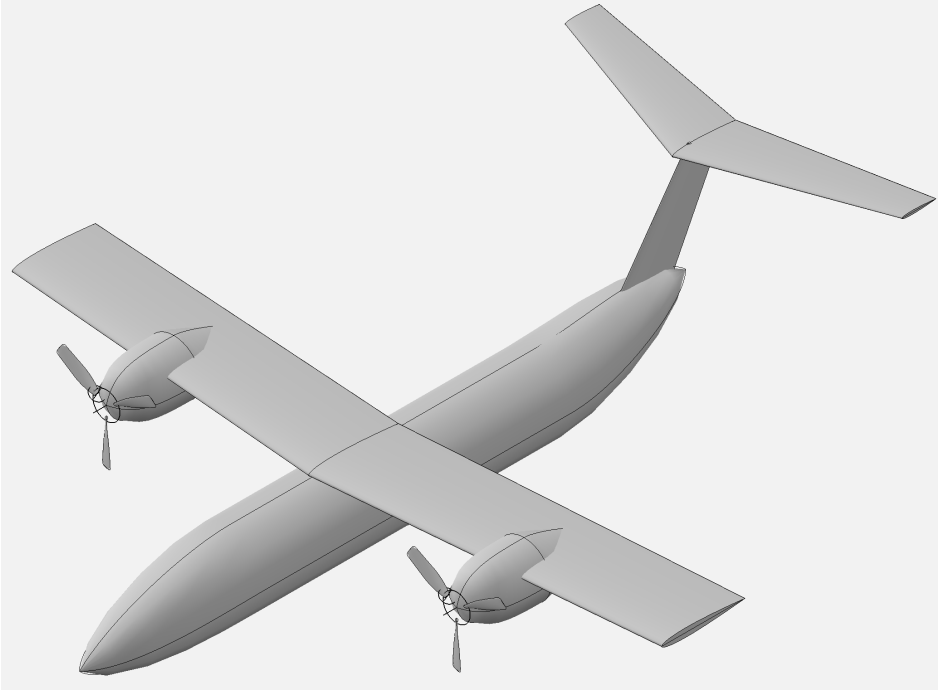

Figure 5-1: OpenVSP render of configuration A.

Configuration A design elements feature a high-wing, twin-engine, t-tail configuration.

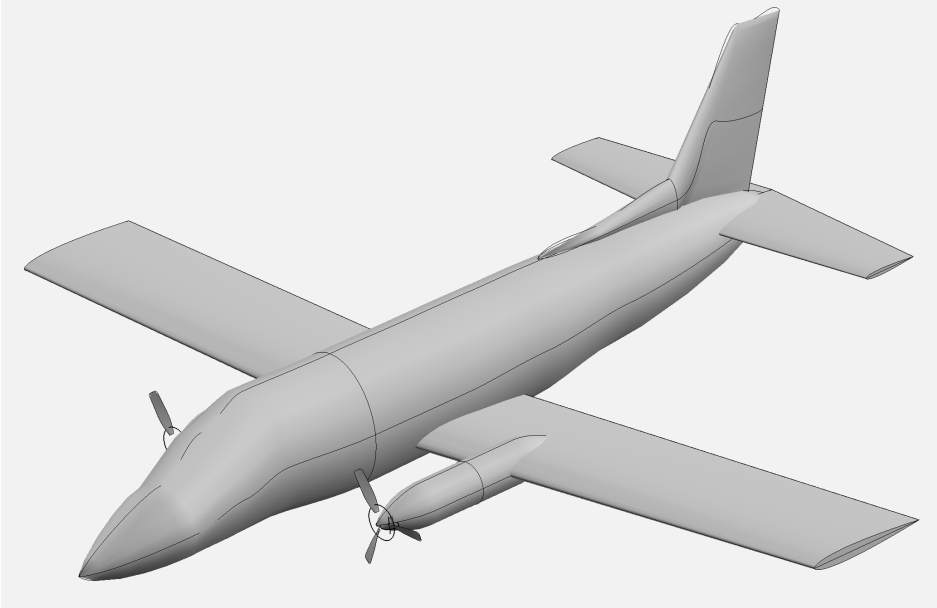

Figure 5-2: OpenVSP render of configuration B.

Configuration B design elements feature a low-wing, twin-engine, conventional-tail configuration.

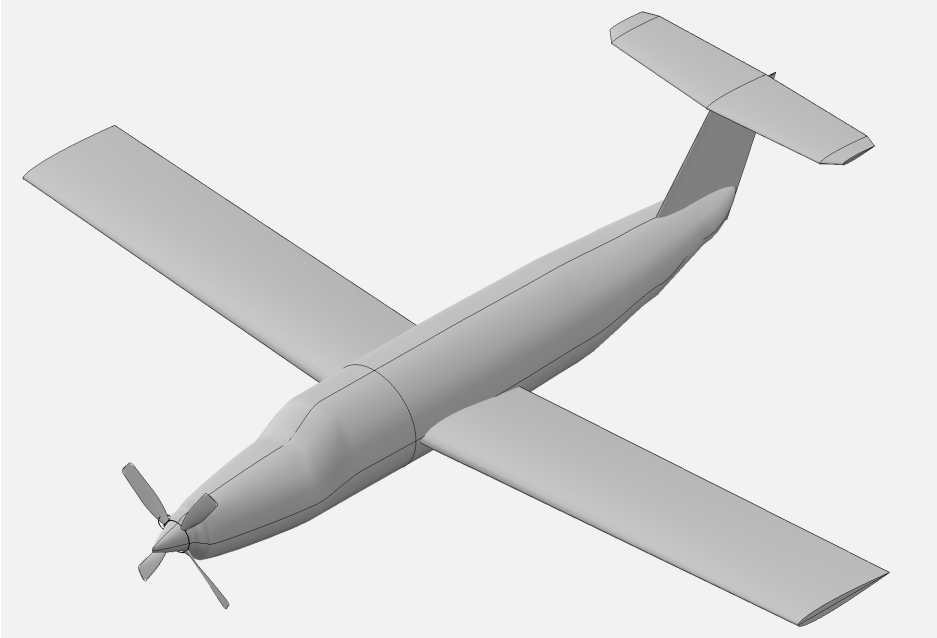

Figure 5-3: OpenVSP render of configuration C.

Configuration C design elements feature a low-wing, single-tractor engine, t-tail configuration.

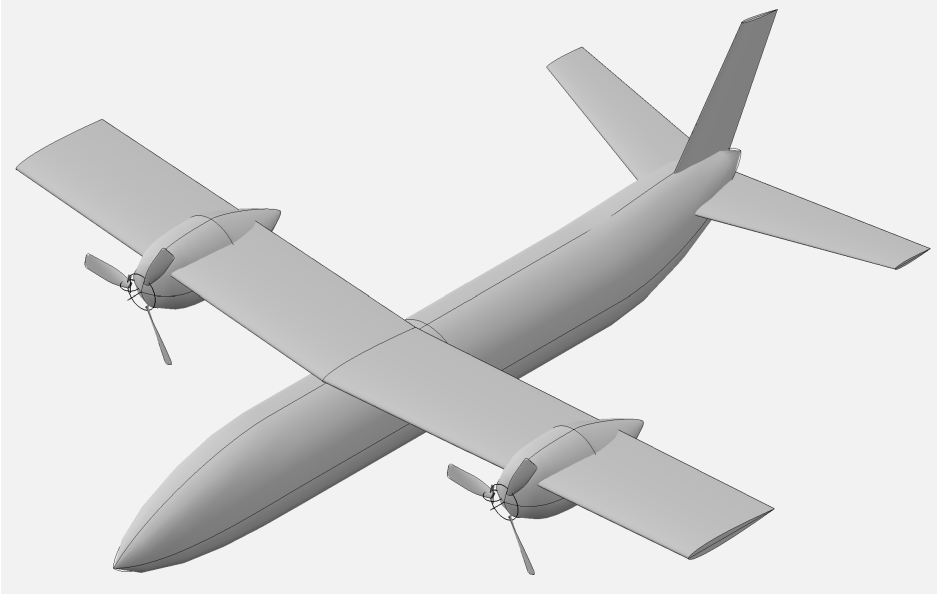

Figure 5-4: OpenVSP render of configuration D.

Configuration D design elements feature a high-wing, twin-engine, conventional-tail configuration.

In the end, Configuration D was selected and sized by referencing several existing aircraft serving similar roles, such as the TECNAM P2012 and the Britten-Norman Islander, both of which are high-wing, twin-engine, 8–9 passenger designs. The placement of the horizontal and vertical tail surfaces was based on these reference aircraft, with both surfaces positioned slightly further aft to accommodate the enlarged rear payload bay on the proposed configuration. Further analysis of One-Engine-Inoperative (OEI) and stability was a primary driver for the tail size.

Further drag analysis and development led to a more streamlined fuselage in addition to a larger vertical tail to account for OEI condition and stability requirements. This helped ensure the aircraft would not lose control were an engine to go out or a disturbance to occur.

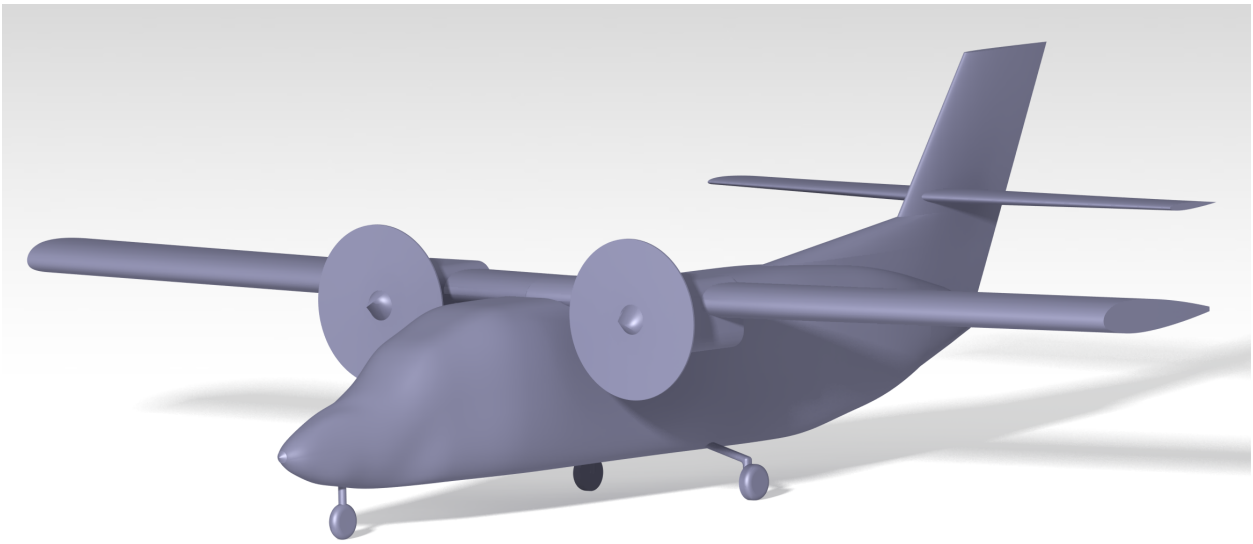

Figure 5-5: CATIA Side Render

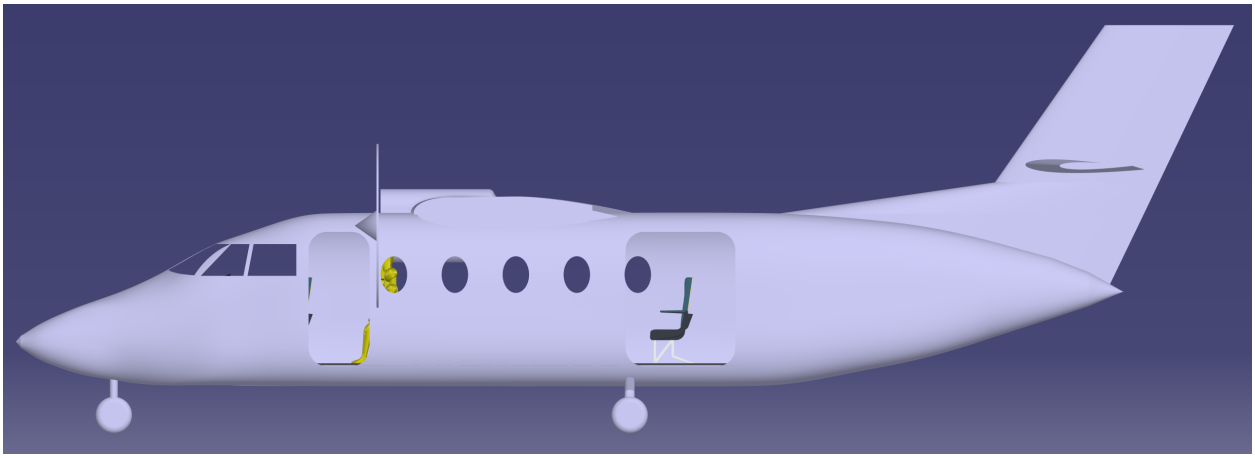

Figure 5-6: CATIA Side Render

Additional refinements include repositioning the engines closer to the fuselage, maintaining a six-inch clearance between the propeller tips and the fuselage sidewall.

5.2 External Layout

The placement of the engines was primarily dictated by the required distance between the propeller tips and the fuselage. According to 14 CFR §25.925, there must be at least one inch of radial clearance between the blade tips and the airplane structure [31]. STOLER-1 is designed with a 6-inch clearance. The number of occupants was defined by Cape Air's requirements, and fixed landing gear was selected to minimize both cost and weight.

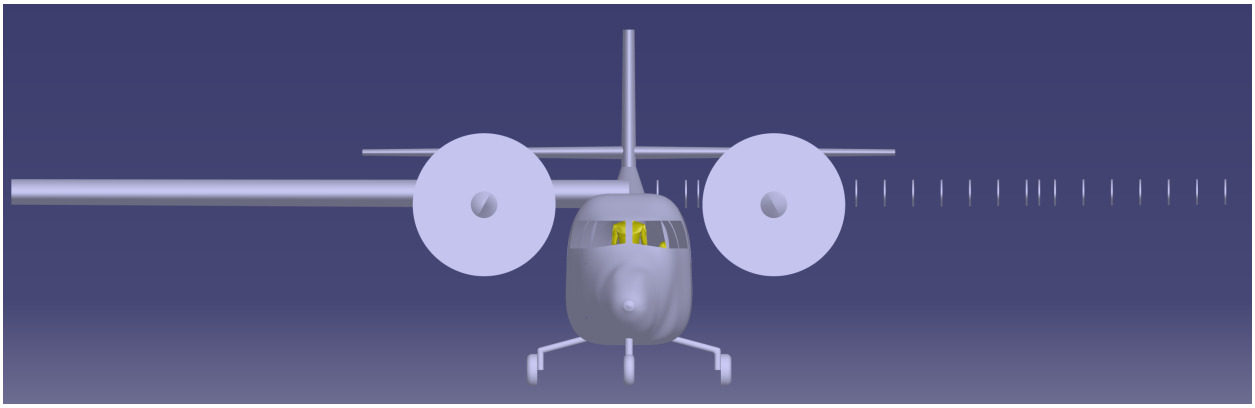

Figure 5-7: CATIA Front Render

Internal portions of the internal wing structure—such as the fuel tanks and several rib locations—were designed. These changes are a direct result of feedback received during the Midterm presentation and further checks for all regulatory compliance.

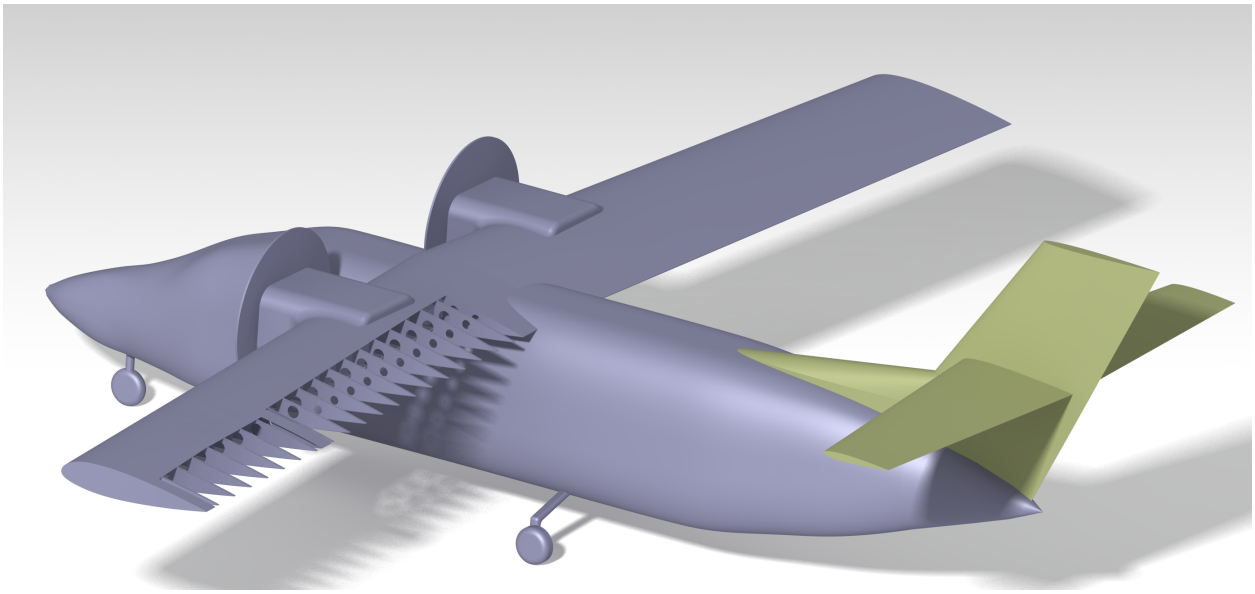

Figure 5-8: CATIA Solid Model for DR2

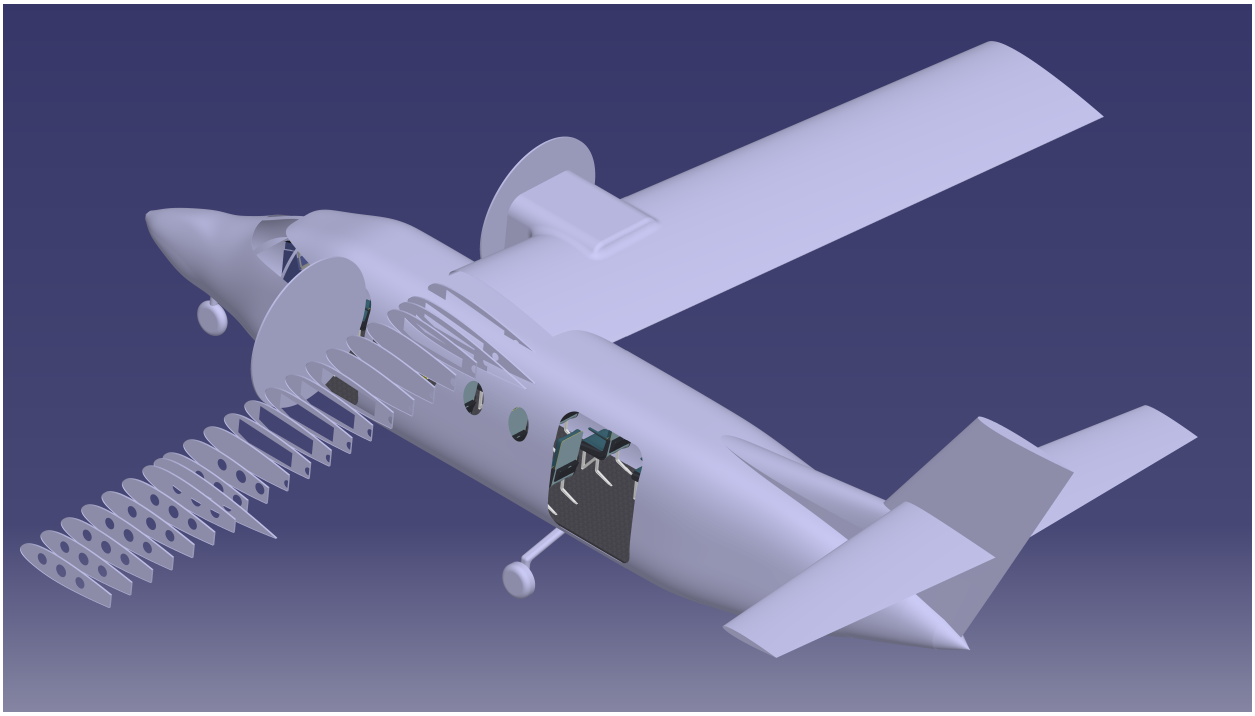

Figure 5-9: CATIA Rear ISO Render

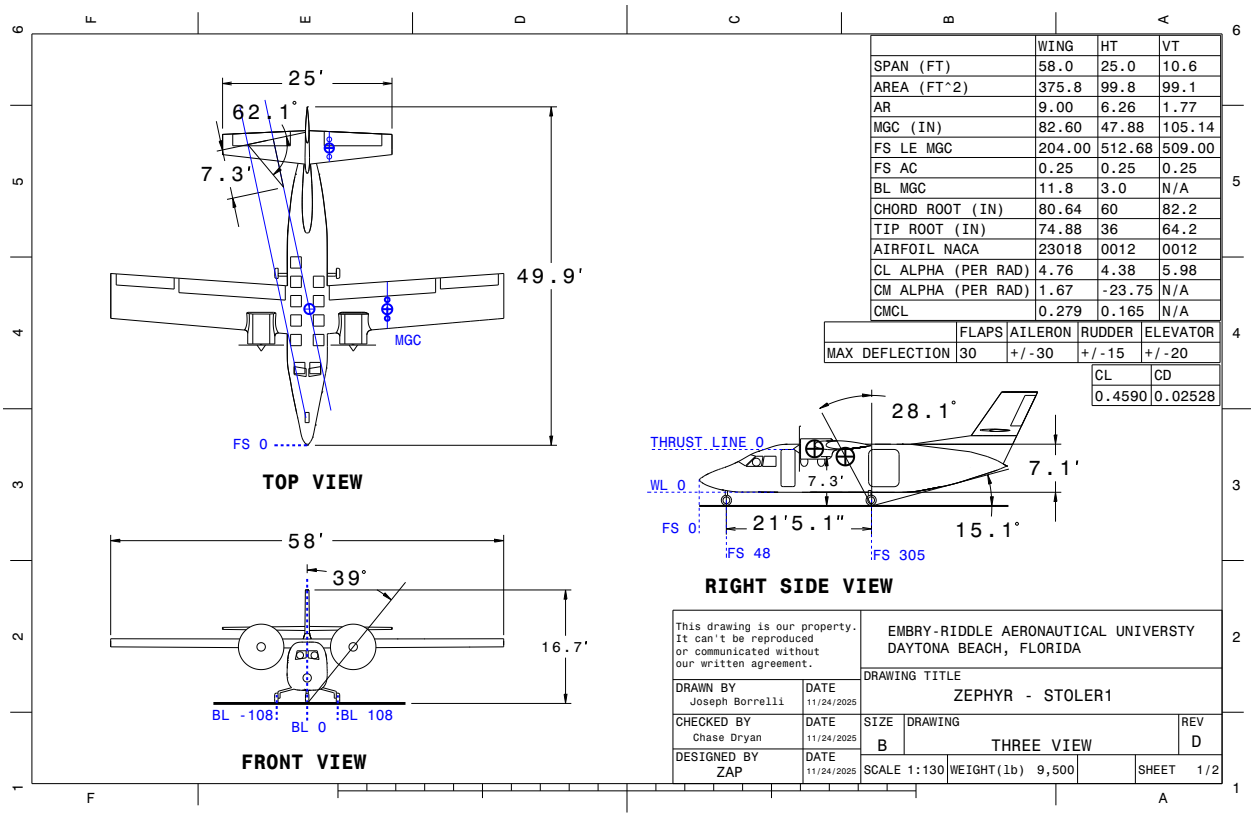

Figure 5-10: CATIA drawing page 1 detailing 3-view, tip over angle, thrust line, waterline, butline, fuselage stations, cg, and MGC values along with geometric values.

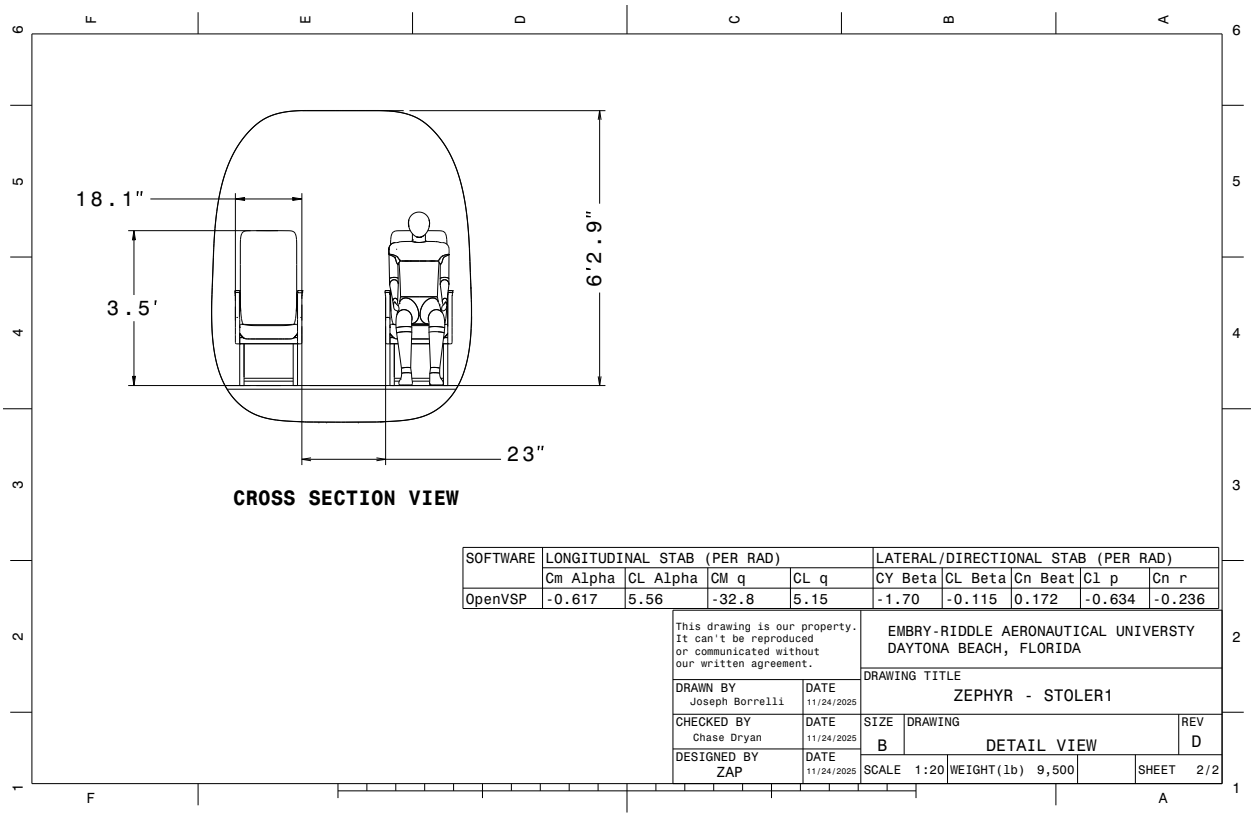

SOFTWARE	LONGITUDINAL STAB (PER RAD)				LATERAL/DIRECTIONAL STAB (PER RAD)				
	Cm Alpha	CL Alpha	CM q	CL q	CY Beta	CL Beta	Cn Beat	Cl p	Cn r
OpenVSP	-0.617	5.56	-32.8	5.15	-1.70	-0.115	0.172	-0.634	-0.236

EMBRY-RIDDLE AERONAUTICAL UNIVERSTY
DAYTONA BEACH, FLORIDA

DRAWING TITLE: ZEPHYR - STOLER1

DRAWN BY: Joseph Borrelli	DATE: 11/24/2025		
CHECKED BY: Chase Dryan	DATE: 11/24/2025	SIZE: B	DRAWING: DETAIL VIEW — REV: D
DESIGNED BY: ZAP	DATE: 11/24/2025	SCALE 1:20	WEIGHT(lb) 9,500 — SHEET 2/2

Figure 5-11: CATIA drawing page 2 detailing internal dimensions and stability values.

5.3 Internal Layout

The internal layout of STOLER-1 was designed to fit specific customer requirements while also being able to be adapted to other various use cases. The majority of the design was based around Cape Air as a launch customer for short commuter flights.

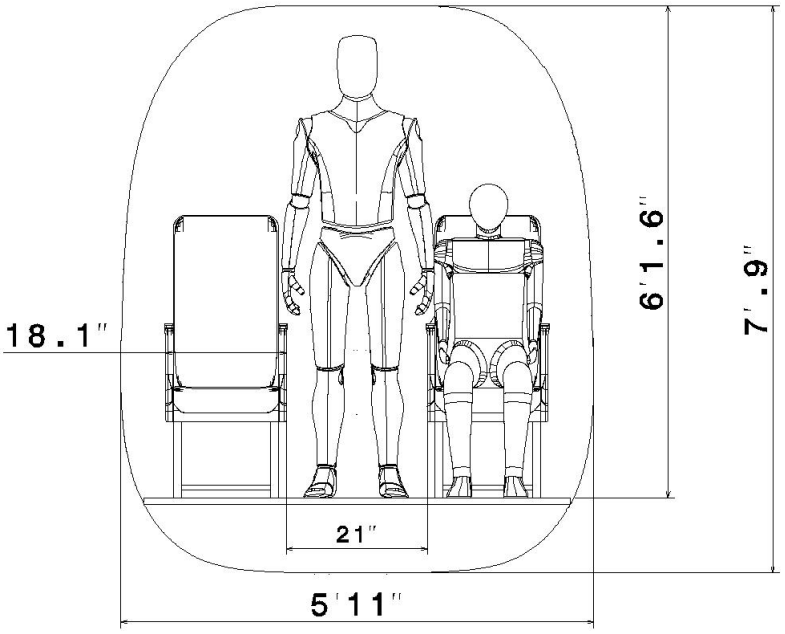

Figure 5-12: CATIA drawing cross-sectional view of the passenger compartment.

The human models are scaled to 5 feet 9 inches, the average American male height, according to the CDC [33].

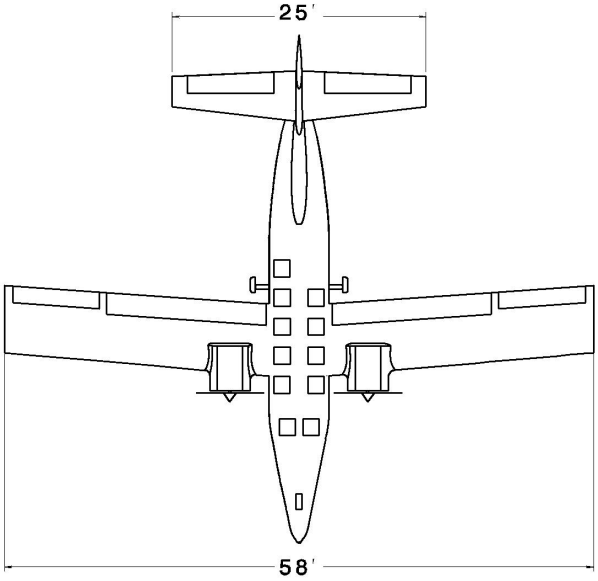

Figure 5-13: CATIA drawing overhead view showing pilot(s) and passenger(s) seating arrangement.

STOLER-1 features:

- 34" Seat Pitch
- 2 Pilots
- 9 Passengers (5 on the left, 4 on the right)

- 21” Isle Width
- 18” Seat Width

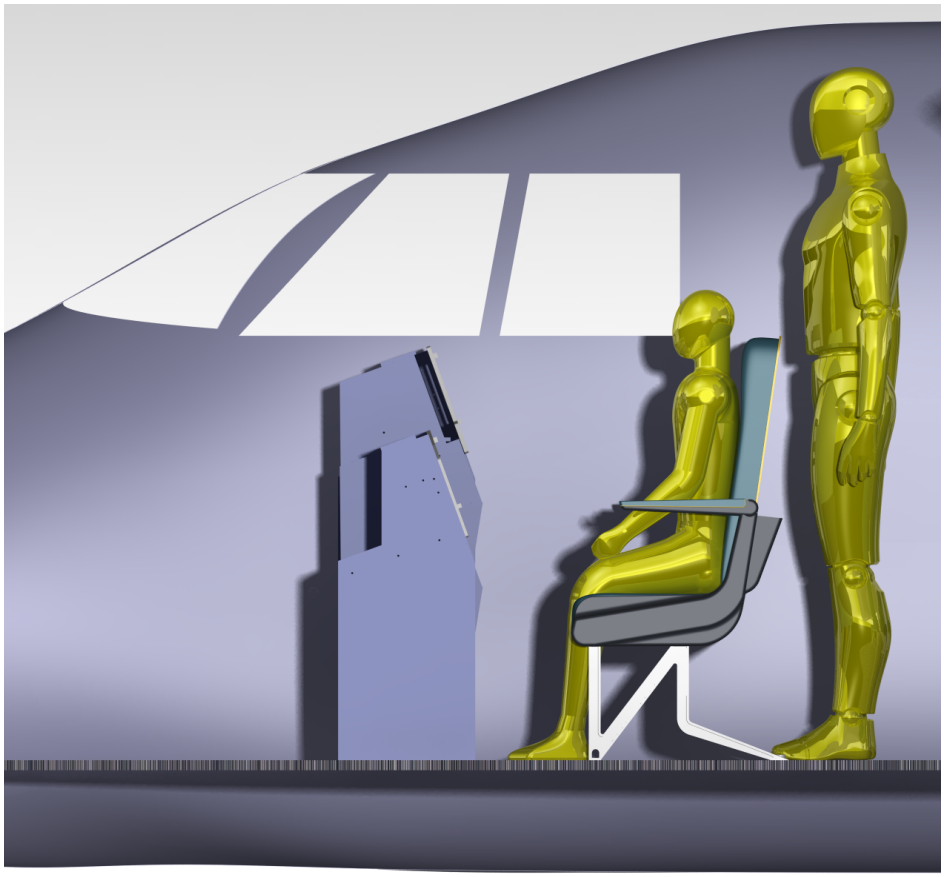

Figure 5-14: CATIA render of the cockpit showing window level and internal cabin space.

STOLER was designed with additional markets in mind, including possible cargo, medical transport, and sky-jumping configurations.

6 Aerodynamics

Following the RFP, the primary rival selected was the Tecnam P2012 Traveller, which is also a nine passenger twin engine commuter aircraft. From manufacturer's report, the wingspan is 46 ft, wing area of 275 ft^2 and a wing loading of 30 lb/ft^2. From information on stall speed and wing loading, a simple calculation can estimate the $C_{L,\max}$ of the aircraft to approximately 2, which falls within the typical values for GA. Wind-tunnel work published on the aircraft shows a representative drag polar, with a minimum drag coefficient for clean configuration of $C_{D,\min} = 0.03$, and a maximum lift to drag ratio of 12–13 for cruise conditions. These characteristics create a baseline for the STOLER-1 design, targeting compatible performance values relative to the Tecnam.

To evaluate the aerodynamics of the STOLER-1, a combination of low and mid fidelity tools were used. OpenVSP was employed to build the base dimensions of the aircraft, and its VSPAERO vortex-lattice method (VLM) solver provides lift curves, drag polars and stability coefficients over a range of angles of attack and control surface configurations. To better represent the aerodynamics analysis, the higher-fidelity panel method FlightStream is being used, primarily to map the pressure-coefficient distribution over the wing, high-lift systems and empennage. Combining VSPAERO and FlightStream complements hand-calculations and spreadsheet methods, building a consistent picture of the aircraft's behavior relative to the rival Tecnam P2012.

6.1 Airfoil Selection

For airfoil selection, three candidates were considered to satisfy STOLER-1's mission. The wing section must serve a high wing, twin-piston STOL aircraft with low landing distance priority and reasonable fuel burn at cruise. The airfoils compared were **NACA 23018**, **NACA 4415**, **NACA 2412**, and **NACA 0012** (used for vertical and horizontal tail) evaluated against five criteria: flapped maximum lift coefficient (($C_{L_{\max,\ \text{flapped}}}$)), stall docility and aileron authority, trim burden, cruise drag, and thickness & flap integration. Graphs in 6-1 show coefficient of lift, moment, drag, and lift-to drag ratio of each airfoil using XFLR5. The primary aerodynamic values are summarized in Table 6-1.

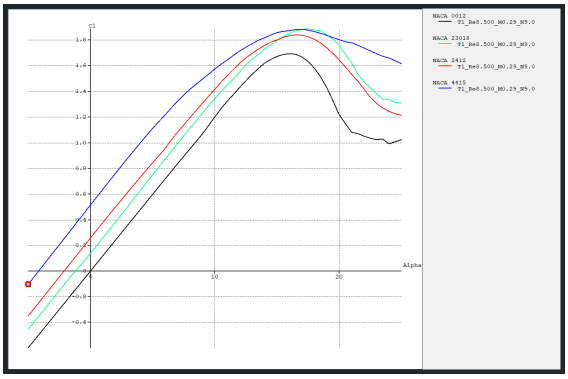

(a) Coefficient of Lift vs. Angle of Attack

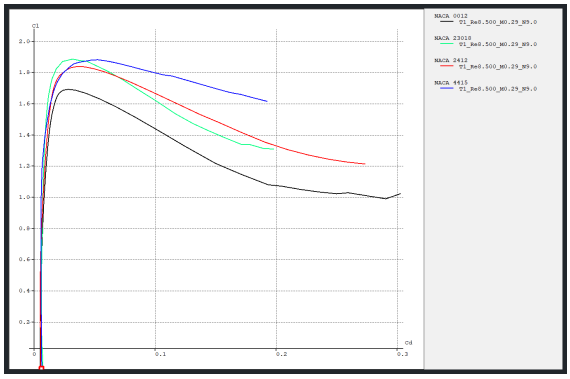

(b) Coefficient of Moment vs. Angle of Attack

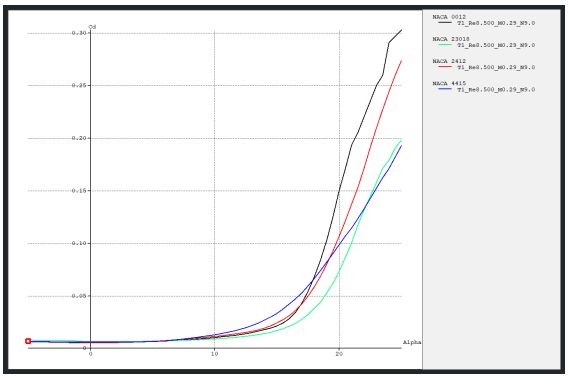

(c) Coefficient of Drag vs. Angle of Attack

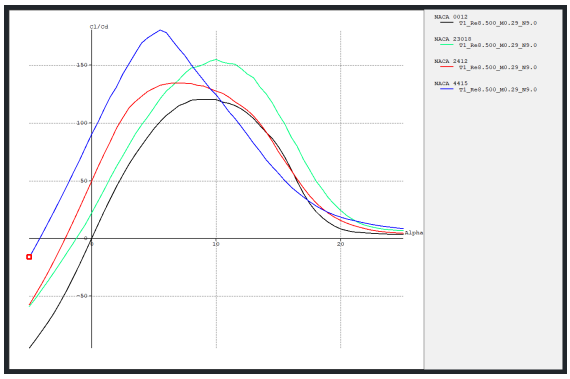

(d) Lift-to-Drag Ratio vs. Angle of Attack

Figure 6-1: Polar Graphs for cruise for NACA Airfoils 2412, 23018, 0012, 4415

Table 6-1: Comparison of candidate airfoils (excluding NACA 0012).

Airfoil Name	Lift Curve Slope $C_{L\,\max}$	Stall AoA (deg)	Linear Range (deg)	$C_{D,\min}$	C_L at $C_{D,\min}$	C_D at Cruise C_L	C_{m0}	L/D at Cruise C_L
NACA 2412	0.11	15	0–12	0.009	0.25	0.0115	-0.05	34.5
NACA 23018	0.11	15	0–12	0.010	0.30	0.0120	-0.08	33
NACA 4415	0.11–0.12	14	0–12	0.095	0.30	0.0115	-0.12	34.5

Additionally, a decision matrix was created to formalize the choice, with criteria weighted as shown in the figure below as well as a vizual representation as a radar plot.

Table 6-2: Airfoil Decision Matrix (scores 1–5; weights sum to 10)

Criterion	**Weight**	**NACA 23018**	**NACA 4415**	**NACA 2412**
$C_{L_{\max,\ \text{flapped}}}$	3	5	4	3
Stall Docility & Aileron Authority	2	4	5	3
Trim Burden	2	4	3	4
Cruise Drag Near Cruise C_L	2	3	4	4
Thickness & Flap Integration	1	5	4	3
Weighted Total (Max 50)	**10**	**42**	**40**	**34**

Note: Scores are 1–5 (5 = best).

Figure 6-2: Radar plot for airfoil selection.

Rationale for Selecting NACA 23018

- **Flap integration:** 230-series sections respond well to Fowler flaps because the airfoil is thick and mildly cambered. This favors higher $C_{L_{\max,\ \text{flapped}}}$ with practical flap chords and slot geometry.
- **Trim burden:** Compared to 4415, NACA 23018 yields a *less negative* pitching-moment coefficient (C_{m_0}). Therefore, the tail must produce less downforce to balance nose-down moments, which is beneficial for STOL approaches and OEI handling. Flap-down moment change ΔC_m remains manageable.
- **Integration margin:** The 18% thickness provides spar depth, gear attachments, and flap-bay volume appropriate for a rugged STOL layout, with minimal penalty elsewhere.
- **Cruise condition:** Polars show a slight penalty in C_D near the trimmed cruise lift coefficient ($C_L \approx$ target value) relative to NACA 2412/4415; however, the low-drag region still spans the cruise C_L. The field-length benefit from higher $C_{L_{\max,\ \text{flapped}}}$ dominates the trade.

Why Other Candidates Were Not Selected

- **NACA 4415:** Offers very forgiving stall controllability and solid flap gains, but carries a more negative C_{m0}. This increases trim drag and tail load, potentially requiring a larger tail arm or tail area to maintain margins.
- **NACA 2412:** A popular GA airfoil with good cruise C_D and benign handling; however, compared to the others it shows the lowest clean $C_{L_{\max}}$ and the thinnest structure (12% thickness), reducing flap-bay depth and structural margin—both undesirable for a STOL mission.

6.2 Wing Geometry

The wing geometry selection was based on STOLER's constraint diagram, aiming to satisfy field–length and climb constraints while maintaining an appropriate wing loading. The required design wing loading is $W/S = 24$ lb/ft^2, which is comparable to competitor aircraft such as the DHC-6 Twin Otter, with a wing loading of 26.2 lb/ft^2 [27]. A small leading-edge sweep was added to the wing to offset minor compressibility effects at cruise speeds. Although cruising at $M = 0.3$ does not produce strong compressibility effects, the sweep also provides a sleeker appearance and improves the overall aesthetics of the aircraft. A positive incidence of $i_w = 3°$ was chosen so that the aircraft can cruise near a level fuselage attitude, improving pilot visibility and overall passenger comfort. Table 6-3 below shows the main values for the wing planform.

Table 6-3: Wing and Empennage Geometric Parameters

Parameter	Symbol	Value
Wing		
Planform area	S_w	375.84 ft^2
Span	b_w	58 ft
Aspect ratio	AR_w	8.95
Root chord	C_r	6.724 ft
Tip chord	C_t	6.236 ft
Mean aerodynamic chord	$\bar{c}$	6.48 ft
Wing loading (TO weight)	W/S	25.1 lb/ft^2
Leading-edge sweep	Λ_{LE}	5°
Wing incidence	i_w	3°
Dihedral	Γ	0°
Geometric twist	ε	0°

6.2.1 Leading Edge Sweep Trade-off

The ZAP team aims for effectiveness, quality, and low-cost aircraft, but another important driver for the STOLER-1 configuration is a modern and sleek design, aesthetically pleasing to the eyes of the customers and passengers. A leading-edge sweep of 5° was chosen for the wing, aiming to satisfy that driver. Additionally, the need for a more-aft center of gravity to improve static margin brought more importance to sweeping the wing, and the implemented change did in fact improve stability. However, sweeping the wing can cause unwanted effects on cost, manufacturing, and structural loads of the aircraft. Firstly, the structure needs to be more robust to sustain the added aerodynamic loads, which increases overall weight, possibly shortening maximum cruise range. Secondly, expensive materials and complex engineering increase the total cost of the aircraft, making it less desirable for customers. Finally, the integration of fuel tanks, flaps, and other systems might become harder during manufacturing and maintenance. Moving forward, the engineering team responsible for STOLER-1 will conduct structural and cost analysis on swept wings to determine the real necessity of the sweep and the best trade-off in this situation.

6.3 High Lift Devices

To keep weight, maintanence demands and structural complexity to a reasonable level while still achieving enough lift for the mission, a single fowler flap system was selected. With high-energy air flowing from the lower surface, the fowler flap allow the boundary layer over the flap to be re-energized, which delays separation and produces increased lift when compared to simpler structures, such as the plain flap. Future configurations of the aircraft might include multi-slotted flaps system depending on customer requirements. The flaps occupy about 54% of each wing semi-span, and 33% of the mean aerodynamic chord. With the placement closer to the wing root, the flaps promote root-first stall behavior, maintaining aileron effectiveness near stall speeds. Ailerons are placed on the outboard portion of the wing with a span of about 30% of the wing semi-span and 25% of the mean chord. This configuration provides enough roll control given the maneuvers required for the aircraft. The horizontal tail houses the elevators, which span roughly 81% of the semi-span and about 38% of the chord. The large span of the elevator ensures decent pitch authority for STOL operations, and the chordwise size ensures little complications regarding its structure and hinge moments. The control surfaces together support the aircraft's short-field performance without the need for complicated structures and machanics. Main values are listed in Table 6-4

Table 6-4: Control surface size as percentage of reference span and chord

Surface	Reference	Spanwise extent [% span]	Chordwise extent [% chord]
Flap	Wing semi-span, wing MAC	54.1	32.9
Aileron	Wing semi-span, wing MAC	29.5	25.4
Elevator	HT semi-span, HT chord	81.0	37.5

With a max flap deflection of 30°, the values for zero angle of attack lift coefficient, zero-lift drag coefficient, lift-coefficient at trim and drag coefficient at trim are listed in 6-5.

Table 6-5: Lift and drag coefficients at zero lift and trim for flap deflections.

Flap deflection	C_{L0}	C_{D0}	C_L at trim α	C_D at trim α
0°	0.189	0.01593	0.459	0.01681
10°	0.500	0.02600	0.780	0.04400
20°	0.762	0.03140	1.048	0.07150
30°	0.973	0.04200	1.243	0.09720

6.4 Lift and Drag Models

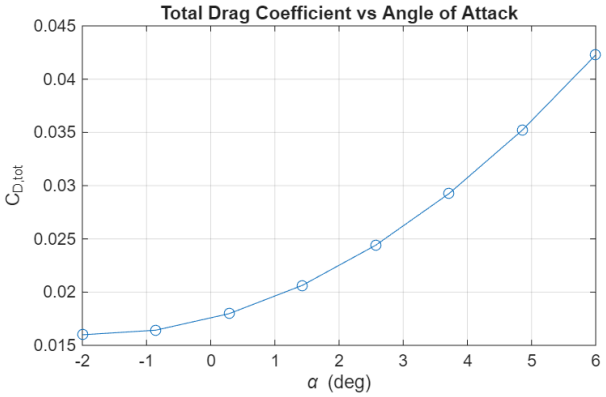

(a) Total drag coefficient $C_{D,\text{tot}}$ vs. angle of attack α for the STOLER-1.

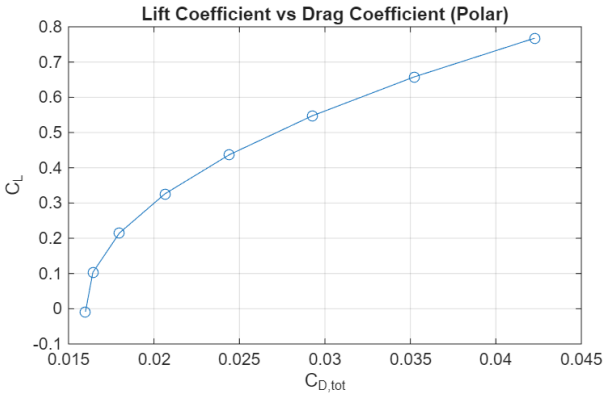

(b) Lift coefficient C_L vs. drag coefficient C_D (drag polar) for the STOLER-1.

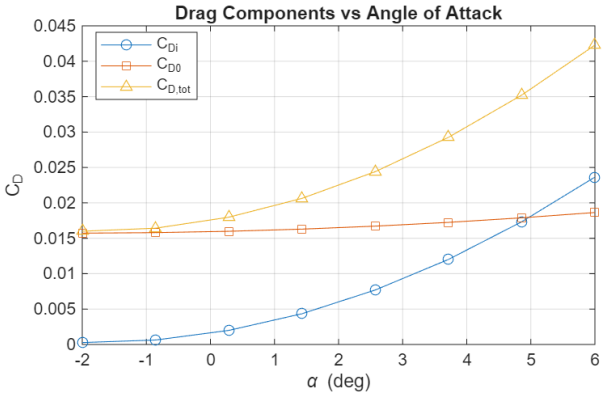

(a) Parasite, induced, and total drag coefficients vs. angle of attack α.

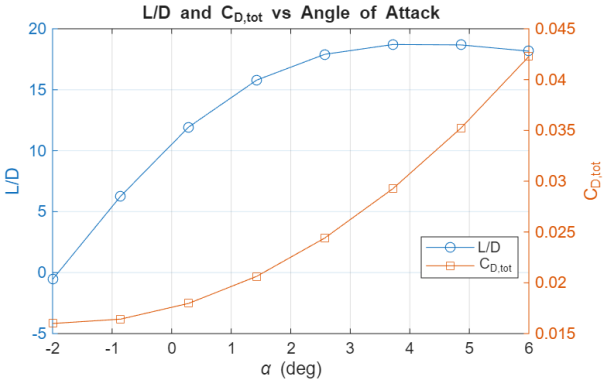

(b) Lift-to-drag ratio L/D and total drag coefficient $C_{D,\text{tot}}$ vs. angle of attack α.

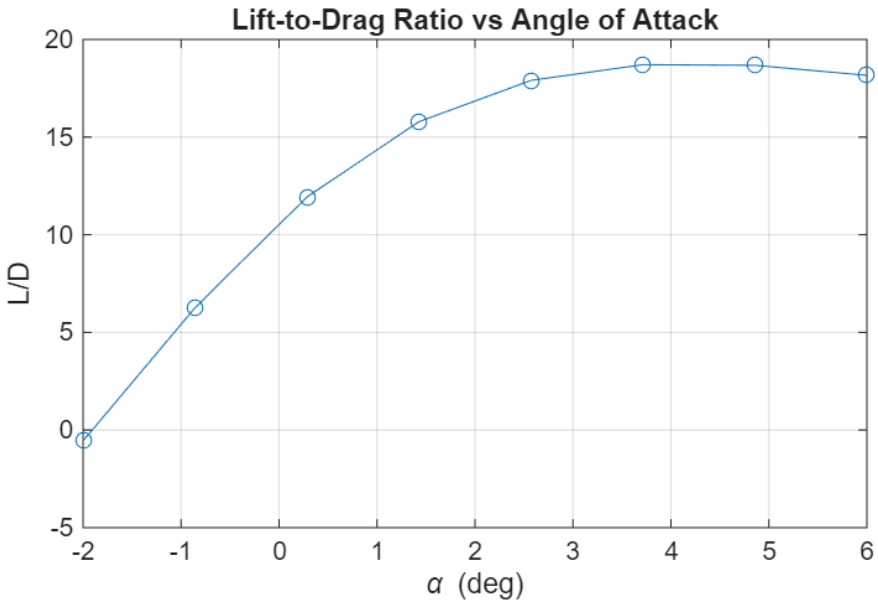

Figure 6-5: Lift-to-drag ratio L/D vs. angle of attack α.

The drag polars for the STOLER-1 were generated using VSPAero data for clean configuration at cruise, and represent key parameters that define the efficiency of the aircraft. Figure 7-6 shows how much lift compared to drag the aircraft experiences at different angles of attack. Cruising at a trim alpha of 2.8, the Lift-to-drag ratio is 18.3, which is desirable and within range of similar aircrafts. Beyond the trim angle of attack, the aircraft generates more lift with the high cost of drag, which is not desirable for the operation. Plotting L/D and CDtotal on the same highlights the trade-off between efficiency and drag increase. At the L/D peak, the drag coefficient is still relatively small, meaning that any increase in angle of attack will not greatly penalize performance, enforcing decent handling quality. However, the drag breakdown in Figure 7-4 displays a rapid increase in induced drag at higher angles of attack, which is undesirable for cruise but acceptable in takeoff and climb. Overall, the drag polars indicate a realistic design with expected trends. Induced and parasite drag are compliant with the chosen aspect ratio of the wing and tail volume. Table 6-6.display the main aerodynamic values for the aircraft in clean-cruise configuration.

Table 6-6: Cruise aerodynamic parameters for clean configuration

Parameters (clean config)	**Value**
Induced factor, K	0.04461
Oswald efficiency, e	0.797
Cruise angle of attack, α	2.80°
Lift coefficient, C_L	0.4590
Zero-lift drag, C_{D0}	0.01681
Induced drag, C_{D_i}	0.00847
Total drag, $C_{D,\text{tot}}$	0.02528
Lift-to-drag ratio, L/D	18.14

6.4.1 Aerodynamics Sensitivity Analysis

The aerodynamic data previously analyzed was generated using OpenVSP VSPAERO for a preliminary analysis. In VSPAERO's vortex-lattice method, lifting surfaces are represented by a lattice of horseshoe vortices over the camber surfaces. The model assumes irrotational and inviscid flow, solving for the zero normal velocity in each panel. This method predicts lift distribution and stability derivatives very efficiently, being a great tool to validate wing and tail geometries and incidences. In contrast, the model disregards

thickness, not fully solving for the fuselage and intersections with wing and tail. Therefore, induced drag is based on the idealized lifting-surface solution, often underpredicting values for the drag components for the complete aircraft. To validate the data generated by VSPAERO, the 3-D panel method by FlightStream was employed in our design.

FlightStream solves the flow over the actual geometry of the STOLER-1, including the junctions between fuselage and the lifting surfaces as seen by 6-6, which shows the pressure coefficient map along the aircraft's surface.. While STOLER-1's mission does not include operations above $M = 0.3$, the compressible Prandtl–Glauert correction model was chosen to account for any low-Mach compressibility effects that the aircraft may experience, even though such effects will be insignificant given the low velocities. On top of this solution, FlightStream incorporates viscous coupling and a boundary-layer model that spans along the surface, enabling estimations for skin-friction drag, transition, and separation and feeding it back to the main inviscid model. Those extra steps allow for the capture of both induced drag and viscous drag caused by local pressure gradients and interference effects, resulting in higher and more realistic predictions for drag levels than a pure vortex-lattice method.

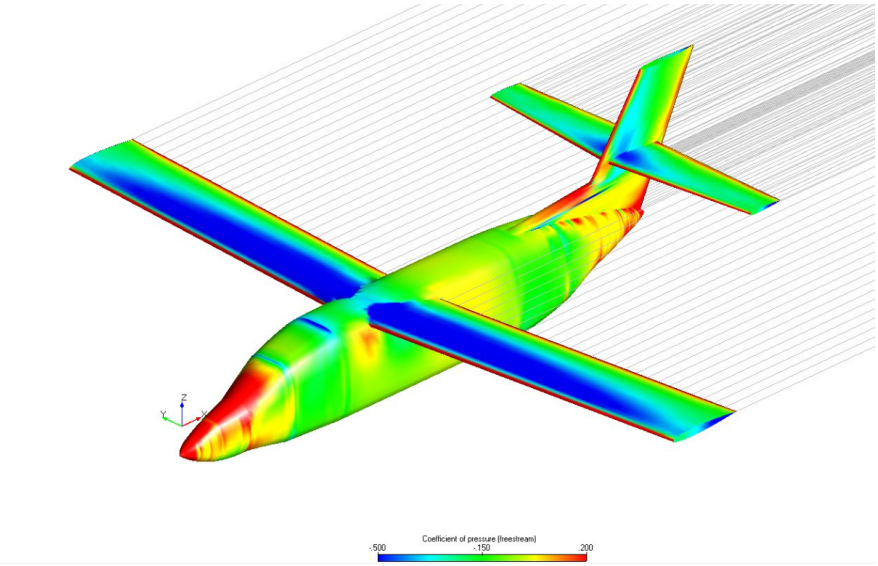

Figure 6-6: FlightStream pressure coefficient map for STOLER-1

The geometry developed in OpenVSP was exported to FlightStream where the mesh could be refined for a better analysis, fixing any defects on the surfaces and junctions. Leading edges and wake-termination nodes were defined and a similar angle-of-attack sweep run was done to compare the results with VSPAERO. For STOLER-1, both solvers predict an almost identical lift curve slope as seen in 6-7, being essentially parallel over the linear range, validating the effectiveness of the wing-tail design and confirming that lift analysis is not very sensitive to solver choice. The discrepancies start appearing when the drag of the aircraft is analyzed. As expected beforehand, FlightStream predicts a higher induced drag, and also outputs the boundary-layer drag. The two types of drag are summed so a total drag comparison between the models is possible. Table 6-7 displays the values from both solvers.

The main discrepancies between the solvers appear in the drag polar and lift-to-drag ratio. In the cruise α range, VSPAERO predicts a $C_{D0} = 0.016$ and a maximum $L/D = 18.7$ at $\alpha = 3.7°$. Using the same geometry, FlightStream predicts C_D values roughly 25–30% larger across the α sweep, corresponding to a maximum L/D of 14 occurring at a slightly higher angle of attack around $\alpha = 5°$, as seen in 6-8. These ranges align with published data for similar commuter aircraft. [32] performed wind-tunnel analysis on a scaled model of the Tecnam P2012 Traveller, reporting agreement in lift and pitching-moment curves but an underprediction of drag in numerical analysis, reinforcing the optimistic drag estimation of lower

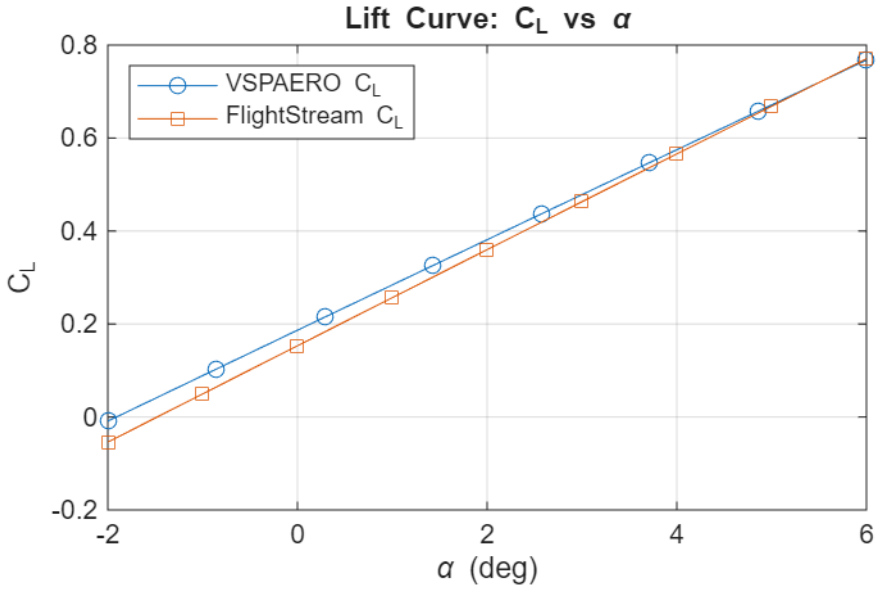

Figure 6-7: Lift curve comparison between VSPAERO and FlightStream.

Table 6-7: Comparison of VSPAERO and FlightStream aerodynamic predictions for STOLER-1.

Quantity	Symbol	Condition	VSPAERO	FlightStream
Trim condition ($\alpha_{\text{trim}} = 2.8°$)				
Lift coefficient	C_L	trim	0.4590	0.4425
Parasite drag	C_{D0}	trim	0.01681	0.01442
Induced drag	C_{Di}	trim	0.00847	0.02045
Total drag	$C_{D,\text{tot}}$	trim	0.02528	0.03487
Lift-to-drag ratio	L/D	trim	18.14	12.69
Drag polar fit (least-squares over α range)				
Fitted zero-lift drag	$C_{D0,\text{fit}}$	polar	0.01593	0.02428
Induced-drag factor	K	polar	0.04461	0.05475
Oswald efficiency	e	polar	0.797	0.650
Max lift-to-drag ratio	$(L/D)_{\max}$	polar	18.71 @ 3.71°	13.72 @ 5.00°

fidelity tools. The article also shows that the STOLER-1 is similar in performance to the Tecnam P2012, as experimental values on wind-tunnel showed maximum L/D values of approximately 11–12. To further validate the aerodynamic performance of the STOLER-1, wind-tunnel experiments with scaled models would be a valuable and viable choice.

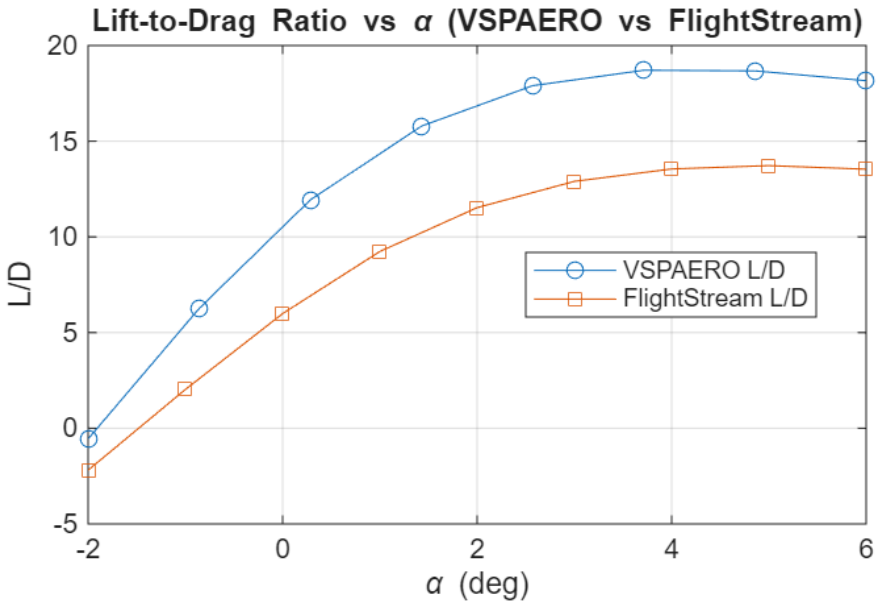

Figure 6-8: Lift-to-drag ratio comparison between VSPAERO and FlightStream.

7 Propulsion

The propulsion system of the aircraft is the driving force behind the performance and usability of the aircraft. This analysis will look at the propulsion system selected for the STOLER-1. This analysis starts with looking at the engines that were considered to be used to power the STOLER-1. The analysis goes on to look at the propeller, along with its sizing and reasoning behind design choices for the propeller. Following that, the analysis goes into the thrust that the engines generate, and how that is variable with both airspeed and altitude.

7.1 Engine Selection

The engine selected to power the STOLER-1 was the Lycoming IO-720. This engine was primarily selected due to its high power output, relatively low acquisition cost, and coming from a reputable engine manufacturer in Lycoming. The table below shows the decision matrix used to compare the engines considered for the STOLER-1, and provides more reasoning behind the decision to use the IO-720. The data in the table was taken from Refs. 5,6,7,8,9, and 10.

Table 7-1: Engine decision matrix.

Category	Weight	Lycoming IO-720	Continental CD-300	PT6A-140	DHK235A4	Lycoming TEO-540-C1A
Piston	0.05	10	10	0	10	10
Power	0.20	9	6	10	2	9
Jet A	0.05	0	10	10	10	0
Maintainability	0.10	9	7	5	7	9
Cost	0.30	7	6	1	6	4
Certification	0.10	10	10	10	10	10
Size	0.20	5	5	5	7	5
Total (weighted)	**1.00**	**7.3**	**6.7**	**5.3**	**6.3**	**6.4**

From the above table, it can be seen that the Lycoming IO-720 best met the requirements for the aircraft. This was mostly due to its high power output and relatively low cost. It also had the advantage of being a piston engine, which is more desirable to the launch customer and easier to maintain. However, the IO-720 does not possess the ability to use Jet A, which means it can only be used in North America, as other areas

of the world do not use AvGas. This will likely be remedied by creating a higher performance model of the aircraft using a turboprop engine like the PT6A-140. Doing this would cause the aircraft to cost more, but ideally would also open up a larger market for the aircraft as it would have better performance and be usable in more places.
The engine is not the only part of the propulsion system of the aircraft. A propeller is needed to transfer the power of the engine into thrust for the airplane. It was found the STOLER-1 propeller needed to be 80.5 inches in diameter. This was found using the below equation from Ref. 4.

$$D_p = K_p * P_{BHP}^{1/4} \tag{3}$$

Using the horsepower rating of the Lycoming IO-720 (400 hp) (Ref. 8) and the K_p was taken from Ref. 4 for a four-bladed propeller to be 18.0. The decision was made to use four blades for better noise reduction and better efficiency. The decision was also made to make the propellers out of carbon fiber so they could be light, strong, and aerodynamic. Finally, it was decided to go with a constant-speed propeller to have the best possible performance at all phases of flight. These decisions ultimately made the propeller a more expensive part of STOLER-1, but it was considered to be worth it to get the most out of the engines as possible. The propeller efficiency was also modeled using the matrix method presented in Ref. 4. The estimated propeller efficiency is shown in Figure 7-1.

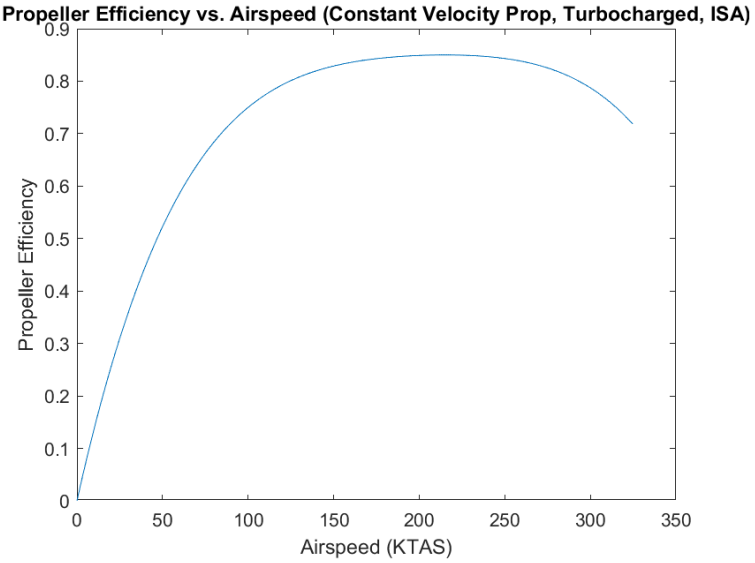

Figure 7-1: Propeller efficiency vs. airspeed

It can be seen that the propeller efficiency stays at or near it's highest value over a large range of airspeeds. This is typical of a constant-speed propeller, which changes pitch with increases in speed to keep the propeller efficiency up.

7.2 Thrust Modeling

Piston propeller engines are considered constant power devices. This means they have variable thrust depending on many factors, such as propeller efficiency, altitude, and most importantly speed. The thrust of STOLER-1 was modeled using two different methods presented in Ref. 4. The two plots created for these thrust models are shown below in Figure 7-2 and Figure 7-3.

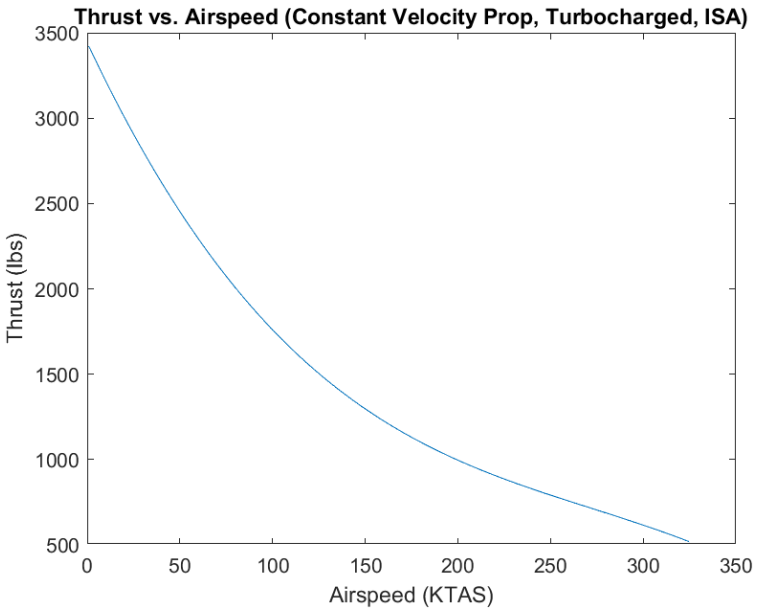

Figure 7-2: Thrust vs. Airspeed from MATLAB

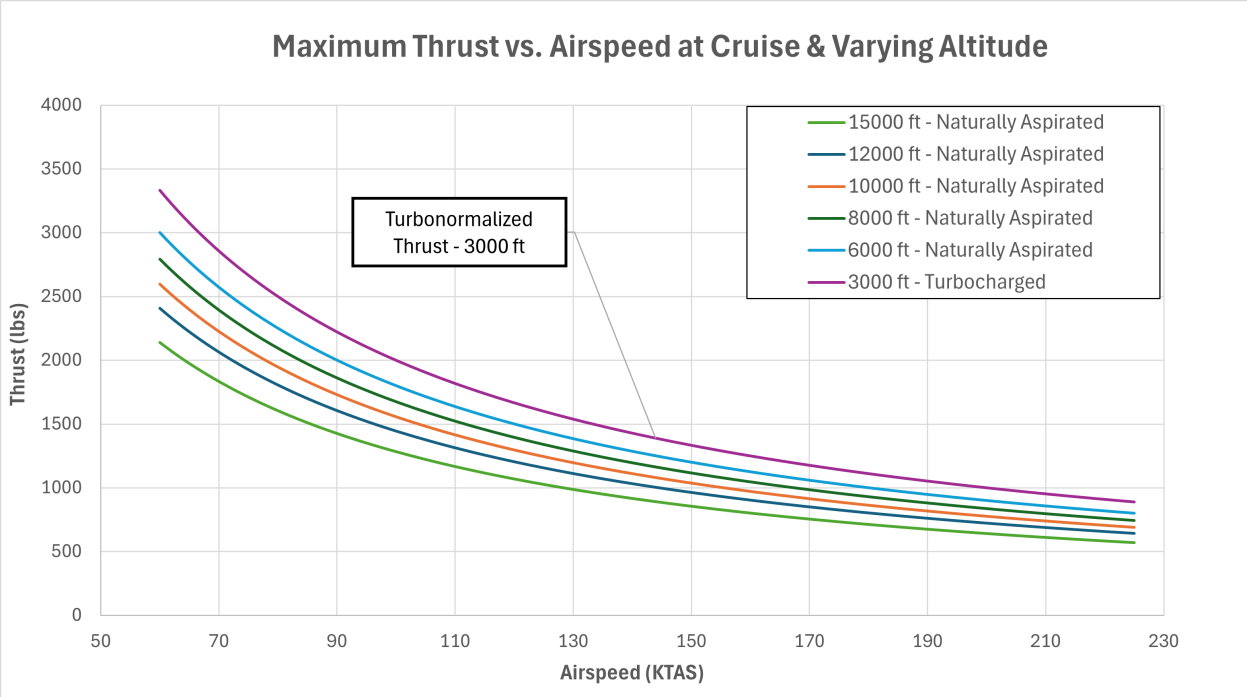

Figure 7-3: Thrust vs. Airspeed at Altitude

Both of these plots are relatively close for the thrust at 3000 ft, which is approximately the pressure altitude of the pressure the turbocharger can keep the engine at. This means the engine can hold this performance up to the cruising altitude of 12000 ft. From the excel graph, it can be seen why it was decided to use a turbocharger. The turbocharger greatly increases the available thrust at 12000 ft, allowing for much improved performance in cruise. The addition of turbochargers also allows for pressurization of the cabin, something other similar aircraft do not do. This is done by taking bleed air from the engine manifold, which is kept at the higher pressure, and bringing it to the cabin to pressurize it. This does cause a slight dip in performance

of the engines, which is why it was decided to use a pressure altitude of 3000 ft for engine performance instead of the actual approximately 2700 ft where the actual manifold air pressure is [30].

From the thrust and using the drag coefficient found through the aerodynamic analysis of STOLER-1, a power required versus power available plot can be created. The power available is found by multiplying the thrust by the airspeed, and the power required is found by multiplying the drag by the airspeed. The plot is shown below in Figure 7-4.

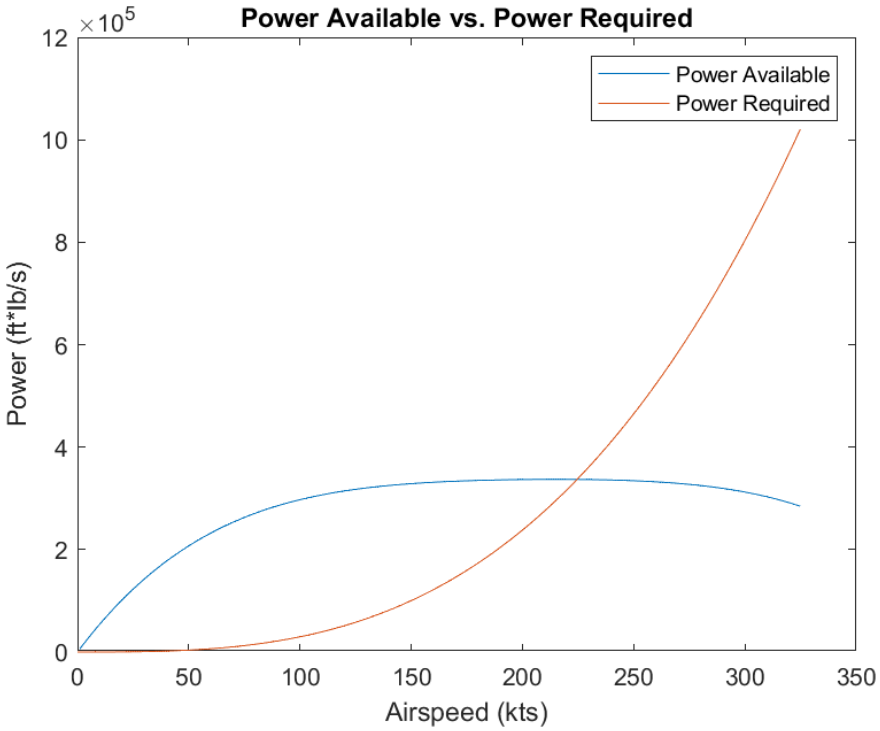

Figure 7-4: Power Available vs. Power Required

One of the most important metrics that can be gained from this where the maximum obtainable speed of the aircraft is with the engines at full power. According to this plot, that speed is about 225 kts true airspeed. While this is not the maximum speed with maneuvers like dives, it is the maximum straight-line speed of the aircraft at cruise. This proves that cruising at 215 kts true airspeed is obtainable for this aircraft, which is a major performance parameter and selling point of STOLER-1.

7.3 OEI Engine Performance

The ability to operate with one engine inoperable is very important for a multi-engine aircraft, like the STOLER-1. A well-designed multi-engine aircraft should be able to have one engine stop working and be able to continue to safely operate. For STOLER-1, part of the aircraft's performance with one engine inoperable was assessed with another power available vs. power required plot, this time only using the thrust produced by one engine. This plot was created with the same code as in Appendix A, just with different variables, and is shown below in Figure 7-5.

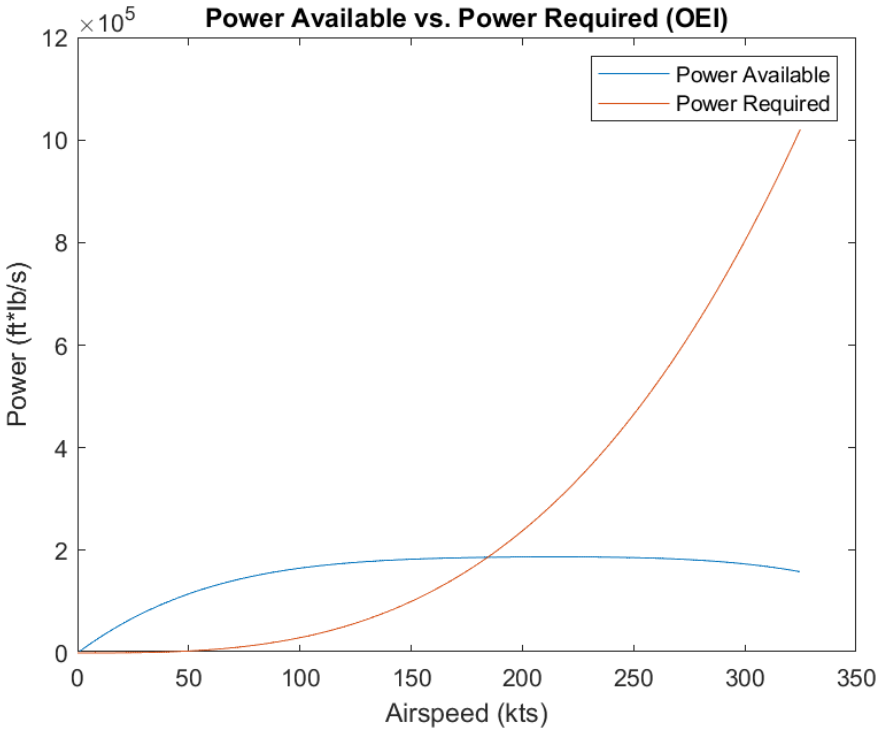

Figure 7-5: Power Available vs. Power Required for One Engine Inoperable

With one engine inoperable, the STOLER-1 still maintains a relatively high maximum obtainable speed of about 181 kts true airspeed. This means that with one engine out the STOLER-1 is still capable of flying at an operable speed, and either continuing to its destination, or more likely diverting to a nearby airport for repairs. This showcases the safety of the STOLER-1, as with one engine inoperable the aircraft can continue to operate with reduced performance. Also, worth noting, the thrust plot for one engine inoperable is not shown here as it would be the exact same as the thrust plot for both engines operating, just with the values at half their original values.

8 Stability & Control

The stability and controls of an aircraft are vital in defining an aircraft's handling qualities and safety across various flight conditions. The analysis calculates the forces and moments the aircraft experiences at different phases in flight for the aircraft to maintain equilibrium and respond to pilot inputs. Each of the sections below will discuss the tail and control surface sizing, as well as the longitudinal, lateral/directional, and dynamic stability of the STOLER-1. The DHC-6 Twin Otter is considered a rival aircraft to STOLER-1 for stability and controls. Below in table 9-1 are the stability derivatives of the DHC-6 Twin Otter referenced from Gudmundsson [4]

The DHC-6 Twin Otter is considered a stable aircraft that is significantly easier to handle in various flight conditions. The values for each stability derivative presented in Table 9-1 were considered when developing the values for STOLER-1. The vertical tail of the DHC-6 Twin Otter is large compared to other STOL aircraft, but the emphasis on handling qualities was important in the decision process of the STOLER-1. The DHC-6 Twin Otter control surface and tail sizing played a significant role in the design process of the STOLER-1.

The approach that was taken in designing the stability and controls of the aircraft considered a range of values for general aviation aircraft provided by Gudmundsson [4]. The aircraft was modified a multitude of times to achieve a stable aircraft in different phases of flight with various flap angles. The most significant modification was to the vertical tail, which added a dorsal fin and increased the span and area.

Table 8-1: DHC-6 Twin Otter stability and control derivatives.

Stability derivative	**Value (per rad)**
Longitudinal stability (C_{m_α})	-1.200
Directional stability (C_{Y_β})	-0.866
Dihedral effect (C_{L_β})	-0.119
Directional stability (C_{N_β})	0.087

8.1 Empennage

The cruciform tail configuration places the horizontal tail at the center of the vertical tail, forming a cross shape when viewed from the front or rear of the aircraft. This configuration was selected as a compromise between a low tail and T-tail design that is typically seen with STOL aircraft. The cruciform placement is beneficial in removing the horizontal tail out of the wash produced by the engine and wake generated by the wing. This ensures the elevator has clean airflow that maximizes pitch control for longitudinal stability. This design also prevents an increase in stress on the structure due to weight, as the T-tail configuration typically produces.

The vertical tail involves a dorsal fin (Triangular fairing connecting the vertical tail to the leading edge of the fuselage) that improves the directional stability of the aircraft. The role of the dorsal fin is to maintain airflow over the root of the vertical tail into the rudder at large sideslip angles. This delays the flow separation, which is important during engine-out maneuvers where directional stability is required.

The NACA 0012 was selected for both the vertical and horizontal tails' airfoils. This is a symmetric airfoil, which is ideal with tail surfaces because lift needs to be produced in both directions in different areas of flight. This is also a predictable airfoil with a good lift-curve slope (C_{L_α}), making it easy to manufacture. The lift-curve slope is important to the stability of the aircraft as it is directly proportional to the overall effectiveness of the tail.

The tail volume coefficients (V_H,V_V) for general aviation-twin engine aircraft, STOLER-1, and DHC-6 Twin

Otter are shown in Table 9-2. The STOLER-1 tail volume coefficients are higher than typically seen with general aircraft and its competition. The horizontal tail volume coefficient being higher enhances the longitudinal stability and control, creating a more statically stable aircraft. The vertical tail volume coefficient is greater because this improves directional stability, especially for one-engine-out safety.

Table 8-2: Tail volume coefficients.

Aircraft	**Horizontal tail,** V_H	**Vertical tail,** V_V
General aviation (twin engine)	0.800	0.0700
DHC-6 Twin Otter	0.918	0.0783
STOLER-1	1.040	0.0850

8.2 Control Surface Sizing

The primary goal in sizing both the horizontal and vertical tails was to improve stability. The horizontal tail sizing was not changed often throughout the design process, unlike the vertical tail. The vertical tail underwent significant changes throughout, as previously discussed in Section 9.1; the addition of the dorsal fin was significant in improving the directional stability. The tail arms also played a significant role in the sizing of the tails. In table 9-3 and 9-4, the sizing of both the horizontal and vertical tail is displayed.

Table 8-3: Horizontal tail geometric parameters.

Parameter	**Value**
Horizontal tail area (S_H)	99.75 ft^2
Horizontal tail span (b_H)	25.00 ft
Horizontal tail aspect ratio (AR_H)	6.27
Horizontal tail taper ratio (λ_H)	0.596
Horizontal tail arm (l_H)	25.4 ft

Table 8-4: Vertical tail geometric parameters.

Parameter	**Value**
Vertical tail area (S_V)	64.71 ft^2
Vertical tail span (b_V)	11.31 ft
Vertical tail aspect ratio (AR_V)	1.77
Vertical tail taper ratio (λ_V)	0.781
Vertical tail arm (l_V)	23.7 ft

A trade study was conducted to assess the impact of moving the tails closer to the center of the fuselage rather than back. This would impact the stability and maneuverability of the aircraft in different phases of flight. In Table 9-5, the trade study was carried out by moving the tail arms and the area by $\pm 10\%$. Increasing the tail arms improved the stability of the aircraft, but reduced maneuverability. This resulted in the design of the cruciform tail and the development of the dorsal fin to improve stability while maintaining a level of maneuverability that pilots would be able to utilize.

Table 8-5: Tail arm sizing trade study.

Parameter	**0%**	**+10%**	**-10%**
Horizontal tail arm, l_H (ft)	25.40	27.94	22.86
Vertical tail arm, l_V (ft)	23.70	26.07	21.33
Horizontal tail area, S_H (ft^2)	99.75	109.73	89.78
Vertical tail area, S_V (ft^2)	99.09	109.00	89.18

8.3 Trim Configurations

Maintaining trimmed flight is fundamental to longitudinal stability. This section outlines the process used to determine the control surface deflections necessary to trim the aircraft across three flight phases: takeoff, cruise, and landing. Utilizing XFLR5 for airfoil flap characteristics and OpenVSP for full aircraft aerodynamic analysis. The required trim deflections for both the elevator (δ_e) and flaps (δ_f) are calculated and shown in Table 9-6. The purpose of analyzing the aircraft at trim is to ensure the horizontal tail and elevator have the required controls throughout the flight envelope while maintaining a stable aircraft.

Table 8-6: Trim deflections at key flight phases.

Flight phase	**Flap deflection, δ_f (deg)**	**Elevator deflection, δ_e (deg)**
Takeoff	20	15
Cruise	0	0
Landing	30	10

8.4 Longitudinal Stability

The longitudinal stability of the aircraft was determined using VSPAero Vortex Lattice Method. The values were validated using MATLAB to recalculate the derivatives, ensuring the accuracy of the values. Each longitudinal stability derivative and the static margin were obtained to comply with the flight envelope. Each derivative and static margin was given a range to ensure the aircraft was stable throughout the flight envelope and fit the criteria of a general aviation aircraft [4].

Static margin is defined by the distance between the center of gravity (CG) and the stick-fixed neutral point (NP). For an aircraft to be statically stable the static margin should be positive. Below in Table 9-7 is the static margin in the best and worst case scenario. For the best-case scenario, the CG is forward, creating a larger static margin, resulting in more static stability. For the best-case scenario, the aircraft has 2 pilots with no passengers or cargo. For the worst-case scenario, the static margin is greater than the best-case, but still makes a statically stable aircraft. The worst-case scenario is that the aircraft has 1 pilot with a full passenger and baggage load. For both scenarios the static margin is acceptable, and no further accommodations are needed. In Figure 9-1, the center of gravity and neutral point location are displayed on STOLER-1.

Table 8-7: Static margin scenarios.

Scenario	**CG location (ft)**	**Neutral point location (ft)**	**Static margin (%)**
Best case (forward CG)	20.55	22.26	18.00
Worst case (aft CG)	20.80	22.26	22.53

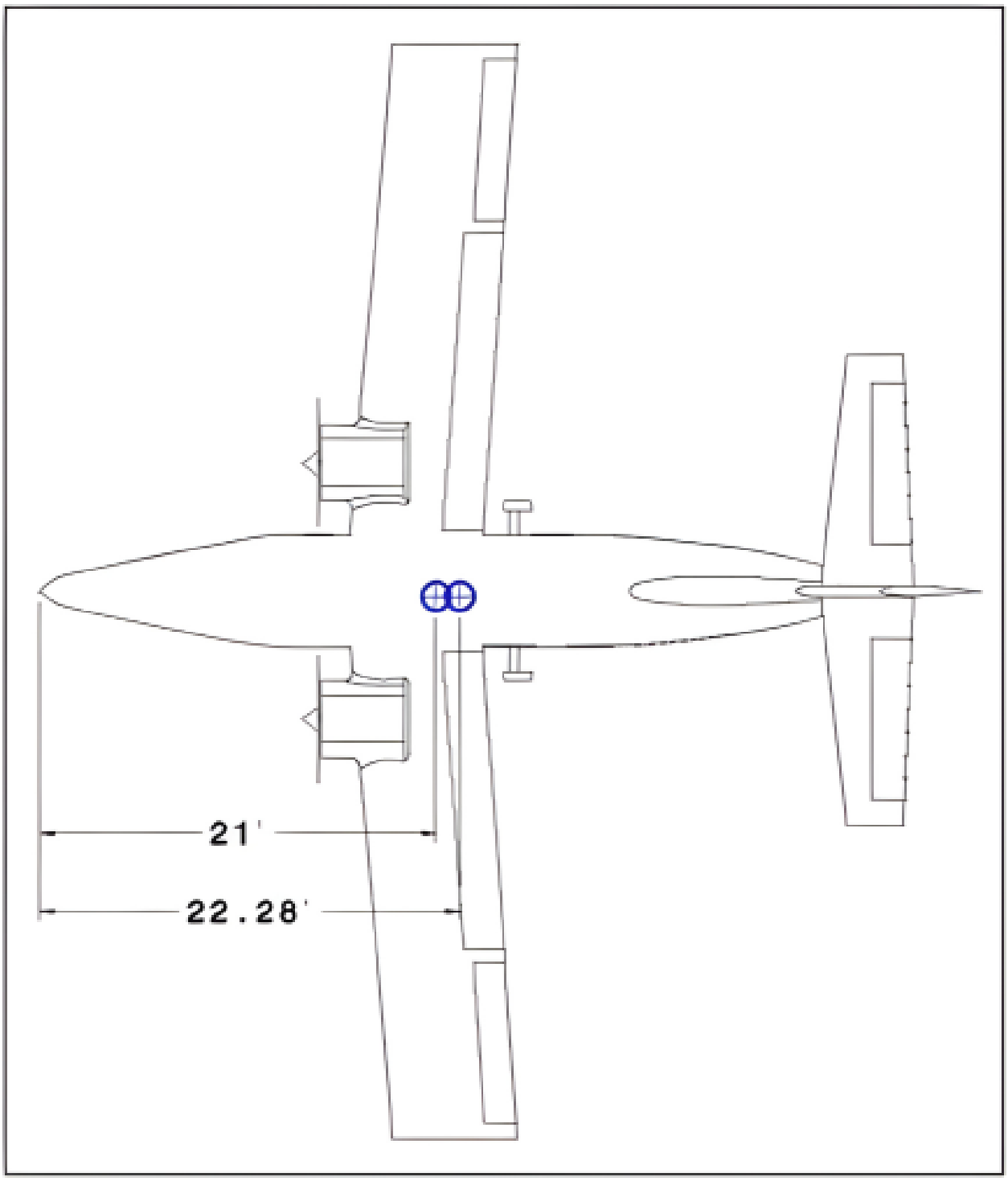

Figure 8-1: Location of the center of gravity and the neutral point relative to STOLER-1

The longitudinal stability derivatives represent how aerodynamic forces and pitching moment change in response to small changes in the angle of attack and pitch rate. In Table 9-8 each of the longitudinal stability derivatives is displayed with the calculated value obtained from analysis on VSPAero. The primary derivatives of longitudinal stability are C_{l_α}, C_{M_α}, C_{L_q}, C_{M_q}. The key values are C_{l_α} and C_{M_α} for the STOLER-1 to determine if the aircraft is longitudinally stable. The derivative C_{l_α} measures the change in lift against the angle of attack, which is the lift-curve slope. This must be a positive value which indicates the aircraft is

generating more lift as the angle of attack increases. The derivative C_{M_α} is the most important derivative for static stability. The value must be negative, indicating that as the angle of attack increases, a more negative pitching moment is generated by the nose of the aircraft. The pitch-damping derivatives C_{L_q} and C_{M_q} are vital for the aircraft to be stable in different pitching scenarios. C_{M_q} is a large negative value indicating there is a strong pitch damping resisting pitching motions for the aircraft, which is important for the heavy damping ratio for the short period mode displayed in Table 9-9.

Table 8-8: Longitudinal stability derivatives.

Derivative	**Value**
C_{M_α}	-0.617 per rad
C_{L_α}	5.56 per rad
C_{M_q}	-32.8 per $\hat{q}$
C_{L_q}	5.15 per $\hat{q}$

The dynamic stability envelope illustrates the aircraft's longitudinal Short-Period Mode (SP) and Phugoid Mode (LP) in relation to flying quality specifications. The envelope plots the natural frequency ($\omega_{n_{SP}}$, $\omega_{n_{LP}}$) in radian per second against the damping ratio (ζ_{SP}, ζ_{LP}). The flying quality specifications are divided into three regions, labeled as levels 1, 2, and 3. Level 1 is highly desirable, level 2 is acceptable, and level 3 is controllable but deficient. For all flight phases, the Short-Period and Phugoid Modes calculated in Table 9-9 fall within the level 1 flight specification throughout the operational envelope.

Table 8-9: Longitudinal dynamic stability characteristics.

Dynamic mode	**Natural frequency, ω_n (rad/s)**	**Damping ratio, ζ**	**Period, P (s)**	**Flying specification**
Short period	4.73	0.82	2.3	Level 1
Phugoid	0.0965	0.026	65.1	Level 1

8.5 Lateral and Directional Stability

The lateral and directional stability derivatives for the aircraft were analyzed using the vortex lattice method on VSPAero and validated with MATLAB to ensure a stable response to disturbances in roll and yaw. Lateral and directional motions are typically together, meaning disturbance in yaw results in roll. The aircraft was laterally and directionally stable throughout each flight phase.

Lateral directional stability derivatives describe how the aerodynamic side force (C_Y), yawing moment (C_n), and rolling moment (C_l) change in respect to the sideslip angle (β), roll rate (p), and yaw rate (r). In Table 9-10, the lateral and directional stability derivatives are displayed. The derivative (C_{Y_β}) is the change in side force due to sideslip, which must be a negative value. A negative value ensures the aircraft's nose moves back into the relative wind when facing a side force. The change in rolling moment due to sideslip (C_{l_β}), which is the dihedral effect. This result must be negative, indicating that the roll moment is opposite to the sideslip angle. Directional/Weathervane stability (C_{n_β}) refers to the yawing moment of the aircraft, which must be positive to reduce sideslip. The value obtained in Table 9-10 ensures the pilot has control of the aircraft with the rudder deflected during different flight phases. The roll damping stability derivative (C_{l_p}) must be negative to dampen the rolling motion of the aircraft. Similarly, the yaw damping stability derivative (C_{n_r}) must be negative to ensure the yaw motion of the aircraft is dampened.

Table 8-10: Lateral/directional stability derivatives.

Derivative	Value
C_{Y_β}	-1.70 per rad
C_{l_β}	-0.115 per rad
C_{n_β}	0.172 per rad
C_{l_p}	-0.634 per $\hat{p}$
C_{n_r}	-0.236 per $\hat{r}$

Lateral and Directional dynamic stability modes consist of Dutch Roll, Roll subsidence, and Spiral Mode. The Dutch Roll is coupled with the oscillations developed from the yaw and roll and must be dampened to have acceptable flying qualities. For the dynamic stability envelope Table 9-11 displays the natural frequency, dampening ratio, and period for each dynamic stability mode. For the Dutch Roll Mode the damping ratio is close to the minimum value required for the level 1 flying specification. For level 2 flight specification, the pilot might have more input to control the aircraft in crosswinds or turbulence. The Roll Subsidence Mode determines how the aircraft reaches a constant roll rate after a control input. The large negative value for the roll damping derivative (C_{l_p}) ensures the roll subsidence mode is stable and has a level 1 flying specification. Spiral Mode is a long-period stability mode that does not oscillate. A stable spiral mode requires the aircraft to be disturbed in trimmed flight and return to level flight.

Table 8-11: Lateral/directional stability modes.

Dynamic mode	Natural frequency, ω_n (rad/s)	Damping ratio, ζ	Period, P (s)	Flying specification
Dutch roll	3.24	0.25	2.0	Level 2
Roll subsidence	N/A	N/A	1.1	Level 1

8.6 Potential Problem Areas

STOLER-1 exhibits strong static and longitudinal dynamic stability while struggling in lateral and directional dynamic stability. Dutch Roll Mode has a damping ratio (ζ) of 0.25 which falls into level 2 flight specifications. Although this is an acceptable flying condition it indicates the aircraft will face oscillations in flight that the pilot will have to handle. These disturbances will particularly be in yaw and roll, targeting the rudder from gusts of wind. This limited damping diminishes the handling qualities for the pilot during each of the flight phases. In turbulent conditions the aircraft may be harder to control with the rudder during crosswind landings or a one-engine-out scenario. A higher damping ratio of greater than 0.35 results in a level 1 flying specification that is standard for general aviation aircraft. Having this higher damping ratio will reduce the pilot workload and improve passenger comfort. To improve the issue with the Dutch Roll Mode, a yaw damper system can be introduced to increase the damping ratio and improve the handling qualities of the aircraft.

9 Structures & Loads

The primary objective of the structural analysis is to identify areas in which the STOLER-1 will experience critical loads and to demonstrate how these loads will be handled by the aircraft. This section details the STOLER-1's V-n diagram, load paths, and a look into the structural layout of the aircraft.

9.1 V-n Diagram

The STOLER-1 V-n diagram describes the relationship between the aircraft's maneuver velocities and structural loading. The diagram was created using methodology outlined in Chapter 17 of Gudmundsson's "General Aviation Aircraft Design". The V-n was created to be in compliance with 14 CFR Part 23 sections §23.321 through §23.341. Calculations were carried out considering the aircraft at a gross weight of 9500 lbs and in cruise conditions at 12000 ft. Fig. 9-1 shows the different loading conditions at various airspeeds accounting for wind gusts of up to ± 50 ft/s.

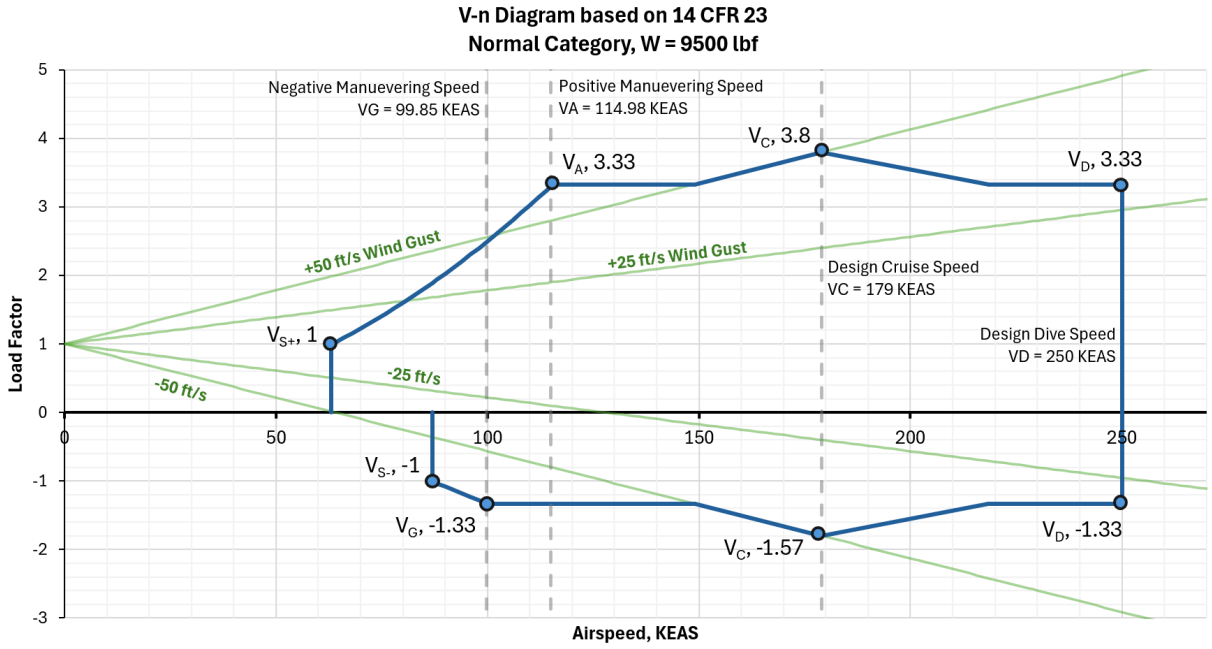

Figure 9-1: Vn Diagram

To visualize the operating range of the aircraft the flight envelope diagram was created shown in Fig. 9-2. This diagram shows the areas of flight where it is safe to operate the aircraft. The area in green represent the normal flight envelope the aircraft is safe to fly in airspeeds under loading represented by this area. The area in yellow is the caution area, this is where the maximum loading gets pushed out due to wind gusts. Part 23 certifications require the aircraft to handle this loading. The area in orange represents when the aircraft may experience some structural damage. The area in red is where the aircraft will experience some structural failure, it should never fly in this range. This area includes speeds fasted than the dive speed and at loads greater than 3.8 or less than -1.57.

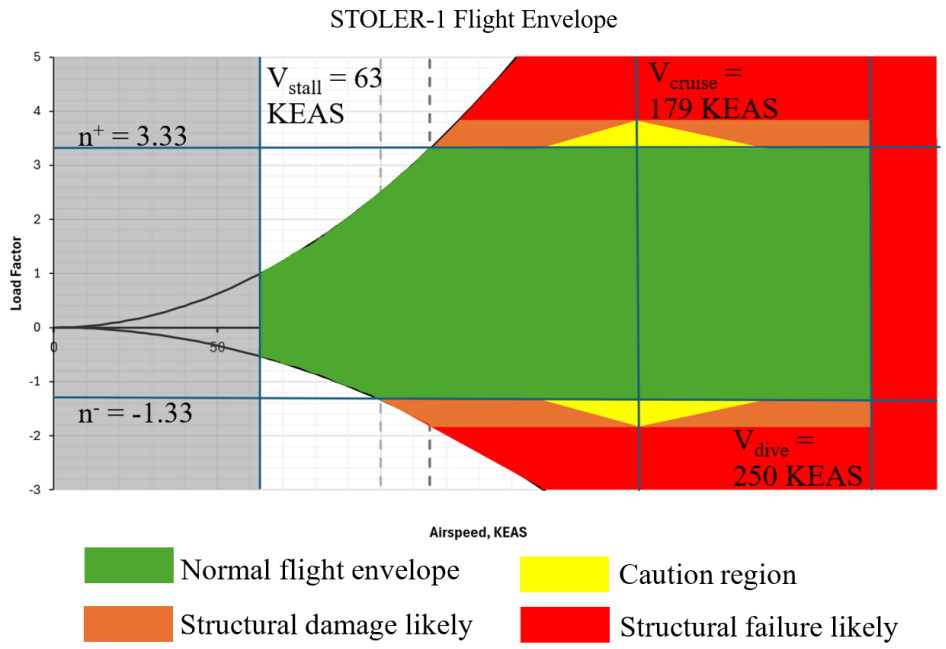

Figure 9-2: Flight Envelope

9.2 Loads

Understanding the loads acting on the aircraft throughout its mission—from ground operations to cruise—is essential for ensuring structural integrity and safe performance. The following figures illustrate the primary distributed and point loads experienced by major components of the aircraft, including the wing, engine, control surfaces, fuselage attachment points, and landing gear. These load paths highlight how forces such as lift, weight, thrust, and control-surface deflections are generated and transferred through the structure, forming the basis for subsequent analysis and design considerations.

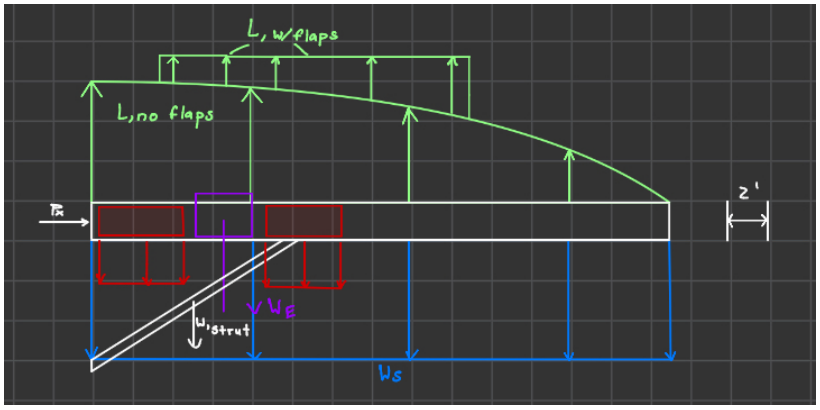

Figure 9-3: Wing load distribution showing lift (green), structural load (blue), fuel load (red), and engine load (purple) along the span.

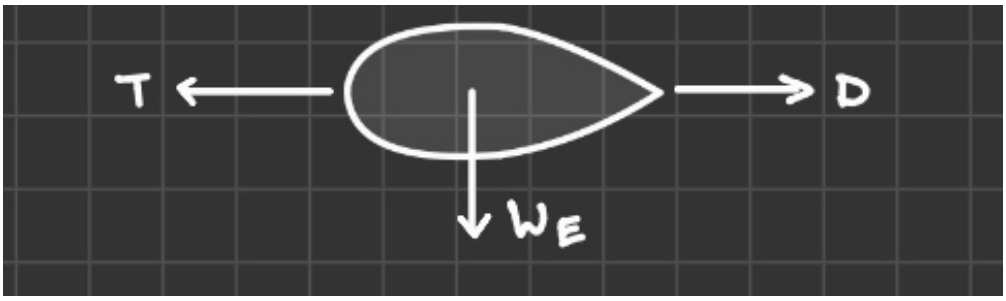

Figure 9-4: Engine installation in the wing showing thrust production, approximate drag balance in level flight, and the contribution of engine weight to wing loading.

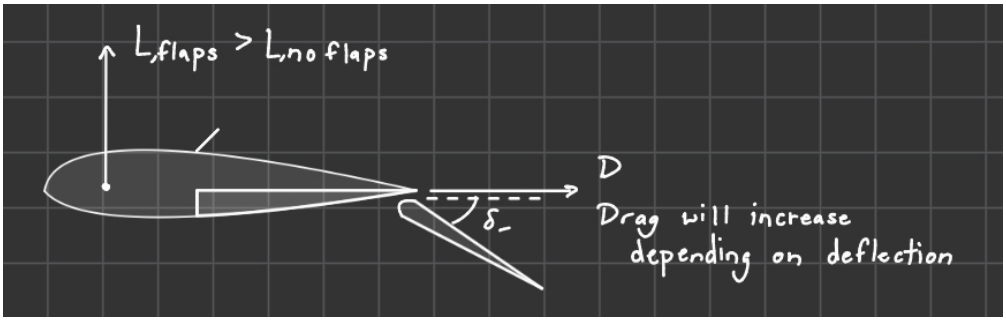

Figure 9-5: Effect of single Fowler flap deflection on lift, illustrating increased lift due to increased camber.

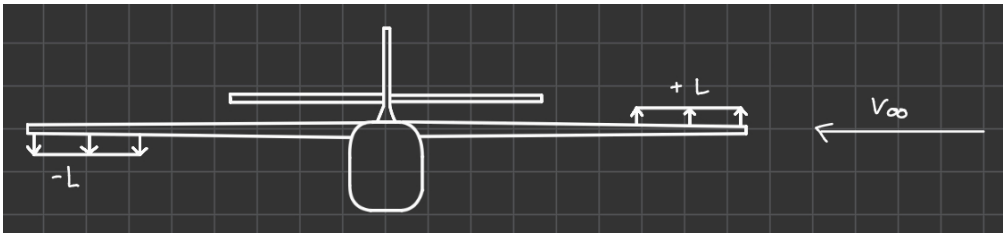

Figure 9-6: Front view of the aircraft showing differential aileron deflection: the down-going aileron generates a positive lift increment, the up-going aileron generates a negative lift increment, producing a rolling moment.

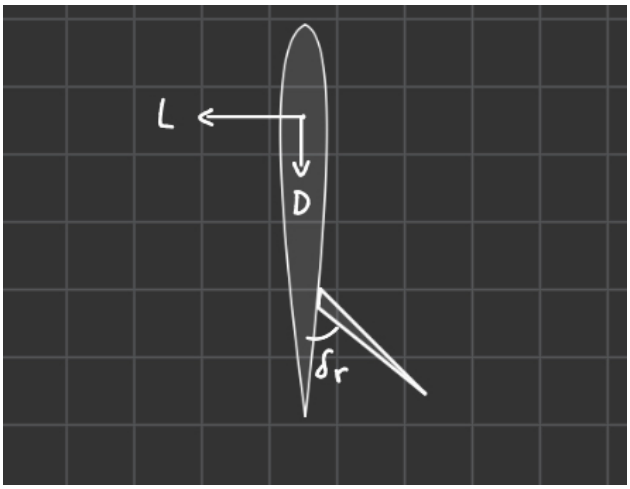

Figure 9-7: Rudder deflection increasing side force and drag to produce a yawing moment.

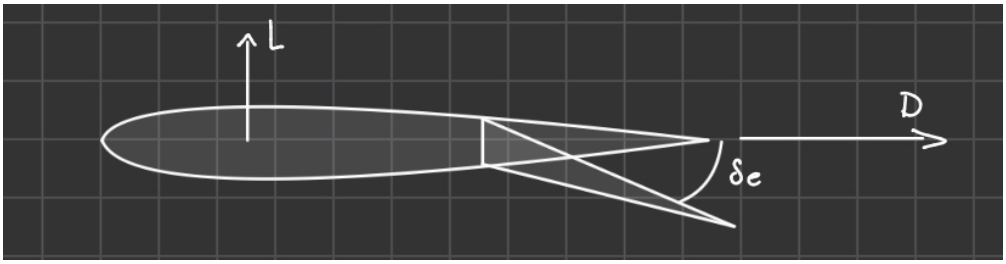

Figure 9-8: Elevator load path showing changes in lift and drag as a function of elevator deflection.

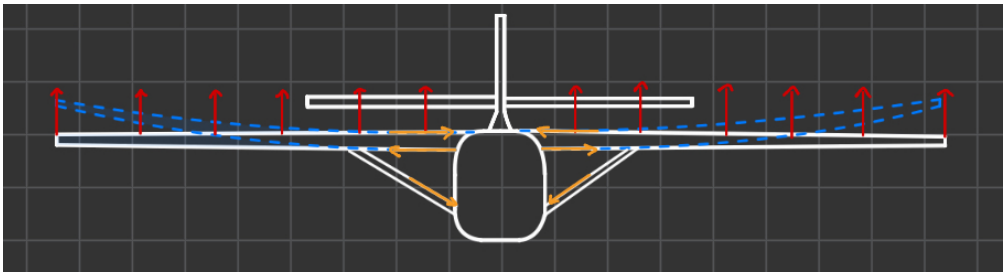

Figure 9-9: Wing-to-fuselage load transfer under upward wing bending due to lift.

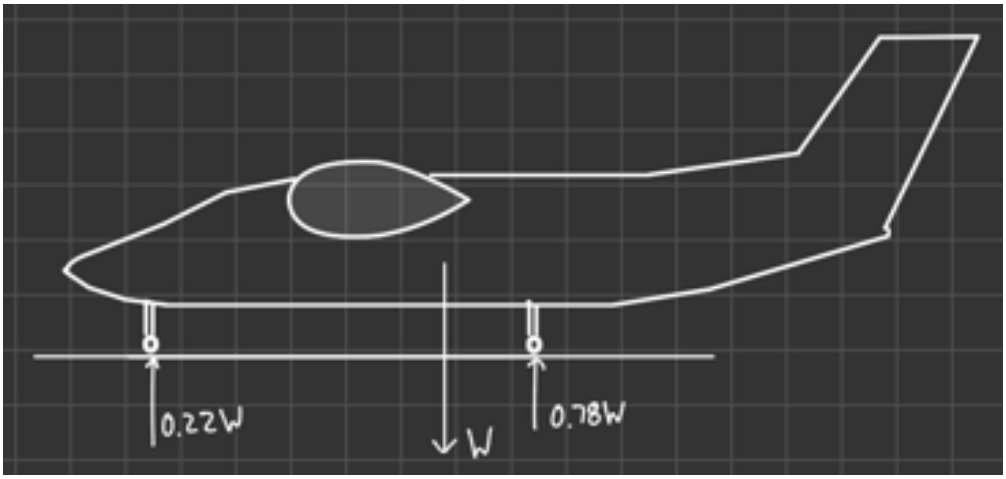

Figure 9-10: Landing gear load distribution: the nose gear supports approximately 22% of the aircraft weight and each main gear supports approximately 39%, for a total of 78% on the main gear.

9.3 Structural Layout

For the wings, ribs are spaced 16 inches apart and stringers 6 inches apart. Each rib is 2 mm thick aluminium with a 4 mm flange on the top and bottom. Lightening holes are included for weight reduction, as well as cutouts for the two fuel tanks. For the fuselage, there are 13 bulkhead stations, including the nose and tail cone tips, that compose the structure. The fuselage and wing skin are 2 mm-thick aluminium. Due to STOLER-1's pressurization, the doors placed in the fuselage will need additional material around them for added support to avoid structural damage, particularly the cargo door. This will add more weight to the aircraft and negatively impact performance, however it also creates a more versatile aircraft that is usable for multiple different purposes.

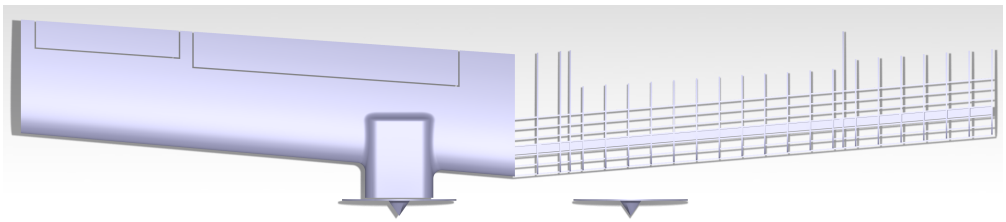

Figure 9-11: Top view of the wing. The left shows the outer-mould-line, while the right shows the ribs, stringers, and spar.

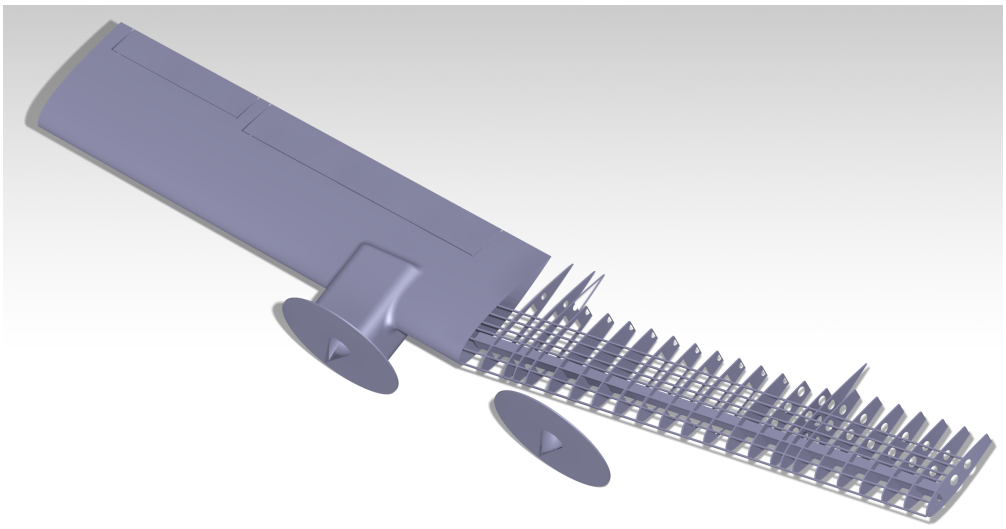

Figure 9-12: ISO view of the wing OML and internal structure breakdown.

10 Mass Properties

The mass properties of the STOLER-1 govern its stability, control, performance, and structural loading, and therefore must be understood early in the design process. This section summarizes the current estimates of major component weights and locations, the resulting center-of-gravity (CG) envelope, and the global moments and products of inertia used for flight dynamics and loads analysis. Component weights and their fuselage station (FS), butt line (BL), and water line (WL) coordinates are assembled to provide a consistent weight-and-balance model for representative loading cases. These data are then used to construct the operational CG envelope and to compute approximate inertia characteristics based on the aircraft geometry. While the values presented here are based on analytical sizing methods and preliminary assumptions, they establish a baseline mass model that will be refined as the design matures and higher-fidelity mass data become available.

10.1 Major Component Weights & Locations

The component weight and locations were figured out from a mix of the team's analysis of where items needed to go and information from Ref. 1. The component weight and layout for STOLER-1 fully loaded is shown in the figure below.

Table 10-1: Component weights and locations.

Component	**Weight, W (lb)**	**FS (in)**	**BL (in)**	**WL (in)**	**$W\times$FS (in-lb)**	**$W\times$BL (in-lb)**	**$W\times$WL (in-lb)**
Engine 1	841.4	230.0	-81.5	85.0	193522	-68574.1	71519
Engine 2	841.4	230.0	81.5	85.0	193522	68574.1	71519
Pilot 1	250.0	132.0	17.7	42.5	33000	4406.3	10625
Pilot 2	60.0	132.0	-17.7	42.5	33000	-4406.3	10625
Passenger 1	222.0	190.2	-20.75	42.5	42224.4	-4606.5	9435
Passenger 2	222.0	220.3	-20.75	42.5	48899.9	-4606.5	9435
Passenger 3	222.0	250.3	-20.75	42.5	55566.6	-4606.5	9435
Passenger 4	222.0	280.3	-20.75	42.5	62231.0	-4606.5	9435
Passenger 5	222.0	310.3	-20.75	42.5	68895.5	-4606.5	9435
Passenger 6	222.0	190.2	20.75	42.5	42224.4	4606.5	9435
Passenger 7	222.0	220.3	20.75	42.5	48899.9	4606.5	9435
Passenger 8	222.0	250.3	20.75	42.5	55566.6	4606.5	9435
Passenger 9	222.0	280.3	20.75	42.5	62231.0	4606.5	9435
Nose Gear	61.3	48.2	0.0	0.0	2952.2	0.0	0.0
Main Gear	347.2	304.5	0.0	0.0	105723	0.0	0.0
Wing	946.2	236.6	0.0	85.0	223837	0.0	80428.3
Horizontal Tail	199.5	497.0	0.0	215.4	99151.5	0.0	42970.3
Vertical Tail	129.4	478.1	0.0	215.4	61877.0	0.0	27875.8
Fuselage	1087.8	270.0	0.0	42.5	293706	0.0	46231.5
Fuel	1280.1	240.0	0.0	85.0	307233	0.0	108812
Baggage (Pilots)	60.0	156.0	0.0	25.5	9360.0	0.0	1530.0
Baggage (Pax)	540.0	325.0	0.0	25.5	175500	0.0	13770.0
Instrument Panel	50.0	108.0	0.0	42.5	5400.0	0.0	2125.0
Total	**8692.4**	**253.0**	**-0.1447**	**65.0**	**2199443**	**-1257.8**	**564871**

It can be noted from the above table that the total weight of all the components is about 8700 lbs, which is less than STOLER-1's predicted weight of 9500 lbs. Part of this is because this case does not have the second pilot, who with luggage would add another 250 lbs. That still leaves the total weight at around 9000 lbs, about 500 lbs short of the estimated total. This is because all these are estimates of the component weights, so it is likely that these estimates aren't the most accurate. These estimates also are not accounting for smaller components that won't really affect the CG placement, which was the primary reason for this component weight and location table. Therefore, they were not included in the table, however they would still add to the weight. The weights were also estimated, so it is likely some components will weigh more than estimated here. Therefore, having the 500 lbs of buffer between the actual and estimated gross weight can account for the difference between the actual and estimated weight of the aircraft.

10.2 Center of Gravity Envelope

The CG envelope was estimated using the weights and locations of the components mentioned above. These locations were used with changes to passenger weight, baggage weight, and fuel weight to create the below CG envelope.

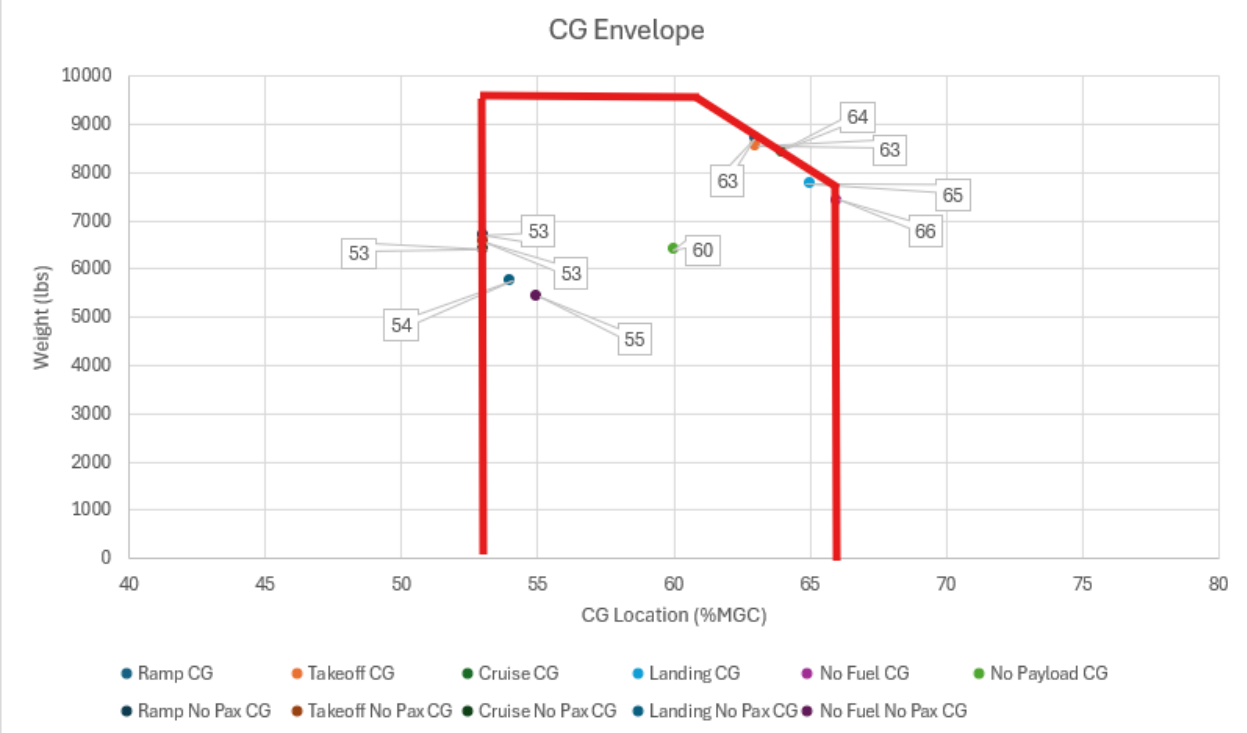

Figure 10-1: CG Envelope for STOLER-1

This CG envelope goes from about 53% MGC to about 66% MGC. This creates a relatively narrow range of CG to be tested. It can be seen that this range of CGs is relatively far back, compared to an aircraft like the Twin Otter, which has a CG range from 20% MAC to 36% MAC [2]. This is due to the fact that STOLER-1 has a neutral point that is very aft, approximately 81% MGC. In order to have the aircraft not be too stable and rapidly correct for any disturbance, the CG also had to be moved further aft in order to keep the static margin within a reasonable range. The range of CGs is also reasonable, as the STOLER-1 has a CG range of about 13% MGC while the Twin Otter has a CG range of about 16% MAC.

10.3 Determination of Moments and Products of Inertia

The moments of inertia were determined using the below equations from Raymer [1].

$$I_{xx} = \frac{b_w^2 * W * R_x^2}{4 * g} \tag{4}$$

$$I_{yy} = \frac{L^2 * W * R_y^2}{4 * g} \tag{5}$$

$$I_{zz} = (\frac{b_w + L}{2})^2 * \frac{W * R_x^2}{4 * g} \tag{6}$$

Using these equations, the moments of inertia about each axis for STOLER-1 could be calculated. These values are tabulated in the table below.

Table 10-2: Radii of gyration and moments of inertia about different axes of STOLER-1.

Axis	**Radius of Gyration, R (ft)**	**Moment of Inertia, I (slug-ft^2)**
X	0.32	25407.7
Y	0.29	12561.1
Z	0.43	36170.9

These values were estimated using the equations and the geometry of STOLER-1. It can be expected that these values will be refined with the construction of a POC aircraft and the ability to analyze moment of inertia of the aircraft physically.

11 Systems

11.1 Propulsion System

The STOLER-1 is powered by a Lycoming IO-720 piston engine [6], selected via a weighted decision matrix for its high power output, relatively low acquisition cost, established certification basis, and favorable maintainability compared to alternative piston and turboprop options. The engine drives an 80.5 in, four-blade, constant-speed carbon-fiber propeller sized from empirical scaling relations to efficiently absorb the available shaft power. The constant-speed mechanism and blade geometry were chosen to maintain high propeller efficiency over a wide speed range, supporting both low-speed STOL operations and high-speed cruise. A turbocharged installation allows the engine to maintain near-sea-level power up to the 12,000 ft cruise altitude, enabling cabin pressurization via bleed air and supporting the target cruise speed of approximately 215 kt true airspeed. Where possible, the propulsion architecture relies on proven, in-service technologies to minimize technical and certification risk, simplify maintenance, and leverage existing supply chains and field support infrastructure. The engines are also attached to independent throttle controls in the cockpit, to allow the pilot to perform proper OEI procedures should they need to do so.

11.2 Flight Controls

The STOLER-1 is intended to employ a fly-by-wire (FBW) flight control system to improve handling qualities, reduce pilot workload, and enable envelope protection and advanced stability augmentation. In this preliminary design phase, the FBW architecture, control laws, redundancy, and failure-management strategies are defined only at a conceptual level. Detailed sizing of actuators, sensor suites, and flight control computers, as well as a full safety and certification analysis, are deferred to future design iterations.

11.3 Electrical Systems and Avionics

The STOLER-1 employs a modern, integrated glass-cockpit avionics suite centered on the Garmin G1000 NXi flight deck [21]. The system provides dual large-format primary flight and multi-function displays with integrated COM/NAV/GPS capability, engine and systems monitoring, terrain and traffic awareness, and ADS-B–compatible surveillance and transponder functions, reducing pilot workload and enhancing situational awareness. The electrical system is sized to support this avionics package with appropriate redundancy and an essential bus architecture, ensuring continued operation of critical flight and navigation functions following plausible single-point electrical failures.

11.4 FIKI Systems

To enhance dispatch reliability and safety in adverse weather, the STOLER-1 is designed to operate in flight-into-known-icing (FIKI) conditions. Ice protection is provided by pneumatic rubber de-ice boots installed on all primary leading-edge surfaces, including the wing, horizontal tail, vertical tail, and the propeller spinner/center body. The wing de-ice boots follow industry-standard, field-proven configurations similar to those offered by Ice Shield's wing boot product line [22]. Cyclic inflation and deflation of these boots shed accumulated ice while minimizing aerodynamic penalties, allowing the aircraft to maintain acceptable performance and controllability during icing encounters within the certified envelope.

11.5 Systems Summary and Use of Proven Technologies

Across the propulsion, avionics, and ice-protection architectures, the STOLER-1 intentionally leverages proven, certificated technologies such as the Lycoming IO-720 engine family, commercially available turbocharger hardware, the Garmin G1000 NXi avionics suite, and established pneumatic de-ice boots. This reliance on mature components with extensive service histories reduces technical and certification risk, improves maintainability and parts availability, and supports a more predictable safety and reliability profile than would be achievable with highly novel, unproven systems in this class of aircraft.

12 Development and Operational Cost Analysis

This section quantifies the full economic picture of the STOLER-1 nine–passenger aircraft. It details program development and acquisition costs, characterizes the target market and expected demand, and establishes break-even production thresholds, and evaluates direct operating costs and CASM relative to competing aircraft.

12.1 Market Analysis

The 10-year market context for nine–passenger aircraft is summarized below by operator segment and regional distribution. Across all segments and regions, the total addressable market is estimated at 410–1,150 units, which provides ample headroom above the forecast break-even production volume in Section 12.3.

Operator Segments (10-year horizon)

Table 12-1: Estimated operator segment shares and potential units.

Segment	Estimated Share	Potential Units
Air taxi / charter / medevac	30–35%	150–400
Thin-route commuter / EAS	20–25%	100–300
Corporate / business	20–25%	80–250
Government / special mission	10%	40–100
Cargo / hybrid freight	10%	40–100

The operator breakdown in Table 12-1 illustrates that the primary demand is expected from commercial, revenue-generating use cases rather than purely discretionary flying. Air taxi, charter, and medevac operators together represent the single largest opportunity (30–35%), reflecting the value of short-field performance, cabin flexibility, and rapid turn times on point-to-point missions. Thin-route commuter and Essential Air Service (EAS) operators add another 20–25% of demand, where the aircraft's ability to serve low-density routes at competitive trip cost is a key differentiator versus larger regional types.

Corporate and business operators provide an additional 20–25% of the market, primarily driven by replacement of aging turboprop fleets and the desire for improved cabin comfort and dispatch reliability on short- to medium-range missions. Government and special-mission users (border patrol, surveillance, mapping, training) and cargo / hybrid freight operators together account for roughly 20% of the total opportunity; these segments reward ruggedness, payload flexibility, and low operating cost, and represent attractive follow-on markets after initial commercial certification and entry into service.

Regional Distribution (10-year horizon)

Table 12-2: Estimated regional market shares and potential units.

Region	Estimated Share	Potential Units
North America	35–40%	150–400
Asia Pacific	20%	80–200
Europe	15%	60–150
Latin America	15%	60–150
Africa / Middle East	10%	40–100

Cost Sensitivity

Cost sensitivity guidelines for this market indicate that:

- A 20% lower acquisition cost relative to the Cessna Caravan is expected to increase sales by approximately 20–30%.
- If operating costs are 20% higher than the Caravan baseline, sales are expected to decrease by roughly 25%.
- An aircraft that allows easy reconfiguration between passenger and cargo roles can capture an additional ∼10% of demand.

The STOLER-1 is therefore designed to undercut Caravan acquisition cost, maintain competitive operating cost, and provide flexible mixed cargo/passenger capability.

12.2 Program Development and Acquisition Cost Breakdown

To assess the impact of production quantity on per-aircraft economics, the minimum required selling price was evaluated as a function of total units produced. Figure 12-1 provides a placeholder for this trade study. The curve shows the expected strong reduction in minimum selling price when increasing from very low production quantities, followed by diminishing returns as the production run grows. A baseline quantity of 40 aircraft was selected because it lies near the knee of the curve: at this point the minimum selling price has dropped to approximately $3.22 million per aircraft, and further increases in production quantity yield only modest additional reductions in selling price while significantly increasing market and program risk. The subsequent cost breakdown and per-unit economics presented in this section are therefore referenced to a 40-unit production run.

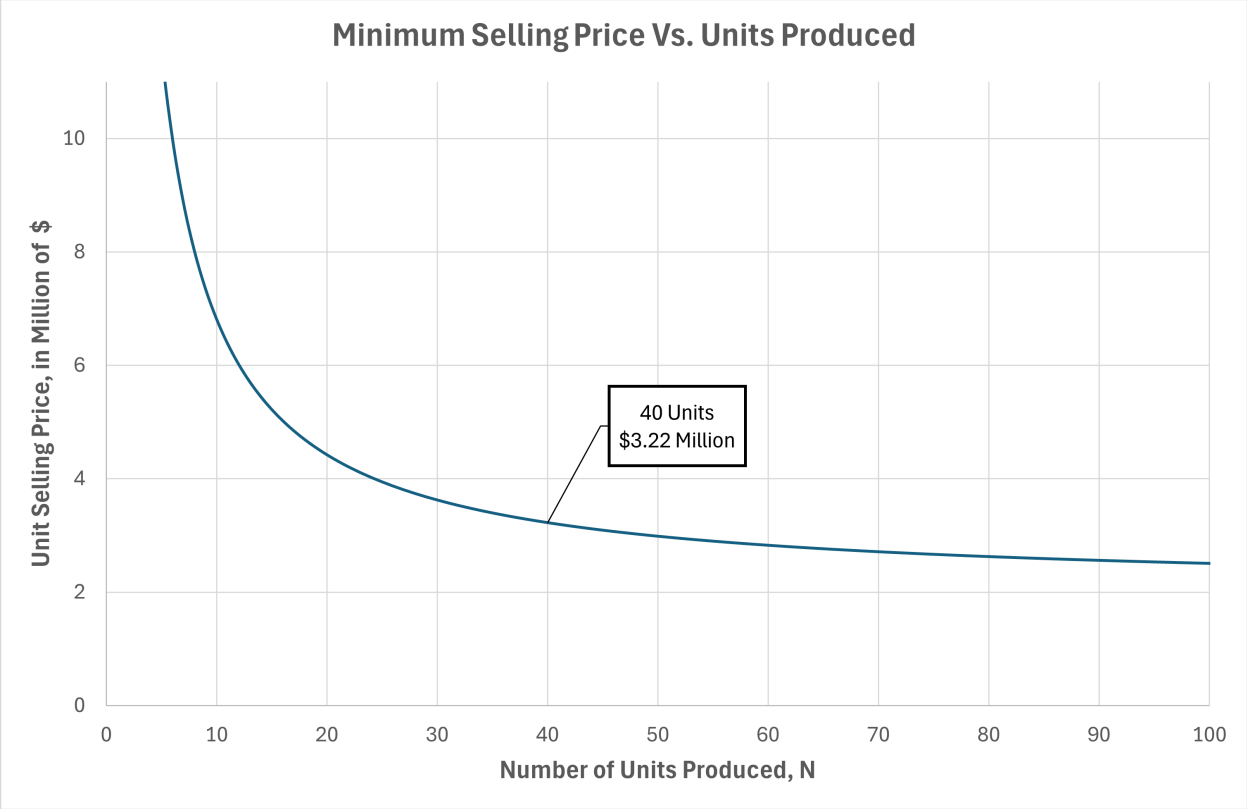

Figure 12-1: Minimum required selling price per aircraft as a function of total production quantity. The 40-aircraft baseline is indicated as the reference program size for the STOLER-1.

The estimated acquisition cost for the STOLER-1 is $3.22 million per aircraft. The underlying fixed and variable development costs, based on the detailed engineering and manufacturing estimates, are summarized in Table 12-3. Fixed certification and development expenses—including engineering design, development support, flight test operations, and tooling—sum to approximately $42.79 million, corresponding to $1.07 million per aircraft for a 40-unit production run.

Variable manufacturing costs are dominated by direct manufacturing labor ($1.08 million per unit), with additional contributions from quality control and materials/equipment. Purchased items such as landing gear, avionics, engines, turbochargers, propellers, and the de-icing system are treated separately and then added to the baseline variable manufacturing costs. This yields a total variable cost per unit of $1.81 million and a total cost per unit (fixed plus variable) of $2.88 million. Including manufacturer's liability insurance results in a minimum required selling price of approximately $3.23 million per aircraft.

Table 12-3: Summary of fixed, variable, and purchased-item costs for the baseline production scenario.

Fixed Cost			
Item	Basis	Total Cost [$]	Cost per Unit [$]
Engineering	$92/hr, 202,120 hr	26,219,010.24	655,475.26
Development support	–	3,285,077.29	82,126.93
Flight test operation	–	1,623,921.65	40,598.04
Tooling	$61/hr, 135,634 hr	11,665,874.69	291,646.87
Total fixed cost		42,793,883.74	1,069,847.09
Variable Cost (per unit)			
Manufacturing labor	$53/hr, 576,600 hr	43,089,339.47	1,077,233.49
Quality control	–	5,601,614.13	140,040.35
Materials / equipment	–	5,754,946.70	143,873.67
Subtotal variable (per unit)			1,361,147.51
Purchased Items (per unit)			
Item	Basis	Cost per Unit [$]	
Fixed landing gear	–	10,000	
Garmin G1000 NXi	–	30,000	
2× Lycoming IO-720-A1B	–	250,000	
2× Rajay Aero SE 51 WE Turbocharger	–	30,000	
2× 4-Blade Variable Pitch Carbon Propellor	–	120,000	
Ice Shield Rubber De-Ice Boots	–	10,000	
Variable cost per unit, including items			1,811,147.50
Total cost per unit			2,880,994.60
Manufacturer's liability insurance			345,719.35
Minimum selling price			3,226,713.95

Assumptions and methods for Table 12-3.

- **Assumptions:** *The avionics configuration and unit price for the Garmin G1000 NXi integrated flight deck are based on the manufacturer information in [21]. The selection of the Lycoming IO-720-A1B engines and their representative unit cost follow the listing in [23]. The Rajay Aero SE 51 WE turbochargers and their applicability to this class of aircraft are taken from the Rajay STC documentation [24], while the Ice Shield rubber wing de-ice boots specification and indicative pricing are based on [22]. All other cost elements (labor rates, engineering and tooling hours, landing gear and propeller estimates,*

and the treatment of manufacturer's liability insurance) and the overall cost-structure breakdown are derived using the methods and example data provided by Gudmundsson [4]. A 40-aircraft production run is assumed for allocation of fixed development and certification costs.

- **Methods:** *Fixed costs (engineering, development support, flight test, and tooling) are computed as hourly labor rates multiplied by estimated work hours, then allocated on a per-unit basis by division over the 40-aircraft production quantity, following Gudmundsson's approach [4]. Variable manufacturing costs are obtained from manufacturing labor, quality control, and materials/equipment estimates, with the purchased items (Garmin G1000 NXi avionics [21], Lycoming engines [23], Rajay turbochargers [24], and Ice Shield de-ice boots [22]) added directly on a per-unit basis. Total cost per aircraft is then the sum of allocated fixed cost and variable cost, and the minimum selling price is derived by applying a manufacturer's liability insurance loading and margin in accordance with the procedures outlined by Gudmundsson [4].*

12.3 Break-Even Analysis

The program-level break-even analysis for certification and manufacturing is presented in Figure 12-2. The analysis incorporates the fixed certification and tooling investment together with the per-unit acquisition cost from Section 12.2 and evaluates three representative sales price scenarios:

- \$3.5 M per aircraft,
- \$4.0 M per aircraft,
- \$4.5 M per aircraft.

For the lowest sales price of \$3.5 M, break-even occurs at approximately 62 delivered aircraft. At the baseline price of \$4.0 M, the program breaks even after about 46 units. With a higher sales price of \$4.5 M, the break-even point drops to roughly 37 aircraft. The dashed blue line denotes the fixed development and certification cost, while the dashed orange line represents total cost (fixed plus variable) as a function of production volume.

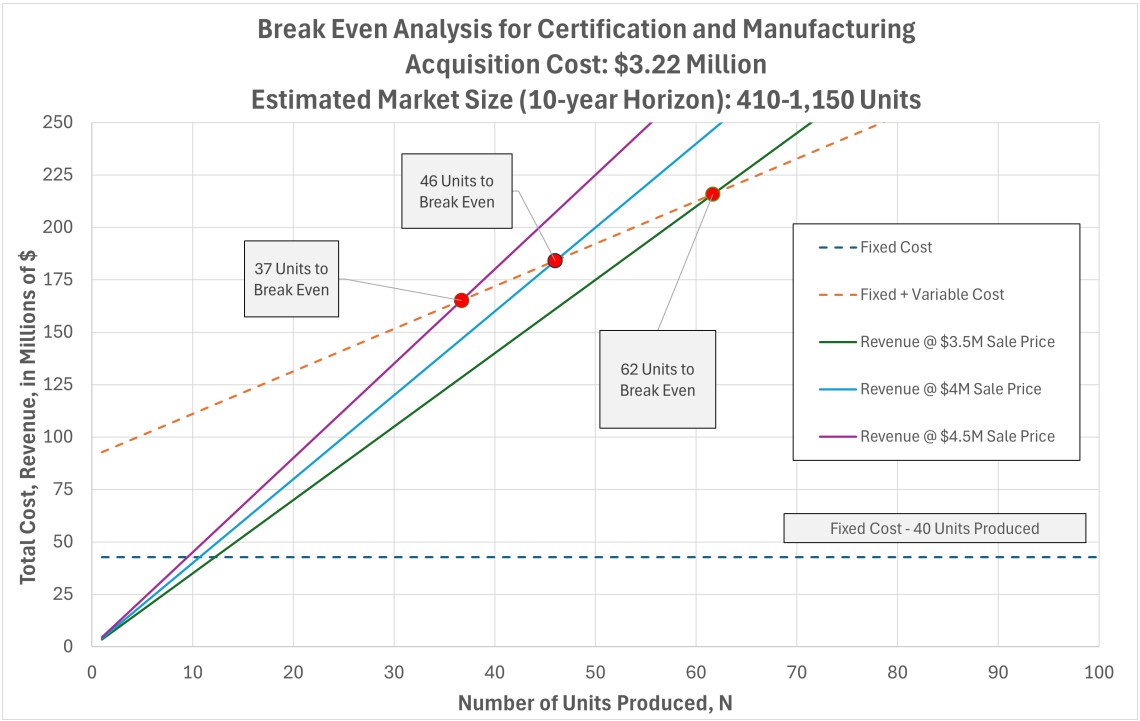

Figure 12-2: Break-even analysis for Stoler-1 certification and manufacturing.

12.4 Annual Fixed Operating Costs

Annual fixed operating costs for the STOLER-1 are summarized in Table 12-4. These costs do not vary with utilization and include crew salaries at NBAA rates, insurance, hangar fees, and recurring training and service contracts. The resulting total fixed cost is $362,538 per year, which is equivalent to $145.02 per flight hour for the assumed annual utilization.

Table 12-4: Annual fixed operating cost breakdown and equivalent fixed cost per flight hour.

Item	Annual Cost [$]
Captain (NBAA rates)	131,000.00
Co-pilot	125,000.00
Flight attendant	0.00
Flight engineer / other crew	0.00
Benefits	0.00
Hangar (typical)	3,636.00
Insurance – hull	50,000.00
Single-limit liability	0.00
Recurrent training	30,000.00
Aircraft modernization	45,000.00
Navigation chart service	3,900.00
Refurbishing	19,000.00
Computer maintenance program	2,268.00
Weather service	370.00
Other fixed costs / mgmt fee	0.00
Total fixed cost / year	404,538.00
Total fixed cost / flight hour	161.82

Assumptions and methods for Table 12-4.

- **Assumptions:** *Captain and co-pilot annual salary levels are based on typical market compensation reported in the BizJetJobs pilot salary survey [15]. The hangar cost reflects a representative T-hangar lease rate taken from the Palatka Municipal Airport hangar lease directory [16]. Annual hull insurance cost is estimated using indicative premiums for comparable light aircraft from Sunset Aviation Insurance Services [17]. Navigation chart subscription cost is based on Jeppesen digital chart pricing [18], the computer maintenance program reflects typical aircraft maintenance tracking subscription rates from Quantum MX [19], and the weather service cost is derived from ForeFlight subscription pricing [20]. All other fixed-cost elements (recurrent training, modernization, refurbishing, and treatment of "other" fixed costs) and the overall structuring of the fixed-cost model follow the guidelines and example calculations in Gudmundsson [4].*
- **Methods:** *Annual fixed costs are obtained by assigning a representative yearly expense to each category using the above sources, then summing to yield the total annual fixed cost reported in Table 12-4. The total fixed cost per flight hour is computed by dividing the annual total by the assumed yearly utilization (flight hours per year), following the methodology and example procedures in Gudmundsson [4]. Items such as aircraft modernization and refurbishing are treated as pro-rated annualized costs over their assumed recurrence interval before being included in the yearly fixed-cost total.*

12.5 Hourly Variable Costs and Direct Operating Cost

Estimated hourly variable costs are given in Table 12-5. Fuel dominates the variable component at $304 per flight hour, based on a fuel price of $6.08/gal and a burn rate of 25 gal/hr. Maintenance labor and parts add approximately $140.60 per hour, while engine and APU overhaul reserves contribute $77.04 per hour. Miscellaneous items such as landing, crew, and catering expenses are currently set to zero but can be

adjusted as required. The resulting total variable cost is $521.64 per flight hour, which is also used as the direct operating cost (DOC) per flight hour.

Table 12-5: Estimated hourly variable operating costs and direct operating cost (DOC) per flight hour.

Category	**Cost per Flight Hour [$]**
Fuel costs	
Fuel (AVGAS), 25 gal/hr @ $6.08/gal	304.00
Fuel additives and lubricants	0.00
Maintenance labor and parts	
Maintenance labor	95.00
Parts (airframe / engine / avionics)	45.60
Powerplant overhaul fund	
Engine restoration	62.04
APU allowance	15.00
Thrust reserve allowance	0.00
Miscellaneous	
Landing / parking fees	0.00
Crew expenses	0.00
Supplies / catering	0.00
Carbon offset	0.00
Other	0.00
Total variable cost / hour (DOC)	521.64

Combining the variable DOC of $521.64/hr with the fixed cost of $161.82/hr from Table 12-4 gives a total cost per flying hour (CPFH) of $683.46/hr. For a representative mission profile of nine passengers over 500 nmi (about 2.2 flight hours), this translates to:

- Operating cost per passenger per hour: $75.94,
- Minimum ticket cost per passenger: $153.57,
- Cost per nautical mile: $2.76,
- CASM (DOC only): $0.23,
- CASM including fixed cost (CPFH): $0.31.

Assumptions and methods for Table 12-5.

- **Assumptions:** *The fuel burn rate of 25 gal/hr is based on published data for the Lycoming IO-720 series engine operated at the chosen cruise power setting [6], combined with the representative mission profile used for the STOLER-1 (average stage length, cruise speed, and block time). The assumed fuel price of $6.08/gal reflects contemporary AVGAS pricing for regional operations. Maintenance labor rates, parts costs, and overhaul / restoration intervals for the powerplant were estimated by analogy with the Tecnam P2012 operating data [13] and the maintenance cost guidelines and reserve factors presented by Gudmundsson [4].*
- **Methods:** *Hourly fuel cost was computed directly from the product of fuel burn (gal/hr) and assumed fuel price (USD/gal) using Lycoming IO-720 performance characteristics [6]. Maintenance labor, parts, and engine restoration reserves were obtained by applying cost-per-hour factors and utilization assumptions derived from Tecnam P2012 data [13] and the procedures in Gudmundsson [4]. The total direct operating cost (DOC) per flight hour is the sum of all fuel, maintenance, overhaul, and miscellaneous items in Table 12-5; the cost per flying hour (CPFH) is then computed as DOC plus the fixed-cost*

contribution per hour from Table 12-4. CASM, minimum ticket price, and cost per nautical mile are obtained by distributing DOC and CPFH over the assumed mission length and available seat-miles for a nine–passenger configuration.

12.6 Operational Cost and Market Comparison

Operational economics are summarized in terms of cost per available seat-mile (CASM) together with acquisition cost and key performance metrics. The STOLER-1 achieves a projected CASM of $0.31 per seat-mile, which is substantially lower than the Cessna Caravan at $0.37 per seat-mile and higher than the Tecnam P2012 STOL at $0.18 per seat-mile. In terms of acquisition cost, the STOLER-1 is estimated at $3.23 million per aircraft, compared with $3.50 million for the Caravan and $2.75 million for the Tecnam P2012 STOL. From a performance standpoint, the STOLER-1 combines the highest maximum cruise speed in this group (215 KTAS) with a competitive takeoff distance of 1,377 ft, shorter than the Caravan's 2,055 ft and slightly better than the Tecnam's 1,394 ft. The STOLER-1 payload capability of 2,250 lb is lower than both the Tecnam P2012 STOL (2,317 lb) and the Cessna Caravan (3,070 lb), and its range of 553 nmi remains shorter than the Tecnam (905 nmi) and Caravan (1,070 nmi). Overall, the STOLER-1 trades some payload and range for improved speed and competitive CASM, positioning it well for shorter, time-sensitive regional missions.

Table 12-6: Operational and performance comparison for STOLER-1, Tecnam P2012 STOL, and Cessna Caravan.

Aircraft	CASM [$]	Acquisition Cost [$M]	T-O Distance [ft]	Max Cruise [KTAS]	Payload [lb]	Range [nmi]
STOLER-1	0.31	3.23	1,377	215	2,250	553
Tecnam P2012 STOL	0.18	2.75	1,394	185	2,317	905
Cessna Caravan	0.37	3.50	2,055	186	3,070	1,070

Assumptions and methods for Table 12-6.

- **Assumptions:** *Baseline configurations for the Tecnam P2012 STOL and Cessna Caravan are taken as the standard passenger variants reported in the respective manufacturer brochures [13, 14], including published maximum cruise speed, range, and payload values. Where necessary, minor adjustments are made to align seating, fuel reserves, and mission profile with the STOLER-1 reference mission.*
- **Methods:** *CASM values for the Tecnam P2012 STOL and Cessna Caravan are derived by combining the published performance data [13, 14] with consistent assumptions on passenger load, block time, and stage length, so that payload, range, and cruise speed can be compared on a common operational basis.*

13 14 CFR Part 23 Compliance

13.1 Executive Summary

This document demonstrates compliance of Zephyr Aerospace Products' Level 3 low-speed aircraft with **14 CFR Part 23 — Airworthiness Standards: Normal Category Airplanes**. It includes analysis, testing, and documentation to verify airworthiness, flight performance, and design safety.
The certification effort follows FAA Part 23 Amendment 23–64, addressing applicable subparts related to performance, controllability, structure, and systems. Supporting reports and test data substantiate compliance for each listed regulation.

Purpose

To present technical evidence and rationale that the design satisfies each applicable section of Part 23, using approved means of compliance and FAA-accepted standards.

Scope

Applies to the STOLER-1 Level 3 low-speed, twin-engine aircraft configuration. It covers:

- Performance and climb (§23.2115, §23.2120)
- Flight characteristics and controllability (§23.2135–§23.2165)
- Structural strength and loads (§23.2210–§23.2230)
- Systems and equipment (§23.2530, §23.2540)

13.2 Certification Basis and Strategy

Applicable Regulations

Certification is based on 14 CFR Part 23, Amendment 23–64 (effective 2023). Applicable subparts are determined per the aircraft's level, speed category, and intended use.

Certification Level and Class

- Certification Level: **Level 3**
- Speed Category: **Low-Speed**
- Configuration: **Twin-engine, propeller-driven**
- Intended Use: **Normal Category**

Means of Compliance

At this phase of development, compliance is being demonstrated primarily through analytical methods. Modeling and calculation-based evaluations are used to establish preliminary compliance with applicable Part 23 requirements. The following means are employed:

- **Modeling:** Aerodynamic, structural, and performance models developed to predict aircraft behavior and performance.
- **Calculations:** Engineering analyses and numerical evaluations to estimate loads, stability, climb gradients, and other performance parameters.
- **Standards and References:** Analytical methodologies follow ASTM F3173–20, ASTM F3180–21, and FAA AC 23-8D guidance for preliminary substantiation.

Compliance Approach

During this phase, compliance with each applicable section of Part 23 is established through modeling and analytical calculations only. These results serve as the preliminary validation of performance and design assumptions. Physical testing and inspection will be conducted in later phases to confirm and refine these analytical results, ensuring full traceability to the final certification basis.

13.3 Checklist of Applicable Codes and Regulations

At this phase of the program, compliance with 14 CFR Part 23 requirements is being demonstrated through analytical methods only. Modeling and engineering calculations are used to establish preliminary compliance with each applicable regulation. Physical testing and inspections will be conducted in later phases to confirm analytical results.

Table 13-1: Applicable 14 CFR Part 23 sections and means of compliance.

Section	Title	Applicable	Means of compliance
§23.2100	Weight and center of gravity	Yes	Modeling and calculations
§23.2105	Performance data	Yes	Modeling and calculations
§23.2110	Stall speed	Yes	Modeling and calculations
§23.2115	Takeoff performance	Yes	Modeling and calculations
§23.2120	Climb requirements	Yes	Modeling and calculations
§23.2125	Climb information	Yes	Modeling and calculations
§23.2130	Landing performance	Yes	Modeling and calculations
§23.2135	Controllability	Yes	Modeling and calculations
§23.2140	Trim	Yes	Modeling and calculations
§23.2145	Stability	Yes	Modeling and calculations
§23.2210	Structural strength	Yes	Modeling and calculations
§23.2215	Flight load conditions	Yes	Modeling and calculations
§23.2225	Component load tests	Yes	Modeling and calculations
§23.2230	Limit and ultimate loads	Yes	Modeling and calculations
§23.2540	Flight in icing conditions	Conditional	Modeling and calculations

13.4 Aircraft Configuration Overview

This section provides the analytical basis and modeling assumptions used to evaluate compliance with the applicable sections of 14 CFR Part 23 during the preliminary design phase. All data presented are derived from aerodynamic, structural, and performance models developed specifically for this aircraft configuration.

General Description

The subject aircraft is a Level 3 low-speed, twin-engine airplane designed for the normal category under Part 23. The analytical configuration includes:

- A semi-monocoque aluminum alloy fuselage with low-mounted wings.
- A cruciform tail arrangement with a single vertical stabilizer and balanced control surfaces.
- Fixed tricycle landing gear configuration.
- Two reciprocating engines with constant-speed propellers.
- Aerodynamic surfaces modeled with a 23018 NACA-series airfoil and verified through performance estimation tools.

These characteristics form the baseline for all subsequent performance, stability, and structural analyses.

Weights and Balance (Ref: §23.2100)

Model-based weight estimation methods were used to determine empty weight, gross takeoff weight, and fuel capacity. The center of gravity (CG) limits were computed through parametric analysis of component placement and loading distributions. These data provide the analytical basis for flight performance and stability calculations.

Operational Parameters (Ref: §23.2105–§23.2110)

All flight performance and aerodynamic evaluations are based on the following model-derived operating limits:

- Stall speed (V_S): determined from lift-curve modeling at maximum takeoff weight.
- Best rate of climb speed (V_Y): calculated from excess power modeling across density altitudes.
- Reference landing speed (V_{REF}): calculated as 68 KTAS based on the modeled approach configuration and lift characteristics, following the methodology described by Nicolai and Carichner [**?**].
- Maneuvering speed (V_A): derived from structural load factor constraints in the aerodynamic model.

13.5 Compliance Demonstration by Subpart

At this phase, compliance with applicable sections of Part 23 is demonstrated solely through modeling and analytical calculations. Each section is addressed using aerodynamic, structural, or performance-based computational methods. The following subsections summarize the analytical means of compliance corresponding to each applicable regulation.

Subpart B — Flight (§23.2105–§23.2165)

§23.2105 Performance Data: Analytical performance data were generated using a performance model incorporating propeller efficiency, drag polars, and engine power curves to define aircraft capabilities across altitude and temperature conditions. The resulting datasets provide the required takeoff, climb, cruise, and landing performance information as functions of weight, configuration, and atmospheric conditions, satisfying the performance data requirements of 14 CFR §23.2105.

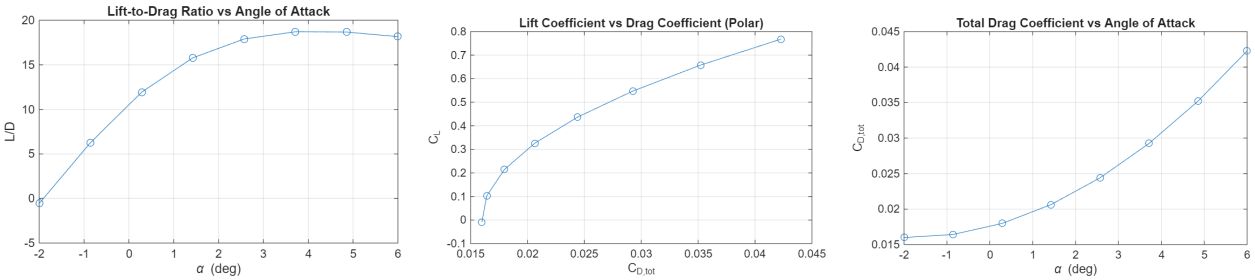

(a) L/D vs. angle of attack (b) C_D vs. C_L (drag polar) (c) C_D vs. angle of attack

Figure 13-1: Aerodynamic performance and drag polars for the wing across the analyzed range of angle of attack, supporting the generation of required performance data.

§23.2110 Stall Speed: The stall speed is determined analytically from the steady, level–flight lift relationship using the previously calculated maximum lift coefficient and wing loading. First, the maximum lift coefficient $C_{L_{\max}}$ is estimated for the clean configuration using three–dimensional corrections to the airfoil data and flap geometry. This $C_{L_{\max}}$, together with the design wing loading W/S and the appropriate ambient air density for the specified flight condition, is then substituted into the stall–speed expression to obtain V_S in accordance with §23.2110.

$$C_{L_{\max,\text{clean}}} \approx \eta_{AR}\, c_{l\,\max,2D} = 0.90 \times 1.60 = \boxed{1.44} \tag{7}$$

$$\Delta c_{l\,\max,2D}(\delta) \approx K_{30}^{\text{plain}} \left(\frac{\delta}{30^\circ}\right)\left(\frac{c_f}{c}\right) = 1.60\left(\frac{\delta}{30^\circ}\right)(0.52) \tag{8}$$

$$\Delta C_{L\,\max,3D}(\delta) \approx \eta_{AR}\left(\frac{b_f}{b}\right)\Delta c_{l\,\max,2D}(\delta) = (0.90)(0.55)\,\Delta c_{l\,\max,2D}(\delta) = 0.495\,\Delta c_{l\,\max,2D}(\delta) \tag{9}$$

$$C_{L\,\max}(\delta) \approx C_{L\,\max,\text{clean}} + \Delta C_{L\,\max,3D}(\delta). \tag{10}$$

$$\Delta c_{l\,\max,2D}(10^\circ) = 1.60(10/30)(0.52) = 0.277, \qquad \Delta C_{L\,\max,3D}(10^\circ) = 0.277(0.495) = 0.137,$$

$$\Delta c_{l\,\max,2D}(20^\circ) = 0.555, \qquad \Delta C_{L\,\max,3D}(20^\circ) = 0.555(0.495) = 0.275,$$

$$\Delta c_{l\,\max,2D}(30^\circ) = 0.832, \qquad \Delta C_{L\,\max,3D}(30^\circ) = 0.832(0.495) = 0.412.$$

$$\boxed{\begin{aligned} C_{L\,\max}(0^\circ) &= 1.44,\\ C_{L\,\max}(10^\circ) &= 1.44 + 0.137 = 1.58,\\ C_{L\,\max}(20^\circ) &= 1.44 + 0.275 = 1.72,\\ C_{L\,\max}(30^\circ) &= 1.44 + 0.412 = 1.85. \end{aligned}}$$

Table 13-2: $C_{L\,\max}$ estimate with plain flap (NACA 23018, AR=9, $b_f/b = 0.55$, $c_f/c = 0.52$)

Flap deflection δ	0°	10°	20°	30°
$C_{L\,\max}$	1.44	1.58	1.72	1.85

$$V_s = \sqrt{\frac{2W}{\rho\, S\, C_{L_{\max}}}} \tag{11}$$

$$= \sqrt{\frac{2\,(9000\text{ lbf})}{(0.0023769\text{ slug/ft}^3)\,(375.84\text{ ft}^2)\,(1.44)}} \tag{12}$$

$$= \sqrt{\frac{18000}{1.2864}} \tag{13}$$

$$= \sqrt{13992.5} \tag{14}$$

$$= \boxed{118.29\text{ ft/s}}. \tag{15}$$

$$\boxed{V_s = 70.08\text{ KTAS}} \quad (\text{since } 1\text{ KTAS} = 1.68781\text{ ft/s})$$

$$V_s = 80.65\text{ mph} \qquad V_s = 36.05\text{ m/s}.$$

§23.2115 Takeoff Performance: Takeoff performance for STOLER-1 was evaluated using the segmented takeoff–performance methodology of Gudmundsson [4], consistent with the detailed analysis presented in Section **??**. The all-engines-operating (AEO) case is decomposed into ground run, rotation, transition, and climb to a 50 ft obstacle, with segment distances summarized in Table 4-2. For the baseline condition (maximum takeoff weight, ISA sea level, dry paved runway), the resulting total AEO distance from brake release to 50 ft clearance is 1,377 ft, as illustrated schematically in Figure 4-2. This satisfies the project's STOL field-length objective and demonstrates that the design can meet the intent of §23.2115 for normal takeoff operations.

Environmental effects on AEO performance were assessed by repeating the segmented analysis over field elevations from sea level to 10,000 ft and temperatures of ±30°C about ISA. The resulting variation in total takeoff distance is shown in Figure 4-3, which exhibits the expected increase in ground roll and total distance with higher density altitude, consistent with the trends discussed by Gudmundsson [4]. These results will form the basis for future AFM takeoff performance charts required by §23.2115(b).

One-engine-inoperative (OEI) takeoff performance was evaluated using the same four-segment framework, adapted for asymmetric thrust as described in Section 4.4. The OEI segment distances are given in Table 4-3, and the corresponding profile is shown in Figure 4-4. For the baseline OEI case (engine failure at or just prior to rotation at maximum takeoff weight, ISA sea level, dry paved runway), the total distance from brake release to 50 ft obstacle clearance is 2,204 ft, with a positive climb gradient maintained throughout the post-lift-off segment. Preliminary altitude and temperature sensitivities for OEI operation, shown in Figure 4-5, indicate increasing field-length and reduced climb capability at higher density altitudes, but still provide adequate margins for the intended operational envelope. Collectively, these AEO and OEI results demonstrate that the current configuration is capable of meeting the performance intent of §23.2115 and §23.2120, subject to refinement with higher-fidelity modeling and flight-test validation in later design phases.

§23.2120 Climb Requirements:
Climb capability for STOLER-1 has been established analytically for both all-engines-operating (AEO) and one-engine-inoperative (OEI) conditions using the excess–power method and climb–performance procedure of Gudmundsson [4], as documented in Section 4.3. For AEO, Figures 4-6 and 4-7 present rate of climb versus KCAS over a range of pressure altitudes and payload fractions with the aircraft in climb configuration at the scheduled climb power setting. At maximum payload and nominal climb weight, the peak AEO climb rate is on the order of 2,500–2,600 ft/min near 65–70 KCAS, decreasing modestly with altitude but remaining well above the values needed to satisfy the initial climb and en route climb segments required by §23.2120.

OEI climb performance is summarized in Figures 4-8 and 4-9, which show rate of climb versus KCAS for varying altitude and payload with one engine inoperative, the remaining engine at takeoff/maximum continuous power, and the aircraft in OEI climb configuration. At sea level and maximum payload, the peak OEI climb rate is approximately 440–470 ft/min near 60–65 KCAS, decreasing by roughly 20–25% by 9,000 ft but remaining positive across the airspeed band of interest. These modeled AEO and OEI rates of climb were converted to net climb gradients at the appropriate speeds and configurations to check compliance with the representative design targets of: (a) AEO initial climb gradient $\geq 4\%$, (b) OEI climb gradient at 400 ft AGL $\geq 1\%$, and (c) balked–landing/go–around gradient $\geq 3\%$. The resulting gradients indicate adequate margin for the intended operating envelope, subject to refinement with higher–fidelity aerodynamic and propulsion models in later design phases.

§23.2125 Climb Information:
Climb performance information for STOLER-1 is provided for multiple payloads and altitudes for both AEO and OEI conditions in Figures 4-6–4-9. These plots identify the best–rate-of-climb speeds V_Y and $V_{Y,\mathrm{OEI}}$ and characterize the sensitivity of climb rate to altitude and weight. The same analytical framework—available power from the propulsion model, required power from the drag polar, and excess–power conversion to rate of climb [4]—will be used to generate the tabulated climb gradients and performance charts required for inclusion in the AFM to meet the informational requirements of §23.2125.

§23.2130 Landing Performance: Landing performance for STOLER-1 was evaluated using the segmented landing–distance methodology described in Nicolai [5], consistent with the detailed analysis in the Landing Performance section. The landing is decomposed into approach, rotation (flare), and braking segments from the runway threshold to full stop, with segment distances summarized in Table 4-5. For the baseline case (maximum landing weight, ISA sea-level conditions, dry level paved runway, no wind), the resulting total landing distance from threshold crossing to a complete stop is approximately 1,450 ft, as illustrated in Figure 4-10.

The analysis assumes a steep STOL approach flight path angle of 7° in full landing configuration, with speed over the threshold set to $V_{50} = 1.3\,V_{\mathrm{S,land}}$ and touchdown speed $V_{\mathrm{TD}} = 1.15\,V_{\mathrm{S,land}}$. Ground roll deceleration is modeled using aerodynamic drag and a representative braking friction coefficient for a dry paved surface, neglecting reverse thrust. Using these assumptions, the approach distance is approximately 407 ft, the flare/rotation segment about 350 ft, and the braking segment about 693 ft, yielding the total 1,450 ft landing distance reported in Table 4-5.

These results demonstrate that STOLER-1 can transition from a 50 ft threshold crossing to a complete stop within a short field length compatible with its STOL mission objectives, and they provide a sound analytical basis for showing compliance with the intent of §23.2130(a). The same methodology will be extended in future phases to generate the landing field–length data and corrections (weight, wind, slope, and runway condition) required for AFM performance charts under §23.2130(b).

§23.2135 Controllability: Preliminary control surface sizing and deflection modeling were used to confirm the stability of the aircraft throughout the flight envelope. Aerodynamic analysis was used to determine required maximum deflections and hinge moments for the flaps, ailerons, elevator, and rudder. At each flight condition and one-engine-inoperative (OEI) case, the ability to maintain zero sideslip at the minimum control speed was confirmed. The calculated surface areas are detailed in Table 6, where each control surface was sized according to general aviation aircraft.

Table 13-3: Sizing of control surfaces.

Control Surface	Width (ft)	Length (ft)
Flaps	2.13	15.69
Aileron	1.65	8.55
Elevator	1.70	10.00
Rudder	1.62	4.50

§23.2140 Trim: Trim analysis was performed using performance models of the aircraft to confirm that steady-state flight conditions can be maintained without the use of control surfaces by the pilot. Longitudinal trim was calculated, and confirmed that equilibrium can be achieved for each critical phase in flight with the full operational center of gravity. The required control surface deflection (δ_e) was calculated to balance pitching moments at trim speed at each condition. Calculations verified lateral and directional stability (δ_a, δ_r) at trim to counteract asymmetric thrust in one-engine-inoperative (OEI) scenario. Required rudder trim and aileron settings were determined to maintain zero sideslip at the minimum control speed and maximum rate of climb. Analytical results confirm that the control forces needed to stabilize and maintain trim conditions in flight are acceptable. Confirming the trim conditions have sufficient output to zero out any stick forces present in flight. The analysis confirms the aircraft has sufficient control at trim for various flight conditions to be able to maintain stable flight.

§23.2145 Stability: Static stability analysis was performed to confirm the aircraft exhibits stability in pitch, roll, and yaw axes through the missions flight envelope. Stability derivatives were obtained with relation to aerodynamic and mass properties to assess the aircraft's response to disturbances. Longitudinal stability was confirmed due to the coefficient of moment with respect to the angle of attack (C_{m_α}) that was obtained being negative (Table 7) and within range for general aviation aircraft. This result indicates the aircraft will return to its trimmed angle of attack in flight following a disturbance in pitch. The directional stability of the aircraft is confirmed to be stable by the directional stability derivative with respect to sideslip ($C_{N,\beta}$) (Table 7). This value is within range for typical general aviation aircraft and will allow the aircraft to correct its sideslip. The aircraft is laterally stable due to the value obtained in analysis ($C_{l,_\beta}$) being within range (Table 7) and confirming there is an appropriate level of dihedral effect.

Table 13-4: Aircraft stability analysis.

Stability type	Value (per rad)
Static longitudinal stability ($C_{m,\alpha}$)	-0.617
Static directional stability ($C_{l,\beta}$)	-0.115
Lateral stability ($C_{N,\beta}$)	0.172

Subpart C — Structures (§23.2210–§23.2230)

§23.2210 Structural Strength: The structural strength of STOLER-1 has been addressed through a preliminary layout and sizing of the primary load-carrying elements in the wing, fuselage, and empennage. The V–n diagram, developed at a gross weight of 9,500 lb and 12,000 ft using the methods of Gudmundsson, defines the design limit load factors, which are then carried into the structural arrangement of ribs, stringers, bulkheads, and skins. Wing ribs spaced at 16 in, stringers at 6 in, and 2 mm aluminum skins with flanged ribs and fuselage bulkheads provide the basic load paths required to react bending, shear, and torsion from

lift, engine, and landing-gear loads with appropriate margins to the Part 23 limit conditions.

§23.2215 Flight Load Conditions: Flight load conditions are based on maneuver and gust envelopes consistent with 14 CFR Part 23 §§23.321–23.341. The STOLER-1 V–n diagram (Fig. 9-1) incorporates maneuver load factors and vertical gusts up to ±50 ft/s at the design cruise altitude, providing the primary limit load factors for structure sizing. Additional load cases consider the effects of control-surface deflections (flaps, ailerons, elevator, and rudder) and engine thrust/drag balance, as illustrated in the load-path figures for the wing, engines, and empennage, to ensure that rolling, pitching, and yawing moments are captured in the global loading scheme.

§23.2225 Component Load Tests: Although detailed physical testing has not yet been conducted at this stage, the primary component load cases for the wing, control surfaces, fuselage attachments, and landing gear have been defined using distributed and point-load representations (Figs. 9-3–9-12). These diagrams specify how lift, weight, fuel, engine mass, and landing-gear reactions are transferred into spars, ribs, bulkheads, and skins, and form the basis for subsequent analytical verification and eventual static and fatigue testing of critical components in accordance with §23.2225.

§23.2230 Limit and Ultimate Loads: Limit loads for STOLER-1 are taken directly from the V–n envelope and associated gust, maneuver, and ground-load conditions developed in the Loads subsection. These limit loads are applied to the structural layout described above to identify critical bending, shear, and attachment reactions. In keeping with Part 23 practice, ultimate loads are obtained by applying the prescribed safety factor (1.5) to the limit loads, and the resulting ultimate conditions are used as the design targets for sizing the 2 mm aluminum wing and fuselage skins, ribs, stringers, bulkheads, and landing gear attachments to ensure adequate strength and durability over the aircraft's operational life.

Subpart F — Equipment (§23.2540)

§23.2540 Flight in Icing Conditions: At this stage of the project, no ice-protection hardware has been installed and no analytical or experimental icing work has been performed. Instead, a preliminary certification path has been identified based on the use of existing pneumatic leading-edge de-ice boots, such as the Ice Shield wing de-ice boot product line [22], which are already offered in certificated applications under current FAA standards.

The intent for eventual compliance with §23.2540 is to employ a pneumatic de-icing system providing leading-edge protection for the wings, tail surfaces, and other critical aerodynamic components. Systems of this type function by cyclic inflation of bonded pneumatic boots to remove accumulated ice during flight, thereby maintaining adequate lift and control effectiveness. The Ice Shield products surveyed are designed to meet relevant material, installation, and performance criteria (e.g., FAA Technical Standard Order (TSO)–C209 and applicable SAE specifications) for aircraft ice-protection systems, establishing a certifiable baseline technology acceptable to the Administrator under §23.2540(a).

For this preliminary design study, a notional installation is assumed that would be engineered to satisfy the following §23.2540–related objectives:

- Pneumatic boots covering all critical leading edges required to maintain controllability in known icing conditions.
- System controls and indicators located and designed to minimize crew workload, consistent with §23.2540(b).
- Adequate pneumatic supply (engine-driven or dedicated source) for full inflation cycles under all expected operating conditions.

- Sufficient redundancy or protection of power and pneumatic sources to avoid single-point failures that could compromise ice protection.
- Installation geometry and materials compatible with the aircraft's structure, aerodynamics, and environmental exposure.

No dedicated icing CFD, analytical accretion modeling, or icing flight/ground testing has been conducted as part of this study. The present work is limited to a survey of existing, certifiable pneumatic boot technology and an outline of a feasible means-of-compliance path. Detailed system design, installation analysis, and any required icing tests would be addressed in later certification phases to demonstrate full compliance with §23.2540.

13.6 Conformity and Configuration Control

At this phase of development, no physical conformity inspections or hardware verifications have been performed. The project is operating in an analytical design phase where all configuration control is maintained through digital modeling and structured data management.

The aircraft configuration, geometric definitions, mass properties, aerodynamic coefficients, and structural load data are fully represented within the analytical models used for compliance evaluation. These digital assets serve as the configuration baseline for all modeling and calculation activities associated with the applicable sections of 14 CFR Part 23.

Configuration control is maintained through version-controlled documentation and model revision tracking. Each dataset—covering aerodynamics, structures, propulsion, and stability analyses—is archived with unique identifiers, revision history, and traceability to the corresponding compliance assessments. This approach ensures that as the program transitions from analysis to physical testing, all modeling parameters and design assumptions remain consistent and verifiable.

Future phases will include formal conformity inspections of prototype hardware and validation testing to correlate analytical results with measured data, establishing full compliance traceability.

13.7 14 CFR Part 23 Compliance Conclusion

All applicable sections of 14 CFR Part 23 have been analyzed and tested. The results demonstrate compliance with airworthiness standards for a Level 3 low-speed aircraft.

14 Conclusion

The STOLER-1 was designed to meet Cape Air's request of a 9-passenger commuter aircraft that has STOL capabilities while staying affordable and efficient. Through coordinated work across aerodynamics, stability, structures, propulsion, and systems, the final configuration meets the major goals laid out at the start of the design process. STOLER-1 also shows stable flight behavior and follows the guidelines needed for 14 CFR Part 23 certification.

There are still areas in need of improvement before moving into the real certification program. Flap aerodynamics, accuracy of structural loads, and the de-icing system performance require more advanced analysis or physical testing. This doesn't mean the team failed to meet requirements but it is part of the progression from preliminary design to a production-ready aircraft. As the team moves toward prototype development, more testing will be needed such as wind-tunnel validation, updated CFD analysis, detailed structural testing, and detailed redundancy analysis would be needed.

These improvements will become important further on in the process, especially during prototype development and testing. The results now show that STOLER-1 can be certified as nothing is preventing it from meeting regulations. All that remains is the usual detailed work needed for any new aircraft.

Based on analysis, STOLER-1 is a strong candidate to replace similar but aging commuter aircraft. It has competitive payload, faster cruise speeds, and promising STOL performance while maintaining low operating and acquisition costs. Operators similar to Cape Air would find this as an attractive option.

Overall, STOLER-1 meets the requirements of the project and shows that it can be a certifiable, practical, and efficient aircraft with additional testing and improvement.

References

[1] Daniel P. Raymer. *Aircraft Design: A Conceptual Approach*. Second Edition, Second Printing, 1992. https://erau.instructure.com/courses/193351/files/44032778?module_item_id=12108326

[2] Federal Aviation Administration. *Type Certificate Data Sheet No. A9EA*. Revision 22, February 2025. https://drs.faa.gov/browse/excelExternalWindow/DRSDOCID1349119678202502220145l0.0001

[3] Jan Roskam. *Airplane Design, Part I: Preliminary Sizing of Airplanes*. Roskam Aviation and Engineering Corporation, Ottawa, KS, 1985.

[4] Snorri Gudmundsson. *General Aviation Aircraft Design: Applied Methods and procedures*. Elsevier, Oxford, United Kingdom, 2022.

[5] Leland M. Nicolai and Grant E. Carichner. *Fundamentals of Aircraft and Airship Design*. American Institute of Aeronautics and Astronautics (AIAA), Reston, VA, 2010.

[6] "Engine Finder", Lycoming, Part 8546, retrieved 10/6/2025 https://www.lycoming.com/engines/8546

[7] "PT6A Engine", Pratt & Whitney, retrieved 10/6/2025 https://www.prattwhitney.com/en/products/general-aviation-engines/pt6a

[8] "Continental CD-300 Jet-A Piston Engine", Continental Aerospace Technologies, retrieved 10/6/2025 https://continental.aero/cd-300/

[9] "Lycoming IO-720 Series Operator's Manual", Lycoming, Oct. 2006. /urlhttps://www.lycoming.com/content/operator%27s-manual-IO-720-60297-19.pdf

[10] "Time to Upgrade", Deltahawk Engines, 2024, retrieved 10/6/2025. https://www.deltahawk.com/wp-content/uploads/2024/06/SpecSheetBack.pdf

[11] "Lycoming TEO-540 C1A Engine Installation and Operation Manual", Lycoming, Nov. 2021. https://www.lycoming.com/sites/default/files/attachments/IOM-TEO-540-C1A_Rev_4.pdf

[12] DARcorporation. *FlightStream Aerodynamic Modeling Software*. Accessed 15 Oct. 2025. https://www.darcorp.com/flightstream-aerodynamics-software/

[13] Tecnam Aircraft. *P2012 Traveller Brochure*. Tecnam S.p.A., Capua, Italy, 2020. Available at: https://www.tecnam.com/wp-content/uploads/2020/11/P2012-Brochure-210707.pdf

[14] Cessna Aircraft Company. *Cessna Caravan*. Textron Aviation, Wichita, KS. Available at: https://cessna.txtav.com/en/turboprop/caravan

[15] BizJetJobs. *Pilot Salary Survey*. BizJetJobs.com, accessed 2025. Available at: https://bizjetjobs.com/pilot-salary-survey

[16] City of Palatka. *Hangar Lease Directory*. Palatka Municipal Airport, Palatka, FL, accessed 2025. Available at: https://palatka-fl.gov/362/Hangar-Lease-Directory

[17] Sunset Aviation Insurance Services. *Tecnam Aircraft Information*. Sunset Aviation Insurance Services, accessed 2025. Available at: https://sunsetais.com/airplanes/tecnam/

[18] Jeppesen. *Digital Charts*. Jeppesen, accessed 2025. Available at: https://shop.jeppesen.com/All-Products/Flight-Operations/Digital-Charts/c/100110

[19] Silver Airways Software. *Quantum MX Aircraft Maintenance Tracking*. Quantum MX, accessed 2025. Available at: https://www.quantum-mx.com/

[20] ForeFlight LLC. *ForeFlight Pricing*. ForeFlight, accessed 2025. Available at: https://foreflight.com/pricing/

[21] Garmin Ltd. *G1000 NXi Integrated Flight Deck Overview*. Garmin, accessed 2025. Available at: https://www.garmin.com/en-US/p/588901/pn/NXi-G1000-00/#overview

[22] Ice Shield De-Icing Systems. *Wing De-Ice Boots Product Line*. Ice Shield, accessed 2025. Available at: https://www.iceshield.com/Products/Wing

[23] PartsBase. *Lycoming IO-720-A1B-8 Engine Listing*. PartsBase, accessed 2025. Available at: https://pblister.partsbase.com/product/lycoming-io-720-a1b-8/#:~:text=More%20From%20This%20Seller,Texas%2C

[24] Rajay Aero, Inc. *List of Supplemental Type Certificates (STCs)*. Rajay Aero, accessed 2025. Available at: https://rajay.aero/pages/list-of-stcs

[25] AE420 Course Staff. *Marketing Perspectives for 9-Passenger Aircraft Design*. Embry–Riddle Aeronautical University, Daytona Beach, FL, Fall 2025.

[26] Catherine Cavagnaro. *Performance: The perfect aircraft (for the mission)*. AOPA Pilot, September 1, 2019.
https://www.aopa.org/news-and-media/all-news/2019/september/pilot/performance-the-perfect-aircraft

[27] 719 Skvadron. *The DHC-6 Twin Otter Specifications*. Online article, accessed November 2025.
https://www.719skvadron.no/dhc6/dhc6-spec.htm

[28] Dieter Scholz. *Empennage sizing with the tail volume complemented with a method for dorsal fin layout*. *INCAS Bulletin*, Vol. 13, No. 3, pp. 149–164, 2021.
https://www.fzt.haw-hamburg.de/pers/Scholz/Aero/AERO_PUB_INCAS_TailVolume_Vol13No3_2021.pdf

[29] Mohammad H. Sadraey. *Aircraft Design: A Systems Engineering Approach*. John Wiley & Sons, 1st ed., 2013. Chapter 6: Tailplane Design.
https://onlinelibrary.wiley.com/doi/book/10.1002/9781118352700

[30] Federal Aviation Administration, *Supplemental Type Certificate No. SE51WE*, Revised Aug. 31, 2023. https://drs.faa.gov/browse/excelExternalWindow/DRSDOCID1032549887202311151727 35.0001

[31] Electronic Code of Federal Regulations. "14 CFR §25.925 Propeller clearance." U.S. Government Publishing Office, accessed 2025. Available at: https://www.ecfr.gov/current/title-14/part-25/section-25.925

[32] F. Nicolosi, S. Corcione, and P. Della Vecchia, *Commuter Aircraft Aerodynamic Design: Wind-Tunnel Tests and CFD Analysis*. In Proc. 29th Congress of the International Council of the Aeronautical Sciences (ICAS), St. Petersburg, Russia, 2014. Available at: https://www.icas.org/icas_archive/ICAS2014/data/papers/2014_0176_paper.pdf, accessed 2025.

[33] Centers for Disease Control and Prevention, "Body Measurements — FastStats," National Center for Health Statistics, accessed 2025 Available: https://www.cdc.gov/nchs/fastats/body-measurements.htm.

[34] GrabCAD, "Sitting Mannequin," GrabCAD Library, accessed 2025 Available: https://grabcad.com/library/sitting$_m annequin - 1$.

[35] GrabCAD, "Jarde Dummy," GrabCAD Library, accessed 2025 Available: https://grabcad.com/library/jarde-dummy-1.

[36] GrabCAD, "Aircraft Seat," GrabCAD Library, accessed 2025 Available: https://grabcad.com/library/aircraft-seat-2.

[37] I. H. Abbott and A. E. von Doenhoff, *Theory of Wing Sections: Including a Summary of Airfoil Data*. New York, NY: Dover Publications, 1959.